Universidad de Concepción

Facultad de Ingeniería

Doctorado en Energías

A CFD Based Design Model for Tubular Fixed Bed CO₂ Methanation Reactors under Power to Gas Operation

Tesis presentada a la Facultad de Ingeniería de la Universidad de Concepción para optar al grado académico de Doctor en Energías.

POR: Victor Soto Pascual,

Profesor Guía: Dra. Ximena García C.

Facultad de Ingeniería

Universidad de Concepción

Profesor Co-Guía: Dra. Claudia Ulloa T.

Facultad de Ciencias Ambientales

Universidad de Concepción

Concepción, Chile 2022.

Acknowledgments

Abstract

Today, there is no doubt that renewable energy will and must play a central role in the future's energy mix. During the 2000s and 2010s the strong growth in wind and solar photovoltaic plants for electricity production was mostly prompted by economics, environmental and social drivers. However, due to recent geo-political developments (Ukraine War, South China Sea disputes), the energy independence has resurged as an additional promoter for renewable energy development. In either case, it is already demonstrated that a large participation of non-dispatchable renewable energy in the electrical grid requires seasonal and hourly storage system to balance peak and low generation periods. Power to X (PtX) technologies, allows for the required storage, transforming electrical energy surplus into other energy carriers such as methane, hydrogen and methanol. In this work, methane as final product of the PtX process is considered due to its versatility and capacity to easily been injected into the existing gas grid. Therefore, the methane storage path also known as Power to Methane (PtM) will be mostly used to describe a particular form of Power to X system, which is of interest in this study. This work addresses one of the main technical problems demanded by methanation technology: heat management and temperature control of CO_2 methanation reactors. A novel Computational Fluid Dynamics based design methodology is proposed for tubular fixed bed reactors in a PtM operational context. This thesis outlines an extensive literature review regarding the current trends in reactor modelling and the operational requirements of PtM technology. The main technological challenges regarding heat management in the tubular fixed bed reactor concept have not been addressed properly. In this research a computational modelling methodology was developed to design a methanation reactor in the context of a PtM operation. A 3D transient computational fluid dynamics model was implemented in ANSYS Fluent for such purposes. First a suitable CO_2 kinetic model is validated against experimental data using a simplified tubular reactor model. Then, the heat transfer process between the reactor tubes and coolant is assessed against empirical correlations used extensively in shell and tube heat exchanger design. This unique approach allows to ensure that the proposed design fulfills entirely, both product gas quality (methane content) and heat management capabilities. Then, a sensitivity study was carried out to identify relevant differences between the two most common coolant fluids used in methanation. Unlike what is found in the revised literature, the most suitable coolant in terms of pumping energy consumption and heat transfer, is thermal oil instead of molten salts. Then, an optimal flow of coolant is found, which minimizes the energy consumed in pumping, while maintaining an optimum temperature control. Finally, a design configuration is proposed based on two modules (the first one of 1 m length, and the second of 0.5 m) with interstage water condensation. Then, the design configuration obtained in the previous chapter is subjected to disruptions relevant to Power to Gas operation. Firstly, the amount of time the reactor requires to reach the steady state from a standby condition is determined. In line with similar works, the time required for the reactor to leave the warm-start condition was 330 s. As for the reactor shutdown, it took 130 s to return to its original warm-start condition. Regarding reactor feeding relevant disruptions, a 30 s H_2 feed interruption prompted a transient low-temperature hot-spot. After 90 s of resuming the H_2 feed, the temperature profile returned to its original values. As for temperature disruptions, a 20 K sudden inlet feed rise, promoted the formation of a lower hot-spot and a new steady state at lower temperatures. On the other hand, a 20 K feed temperature drop triggered a high temperature hot spot, which exposed the catalytic bed to its maximum operating temperature ($\approx$923 K). The appearance of this "wrong-way" behaviour was explained by the combined effect of transient reactant concentration and thermal inertia of the bed. Temperature disruptions did not affect substantially the quality of the outlet gas, while the H_2 interruption induced a 90 s latency time required to return to the minimum methane required concentration. Finally, in the absence of coolant flow or chemical reaction, the reactor maintained warm start conditions for 3 h after all heat flow ceased. The author expects that this thesis will serve as a reference tool to the designers, chemical

or mechanical engineering students to better understand the phenomena involved in chemical reactor engineering in the context of intermittent energy storage.

Thesis Organization

Chapter I introduces and explains the background of the engineering problem to be solved. Chapter II revises the most relevant literature of current intermittent energy storage systems and the current modelling approaches to fixed bed reactors and their theoretical features. Chapter III underlines the research Hypothesis. Chapter IV comprises the main results. Chapter V and VI states the main conclusions and proposes some recommendations for future works.

The following journal articles constitute the main results of this thesis:

- Chapter IV.1: A CFD Design Approach for Industrial Size Tubular Reactors for SNG Production from Biogas (CO_2 Methanation). *Energies*, *14*(19), 6175. https://doi.org/10.3390/en14196175
- Chapter IV.2: A 3D Transient CFD Simulation of a Multi-Tubular Reactor for Power to Gas Applications. *Energies*, *15*(9), 3383. https://doi.org/10.3390/en15093383
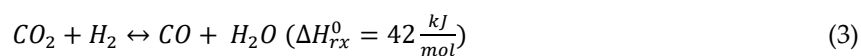
Table of Contents

I. Introducción

I.1 Energía renovable intermitente y su almacenamiento

De acuerdo a la Agencia Internacional de Energía, IEA, en el año 2023 las energías renovables, tendrán un gran protagonismo en el sector generación, suministrando alrededor de un 30% de la demanda global de electricidad, valor que ya se eleva por sobre un 24% en el año 2017. Durante este período, se estima que el 70% del crecimiento en la generación mundial de electricidad, será dominado por fuentes renovables, liderados en primer lugar por las energías solar fotovoltaica y eólica, seguidas por la hidroelectricidad y bioenergía [1]. En efecto, al 2022, los nuevos proyectos de generación eléctrica, a nivel mundial, son liderados por tecnologías basadas en energías renovables, en particular solar fotovoltaica (146 GW) y eólica (76 GW) [1]. La disminución de los costos de estas tecnologías no ha sido el único promotor de su masificación, sino que también compromisos internacionales de desarrollo sostenible, como el "Acuerdo de París" [2]. Lo anterior a impactado en que al 2020 la energía eléctrica a nivel mundial proveniente de fuentes eólica (inshore y offshore) llegó a 1600 TWh, experimentando el mayor crecimiento de todas las demás fuentes de energía combinadas [3]. Para el caso de la energía solar fotovoltaica (solar PV) durante el año 2020 se generaron 821 TWh, un 23% más que el año 2019, convirtiéndose en la tercera mayor fuente de energía renovable durante el 2020, desplazando a la bioenergía y situándose tras la inshore eólica y la hidroeléctrica [4]. Por otro lado, la Política Energética Nacional [5] ha establecido que para el año 2050, al menos 70% de la generación eléctrica del país provendrá de fuentes renovables. La incorporación a gran escala de estas fuentes de energía plantea nuevos desafíos, relacionados con el almacenamiento de los excedentes producidos, los que se relacionan principalmente con el carácter intermitente de los recursos eólico y solar. Estos excedentes, generados por los desfases naturales entre la oferta y demanda de energía, actualmente son vertidos, disminuyendo la eficiencia global del sistema eléctrico. En consecuencia, el incremento de la participación de energías renovables no convencionales (ERNC), en Chile y el mundo, deberá enfrentar el reto de almacenamiento de energía a gran escala, ámbito de gran interés para la investigación y desarrollo en el sector de energías renovables a nivel mundial. Se han propuesto y estudiado numerosas alternativas de almacenamiento energético entre las que se destacan las tecnologías Power to X (PtX) en las que el Power to Methane (PtM) destaca como un versátil proceso de almacenamiento en forma de metano [6, p. 2].

I.2 PtM

El proceso PtM consta de dos etapas: i) producción de H_2 vía electrólisis de agua, utilizando los excedentes de energía eléctrica y ii) producción de CH_4 vía hidrogenación catalítica (metanación) de CO (ecuación 1) o CO_2 (ecuación 2), provenientes de otros procesos industriales (industrias siderúrgicas, plantas de cemento, plantas de biogás, procesos de gasificación de biomasa y carbón, entre otros). Cabe mencionar que la hidrogenación de CO_2 se da como una combinación lineal de la hidrogenación de CO y la reacción *Reverse-Water-Gas-Shift* (ecuación 3), proceso que usualmente es llamado "metanación indirecta".

$$CO + 3H_2 \leftrightarrow CH_4 + H_2O \ (\Delta H_{rx}^0 = -206 \tfrac{kJ}{mol}) \tag{1}$$

$$CO_2 + 4H_2 \leftrightarrow CH_4 + 2H_2O \ (\Delta H_{rx}^0 = -164 \tfrac{kJ}{mol}) \tag{2}$$

$$CO_2 + H_2 \leftrightarrow CO + H_2O \ (\Delta H_{rx}^0 = 42 \tfrac{kJ}{mol}) \tag{3}$$
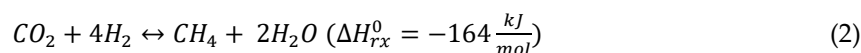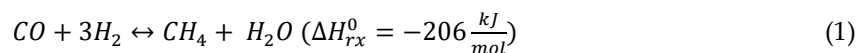
La metanación de CO/CO_2 se lleva a cabo principalmente en reactores de lecho fijo: adiabáticos o politrópicos (de haz de tubos) [7]. Tradicionalmente, este proceso, se ha basado en cascadas de reactores

con enfriamiento intermedio y/o reciclo de producto, logrando altas conversiones de CO/CO₂, al tiempo que se mantienen temperaturas adecuadas en cada reactor. Este concepto está disponible a escala industrial para el proceso de producción de gas natural sintético (SNG) a partir de gas de síntesis derivado de la gasificación de carbón o biomasa [8]. Las tecnologías de metanación actualmente disponibles (TREMP de Haldor Topsoe, entre otras [9]), fundamentalmente están concebidas para operar en régimen permanente, sin mayores perturbaciones y han sido diseñadas principalmente para metanación de CO, dado que estas tecnologías fueron originalmente concebidas para la metanación de gas de síntesis. La literatura señala que una operación costo eficiente de estos sistemas requiere de reactores de metanación que operen bajo condiciones dinámicas, acorde con la intermitencia de la producción de excedentes de energía eléctrica [10]. Las condiciones dinámicas de operación se traducen en cambios bruscos de la temperatura del reactor, afectando la estabilidad térmica, actividad y vida útil del catalizador. Para hacer frente a este problema, el foco de los últimos estudios ha sido el estudio de estrategias de operación estables y eficientes, a escala experimental o de simulación de procesos.

I.3   Clasificación general de reactores de metanación

El concepto de control del calor de reacción (reactor adiabático o politrópico) en conjunto al modo de contacto entre la fase gas y catalizador (lecho fijo, fluidizado, estructurado o trifásico) son elementos de particular importancia a la hora de caracterizar los distintos tipos de reactores para metanación. Actualmente los reactores de lecho fluidizado se encuentran en etapa demostrativa, mientras que los reactores estructurados y trifásicos, todavía se encuentran a escala de laboratorio y son adecuados para capacidades bajas [11]. Cabe destacar que los reactores de lecho fijo han sido especial objeto estudio para la operación dinámica. Su optimización, ya sea en el número de etapas en la versión adiabática, o la estrategia de control térmico para la versión politrópica, ha sido el foco de las últimas investigaciones pertinentes a la problemática [12]. El reactor politrópico, consistente en un haz de tubos en paralelo de diámetro relativamente pequeño (10-30 mm) es destacado por la literatura revisada, por sobre el concepto adiabático. Matthischke et al. [13], concluye en su trabajo, que el tiempo de partida para los reactores politrópicos es considerablemente más bajo que el de su par adiabático. Ghaib & Ben-Fares [12], señala que los reactores politrópicos exhiben gradientes de temperatura más bajos, lo cual conlleva a un incremento en la vida útil y mayor flexibilidad. En la misma línea, Rönsch, et al. [7] concluye que la temperatura de "punto caliente" o "*Hot Spot*", para un reactor politrópico, es considerablemente más baja, respecto a la de un reactor adiabático, por lo que también los productos salen del reactor a temperaturas moderadas (300°C). Este tipo de reactores combinaría las ventajas de un reactor isotérmico y adiabático. Las temperaturas moderadas de *"Hot Spot"* promoverían la velocidad de reacción, mientras que las bajas temperaturas a la salida permiten altas tasas de conversión (en lo que respecta a las limitaciones termodinámicas). A todas las ventajas antes mencionadas, se agrega la de prescindir de equipos auxiliares tales como compresores de reciclo o reactores en cascada con sus respectivos enfriadores intermedios.

I.4   Desafíos en diseño y modelación de reactores para metanación

En el ámbito de la ingeniería de reactores para metanación, una de las líneas de trabajo más relevantes corresponde a la modelación y diseño de reactores sometidos a perturbaciones propias al régimen PtM, elemento discutido a continuación. A pesar de su relativa madurez tecnológica, los reactores de lecho fijo politrópicos todavía enfrentan importantes desafíos en su diseño y modelación que todavía impiden su implementación a gran escala o industrial. En el caso de los reactores de metanación en sistemas PtM, éstos operan bajo condiciones de operación dominadas por las intermitencias inherentes a la generación basada en energías renovables, en particular eólica y solar. En consecuencia, el diseño

y optimización de reactores de metanación para sistemas PtM, presenta importantes desafíos en cuanto a su estabilidad y eficiencia. En particular, debido a la alta exotermicidad de la reacción de Sabatier, el control de la temperatura y calor de reacción, representan los principales desafíos técnicos al diseñador de reactores. La degradación térmica o la deposición de carbón corresponden a los más comunes promotores de pérdida de actividad en los catalizadores de metanación [12]. Además, la reacción de Sabatier sufre de limitaciones cinéticas y termodinámicas a bajas y altas temperaturas respectivamente. Para hacer frente a estos desafíos técnicos, las metodologías convencionales de diseño y modelación de reactores se basan en el supuesto de que uno tubo es representativo de todo el sistema. La transferencia de calor se modela considerando coeficientes convectivos constantes o temperaturas fijas en las superficies del tubo como condiciones de borde de pared [7], [14], [15], [16]. En el caso de coeficientes convectivos constantes, muchas veces ase asumen excesivamente altos, [17], [18], [19], [13], que corresponderían a sistemas de enfriamiento basados en ebullición nucleada y no a sistemas convencionales basados en sales fundidas o aceite térmico [20]. En consecuencia, bajo estos supuestos, una realista distribución de temperatura y velocidades del flujo de refrigerante son ignoradas. Este enfoque, si bien es simple y económico en términos de consumo de recursos computacionales, asume que todos los tubos están expuestos a las mismas condiciones de refrigeración.

I.5 Definición del problema

De acuerdo con la revisión bibliográfica descrita en la sección I y detallada en la sección II, el problema de ingeniería a resolver en el presente trabajo queda caracterizado por los siguientes puntos principales:

- El mayor desafío técnico en el diseño de reactores de metanación es la remoción del calor de reacción y control de temperatura de reacción.
- El reactor tubular de lecho fijo es el concepto más adecuado para un rápido despliegue a escala industrial de la tecnología de metanación de CO_2 para el almacenamiento de energía renovable intermitente.
- El concepto de reactor tubular de lecho fijo actualmente adolece de una falta de conocimiento técnico sobre su operación bajo un régimen PtM.
- Los principales requisitos técnicos para que el concepto de reactor tubular de lecho fijo se implemente como una solución de ingeniería para respaldar las tecnologías Power to Methane son:
    - Capacidad para controlar la formación de puntos calientes (tamaño y temperatura máxima)
    - Capacidad para operar bajo interrupciones operativas de PtM relevantes (p.ej., temperatura de entrada, composición de la alimentación).
    - Preservación de la integridad térmica del reactor cumpliendo la concentración mínima de metano (en la corriente de salida) a inyectar a la red de gas natural, en operación PtM.
- Un modelo de medio poroso (PMM) con factor de efectividad (actividad) muestra un compromiso óptimo entre costos computacionales y precisión, especialmente en términos de balance de masa y cantidad de movimiento en el modelado/diseño de reactores de tamaño industrial.
- Solo los modelos basados en CFD son capaces de modelar adecuadamente el reactor industrial, en términos de variables críticas de diseño como la transferencia de calor entre el lado de la carcasa y los tubos, es decir, los patrones de flujo de refrigerante y la turbulencia.
- El enfoque de diseño de reactores más frecuente y tradicional se basa en modelos 1D (longitud, radio constante). Esto solo permite el cálculo del volumen requerido del reactor para lograr la conversión deseada, bajo el enfoque tradicional de diseño de reactor. Sin embargo, las

características críticas de diseño de flujo y transferencia de calor se pierden en dicho enfoque (por ejemplo, arreglo de tubos, arreglo de deflectores, efecto de las dimensiones del tubo, etc.).

I.6   Objetivos

I.6.1   Objetivo general:

Desarrollar una herramienta metodológica de diseño 3D CFD para reactores de metanación de CO_2 de lecho fijo tubular a escala industrial, sujetos a un contexto operacional Power to Methane.

I.6.2   Objetivos específicos:

- Desarrollar y validar un modelo 3D CFD capaz de representar los fenómenos de transporte esenciales: transferencia de calor y materia, en un reactor de lecho fijo tubular de metanación de CO_2 en régimen estacionario.
- Estudiar el efecto del flujo y tipo de refrigerante en la fracción molar de salida de CH_4 y temperatura máxima, en un reactor de lecho fijo tubular de metanación de CO_2 en régimen estacionario.
- Estudiar los efectos de las interrupciones operativas relevantes para el contexto PtM en la fracción molar de salida de CH_4 y temperatura máxima, en un reactor de lecho fijo tubular de metanación de CO_2 en régimen transiente.

El objetivo general se logrará por medio de un modelo numérico CFD, capaz de predecir el comportamiento del reactor bajo condiciones operacionales pertinentes al contexto PtM, el cual será previamente validado mediante información experimental disponible en la literatura relevante en condiciones estacionarias. Mediante el desarrollo del proyecto se espera generar información de valor para el diseño detallado de reactores politrópicos que operen en régimen transiente, y de este modo, promover el desarrollo de las tecnologías PtM.

I.7   References

[1]   "Renewable electricity – Renewables 2020 – Analysis," *IEA*. https://www.iea.org/reports/renewables-2020/renewable-electricity-2 (accessed Jul. 07, 2022).

[2]   UNFCCC, "What is the Paris Agreement? | UNFCCC," 2019. https://unfccc.int/process-and-meetings/the-paris-agreement/what-is-the-paris-agreement (accessed May 09, 2019).

[3]   "Solar PV – Analysis," *IEA*. https://www.iea.org/reports/solar-pv (accessed Jul. 06, 2022).

[4]   "Wind Power – Analysis," *IEA*. https://www.iea.org/reports/wind-power (accessed Jul. 06, 2022).

[5]   C. Barría *et al.*, "Política Energética Nacional," *Subsecretaría de Energía*, Feb. 2022, Accessed: Jul. 06, 2022. [Online]. Available: http://biblioteca.digital.gob.cl/handle/123456789/3857

[6]   M. Bailera, P. Lisbona, L. M. Romeo, and S. Espatolero, "Power to Gas projects review: Lab, pilot and demo plants for storing renewable energy and CO2," *Renewable and Sustainable Energy Reviews*, vol. 69, pp. 292–312, Mar. 2017, doi: 10.1016/j.rser.2016.11.130.

[7]   S. Rönsch *et al.*, "Review on methanation – From fundamentals to current projects," *Fuel*, vol. 166, pp. 276–296, Feb. 2016, doi: 10.1016/j.fuel.2015.10.111.

[8]   J. Kopyscinski, T. J. Schildhauer, and S. M. A. Biollaz, "Production of synthetic natural gas (SNG) from coal and dry biomass – A technology review from 1950 to 2009," *Fuel*, vol. 89, no. 8, pp. 1763–1783, Aug. 2010, doi: 10.1016/j.fuel.2010.01.027.

[9]   Y.-L. Kao, P.-H. Lee, Y.-T. Tseng, I.-L. Chien, and J. D. Ward, "Design, control and comparison of fixed-bed methanation reactor systems for the production of substitute natural gas," *Journal of the*

Taiwan Institute of Chemical Engineers, vol. 45, no. 5, pp. 2346–2357, Sep. 2014, doi: 10.1016/j.jtice.2014.06.024.

[10]   M. Götz *et al.*, "Renewable Power-to-Gas: A technological and economic review," *Renewable Energy*, vol. 85, pp. 1371–1390, Jan. 2016, doi: 10.1016/j.renene.2015.07.066.

[11]   N. Engelbrecht, S. Chiuta, R. C. Everson, H. W. J. P. Neomagus, and D. G. Bessarabov, "Experimentation and CFD modelling of a microchannel reactor for carbon dioxide methanation," *Chemical Engineering Journal*, vol. 313, pp. 847–857, Apr. 2017, doi: 10.1016/j.cej.2016.10.131.

[12]   K. Ghaib and F.-Z. Ben-Fares, "Power-to-Methane: A state-of-the-art review," *Renewable and Sustainable Energy Reviews*, vol. 81, pp. 433–446, Jan. 2018, doi: 10.1016/j.rser.2017.08.004.

[13]   S. Matthischke, S. Roensch, and R. Güttel, "Start-up Time and Load Range for the Methanation of Carbon Dioxide in a Fixed-Bed Recycle Reactor," *Industrial and Engineering Chemistry Research*, vol. 57, no. 18, pp. 6391–6400, 2018, doi: 10.1021/acs.iecr.8b00755.

[14]   A. Fache, F. Marias, V. Guerré, and S. Palmade, "Optimization of fixed-bed methanation reactors: Safe and efficient operation under transient and steady-state conditions," *Chemical Engineering Science*, vol. 192, pp. 1124–1137, Dec. 2018, doi: 10.1016/j.ces.2018.08.044.

[15]   J. Bremer, K. H. G. Rätze, and K. Sundmacher, "CO2 methanation: Optimal start-up control of a fixed-bed reactor for power-to-gas applications," *AIChE Journal*, vol. 63, no. 1, pp. 23–31, 2016, doi: 10.1002/aic.15496.

[16]   A. Alarcón, J. Guilera, and T. Andreu, "CO2 conversion to synthetic natural gas: Reactor design over Ni–Ce/Al2O3 catalyst," *Chemical Engineering Research and Design*, vol. 140, pp. 155–165, Dec. 2018, doi: 10.1016/j.cherd.2018.10.017.

[17]   D. Sun and D. S. A. Simakov, "Thermal management of a Sabatier reactor for CO2 conversion into CH4: Simulation-based analysis," *Journal of CO2 Utilization*, vol. 21, pp. 368–382, Oct. 2017, doi: 10.1016/j.jcou.2017.07.015.

[18]   E. Moioli, N. Gallandat, and A. Züttel, "Model based determination of the optimal reactor concept for Sabatier reaction in small-scale applications over Ru/Al2O3," *Chemical Engineering Journal*, vol. 375, p. 121954, Nov. 2019, doi: 10.1016/j.cej.2019.121954.

[19]   M. Martinez, C. Kern, and A. Jess, "Catalytic Hydrogenation of Carbon Dioxide to Methane in Wall-Cooled Fixed-Bed Reactors‡," *Chemical Engineering and Technology*, vol. 39, no. 12, pp. 2404–2415, 2016, doi: 10.1002/ceat.201500614.

[20]   T. L. Bergman, F. P. Incropera, D. P. DeWitt, and A. S. Lavine, *Fundamentals of Heat and Mass Transfer*. John Wiley & Sons, 2011.

II.   Literature Review

II.1   Intermittent renewable energy (IRE) storage

The increasing contribution of variable renewable energy (i.e., wind and solar photovoltaic "PV") in the electrical grids has imposed a substantial challenge to the energy system reliability. High levels of IRE penetration require balancing to safeguard the grid's stability, due to its hourly and seasonal variability, Figure 1.
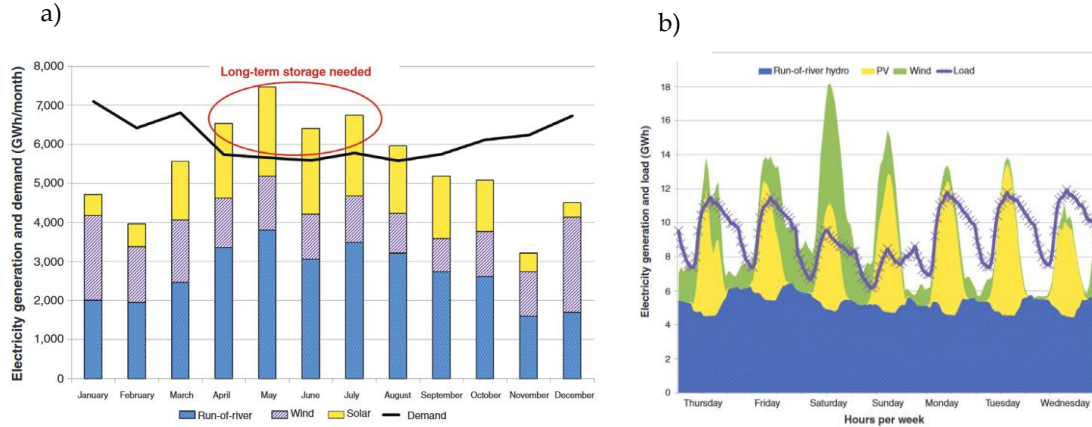
Figure 1. A 100% renewable energy mix based on hydro, PV and Wind. a) Monthly generation vs load. b) daily generation vs load. Source: [1]

Consequently, the engineering problem appears as an optimal compromise between an increment in intermittent renewable energy generation while at the same time minimizing the curtailment. Denholm & Mai (2019) illustrates this issue, proposing different IRE penetration scenarios for the US electricity generation mix. The main aim was to achieve an annual average penetration of 55% IRE by 2050 at minimum curtailment. Five scenarios, (Figure 2), were developed: PV only (55% PV), Wind only (55% wind), Equal (wind 27.5% and PV 27.5%), Wind vision mix (44% wind and 11% PV), and Minimum Curtailment (38% wind, 17% PV).
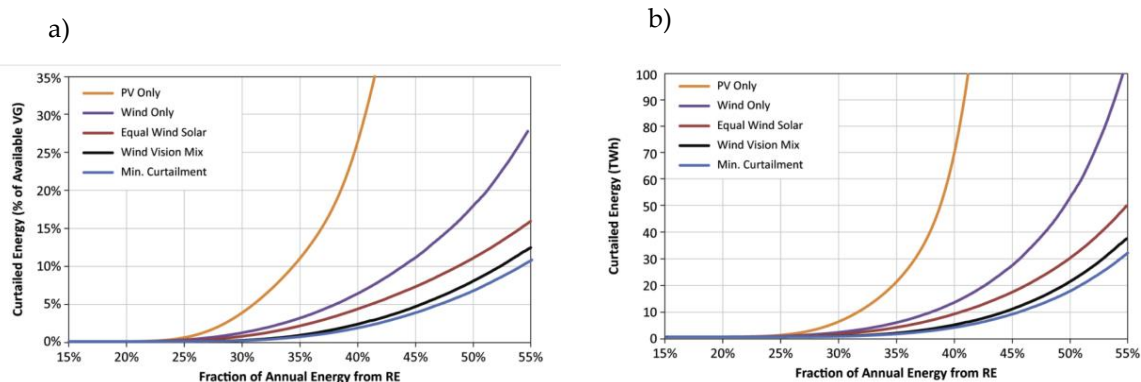
Figure 2. Total IRE curtailment rate (a) and energy curtailed (b) under increasing IRE penetrations, with no energy storage, and different mixes of wind and solar. Source [2].

According to (Denholm & Mai, 2019), the amount of curatailed energy depends on the wind and PV participation and the size of the storage system. A short term storage system (4 h), appeared as a the best cost-effective solution to integrate IRE up to a level of 55%. However, further IRE penetrations (beyond 55%) may only be achieved through the implementation of Long-Term (seasonal) Storage

system. In such case, the authors conclude that seasonal storage in the form of fuels may be a feasible alternative to mitigate long-duration curtailment events such as those ocurring in spring and summer, Figure 1.

II.2   PtX, solutions

Up to date, many state-of-the-art energy storage systems exist. Pumped hydropower, electrochemical storage and mechanical (flywheels) are already proven and reliable, Figure 3. Thermal energy storage, in the form of sensible and latent heat is becoming also an emerging alternative although mostly associated to solar energy storage [3] and district heating [4].
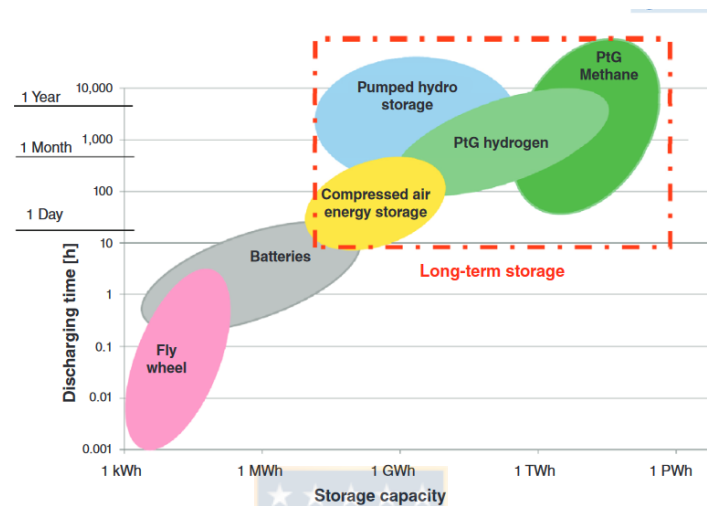
Figure 3. Intermittent energy storage alternatives. Source: [1]

However, they suffer from substantial limitations that hinder their implementation as an optimal IRE storage. Pumped hydropower appears as an excellent and proven alternative to store vast amounts of IRE [5]. However, its application is limited due to geographical requirements. Electrochemical storage using lead acid, nickel metal hydrides or lithium-ion batteries appear as a good alternative for short-term storage, due to energy density and power limitations. In particular, Lithium ion batteries show a high gravimetric energy density, however their deployment is constrained by its relative scarcity [6]. However, emergent storage systems like chemical storage offer both a large storage capacity and discharging time which makes it the most suitable alternative for seasonal/long term storage. Power to X systems [7], currently represent an ample range of chemical storage alternatives. They can provide a flexible alternative to accommodate hourly and seasonal IRE surplus in the form of gaseous or liquid fuels like: hydrogen, methane, methanol, ammonia or higher hydrocarbons [8]. Basically, it transforms the electrical surplus into hydrogen through electrolysis and then to other chemicals by means of different processes. Furthermore, Power to X (PtX) links the electrical grid to other energy sectors (e.g., heat and fuel), adding additional flexibility to the energy system facilitating the distribution of energy across different systems. For example, if the methane route is being used as a storage (Power to Methane), is not only possible to balance the electrical but the gas grid also [9]. At present the most relevant Power to X processes are:

1. Power to Gas/Power to Hydrogen (Water electrolysis), [10]
2. Power to Gas/Power to Methane (Sabatier process), [11]
3. Power to Liquids (Fischer Tropsch synthesis), [8]
4. Power to Methanol (Methanol synthesis), [12]
5. Power to Ammonia (Haber-Bosch process), [13]

An additional benefit of Power to X processes is the reduction of GHG (greenhouse gases) in the form of carbon capture and valorisation since processes 1 to 4 involve the use of CO_2 in addition to hydrogen as main reactants. Finally, in an increasingly unpredictable and complex international scenario, Power to X appears as a suitable alternative to increase the energy security, especially in countries lacking of substantial hydrocarbon resources [14]. Next subsections analyse the general features of each process and their main benefits and limitations. In addition, it is demonstrated that the most efficient and feasible Power to X process at the moment is the Power to Methane conversion route.

II.2.1   Power to Gas, Hydrogen (i.e., Power to Hydrogen, PtH)

Power to Gas (PtG) converts the electricity surplus into gaseous fuels (i.e., methane and hydrogen). Power to Hydrogen (PtH) being the simplest of all Power to X processes, is based on the production of gaseous or liquid (cryogenic) hydrogen after the step of water electrolysis. At the electrolyser's anode, oxidation takes place, and the generated electrons are consumed at the cathode reducing the water and producing hydrogen, Equations 1-3.

$$Anode: H_2O \rightarrow \frac{1}{2}O_2 + 2H^+ + 2e^- \quad (1)$$

$$Cathode: 2H^+ + 2e^- \rightarrow H_2 \quad\quad (2)$$

$$Overall\ reaction: H_2O \rightarrow \frac{1}{2}O_2 + H_2 \quad\quad (3)$$
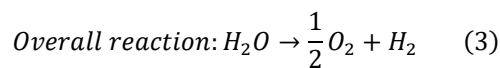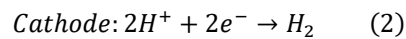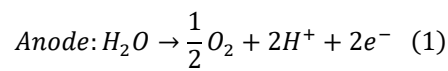
Hydrogen offers interesting benefits in terms of emission reductions since it only generates water as a combustion product. Thus, SOx, PM and CO_2 are entirely avoided. However, NOx emissions are promoted through Fenimore [15] and Zeldovich [16] mechanisms (thermal NO formation). In addition, its implementation requires fewer energy conversion steps than other renewable fuels like methanol, SNG and ammonia. Still, several technological drawbacks hinder the implementation of hydrogen as energy storage alternative. Its low volumetric energy density made compressed hydrogen non-feasible when volume is restricted (aircrafts and maritime transport), while liquid hydrogen LH_2 (-253°C at 1 bar) requires special materials to withstand extreme cryogenic conditions [17]. Furthermore, its low minimum ignition energy 0.02 J, (0.29 for methane) [18] may prompt extreme pre-ignition effects related to the air-fuel ratio and inlet temperature, if used in internal or external combustion engines. Additionally, its low auto-ignition temperature makes hydrogen less suitable to be used as sole fuel in Diesel Cycle engines, which is a critical issue to decarbonize non electrifiable transportation like the heavy maritime freight sector replace with [19]. Finally, there are important safety concerns involving the use of hydrogen. Due to its small molecular size, a loss of containment event will primarily occur through very small leakages leading to gaseous release and dispersion. If no proper ventilation system is supplied, the accumulation of gaseous hydrogen may lead to asphyxiation and the formation of combustible (4-75% v/v) or explosive (18-58%) mixtures. Currently the most auspicious use for hydrogen lies in the transport sector combined with Proton Exchange Membrane (PEM) Fuel Cells (FC) [20]. Current Power to Hydrogen systems, show an efficiency of 77% with the respect of the lower heating value (LHV) of the product gas and the input electrical load [10].

II.2.2   Power to Gas, Methane (i.e., Power to Methane, PtM)

Up to date, catalytic heterogeneous methanation is the suitable and common method to achieve CO_2 hydrogenation into methane, while biological methanation is still at a pilot scale and also suffering from scale up problems due to lower reaction rates [11]. If a subsequent step is added to the hydrogen path, the process is then called "Power to Methane" (PtM). Hydrogen reacts with CO_2 in the Sabatier process (catalytic methanation), Equation 4, to generate methane and water.

$$4H_2 + CO_2 \rightarrow CH_4 + 2H_2O \; \Delta H_r^{298\,K} = -\frac{165kJ}{mol} \quad (4)$$
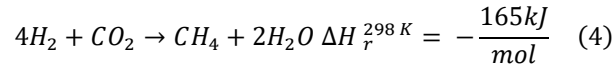
Solid metal catalysts (Ni, Rh, Ru, Co) supported on metal oxides are commonly used, while reaction conditions range from 1-100 bar and 200-550°C [21].
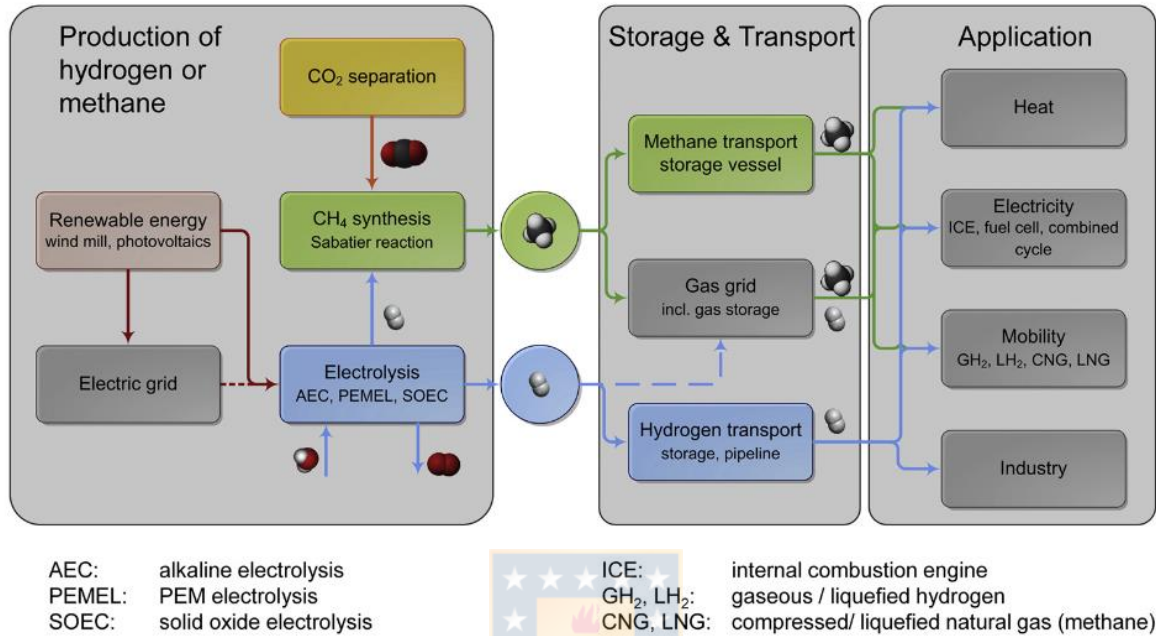
Figure 4. Power to Gas (methane and hydrogen) production flowchart. Source: [22]

The produced methane can be utilized as substitute/synthetic natural gas (SNG) in power generation, households and as a feedstock to the chemical industry. Regarding the process efficiency, if reaction heat recovery is considered, up to a 79% can be attained. Without off-heat usage, the process efficiency drops to 41% [10]. One of the greatest advantages of PtM over other PtH is that methane storage overcomes the considerable difficulties associated with large scale hydrogen storage. SNG can be stored, without any restriction, in the existent natural gas network. In other words, SNG is a direct substitute for fossil natural gas (i.e., similar composition, heating value, means of transport and management). Finally, the synthesis of methane from CO_2 is the simplest H_2 storage route in terms of auxiliary equipment and storage, making it the best alternative to small or decentralized scale applications [23, p. 3].

II.2.3   Power to Liquids (PtL)

Power to Liquids (PtL) involves a step of hydrogen production through electrolysis, CO_2 capture, and higher hydrocarbons synthesis, Figure 5. Panzone et al. [6] reports an ample variety of Power to Liquid processes (e.g., ammonia, higher hydrocarbons, methanol, Dimethyl ether "DME"). Simple storage requirements and great energy density make liquid fuels a very interesting alternative to the transport sector specially the maritime [24] and aviation [25].
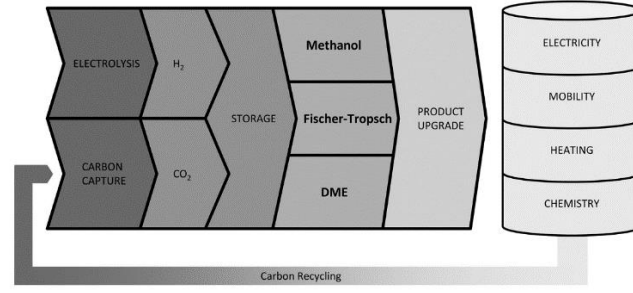
Figure 5. Power to Liquids production flowchart Source: [26]

By means of the well-known Fischer-Tropsch synthesis, it is possible to convert the hydrogen and CO_2 stream intro higher hydrocarbons. The direct conversion of CO_2 into higher hydrocarbons is still at a very early research stage [8]. Instead, the CO_2 stream must be first converted into CO and water by means of the Reverse Water Gas-Shift reaction, Equation 5. Then, the produced syngas is further converted into higher hydrocarbons in the traditional FT process, Equation 6.

$$H_2 + CO_2 \leftrightarrow CO + H_2O \ \Delta H_r^{298\,K} = +\frac{41kJ}{mol} \quad (5)$$

$$2H_2 + CO \leftrightarrow (-CH_2-) + H_2O \quad (6)$$
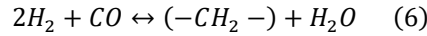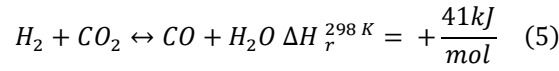
Efficiency for FT based PtL, is lower than other PtX processes. Panzone et al. [6] reported a range of 42-64% efficiency for FT-PtL, depending on the CO_2 source, electrolysis type and process specifications. In order to maximize the CO conversion, it is very important to adjust H_2/CO ratio at 2.15 for high temperature, 290-360°C, iron based FT and at around 1.7 for the low temperature, 180-260°C, on cobalt catalysts [27]. FT process is conducted at an industrial scale at high pressures (1-4 MPa) [28]. The most important and perhaps the sole application for FT-PtL is as aviation fuel. Currently the only alternative to synthetize 100% renewable aviation fuels is through the FT-PtL route [25], [29].

At an industrial level methanol is currently produced from methane (natural gas) via steam reforming and a CO (syngas) hydrogenation process, like the well-known *Lurgi MegaMethanol™* [25] usually at 50-100 bar and 200-300°C. Normally this process is conducted on Cu-Zn catalysts supported on Al_2O_3 [12], Equation 7 and 8.

$$2H_2 + CO \leftrightarrow CH_3OH \ \Delta H_r^{298\,K} = -90.64\frac{kJ}{mol} \quad (7)$$

$$3H_2 + CO_2 \leftrightarrow CH_3OH + H_2O \ \Delta H_r^{298\,K} = -49.67\frac{kJ}{mol} \quad (8)$$
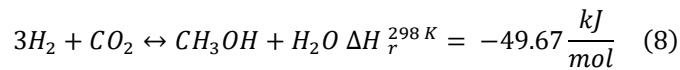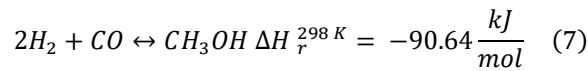
According to Moioli et al. [18], at least theoretically, the Power to Methanol process is able to store 85.3% of the hydrogen energy (on a LHV basis) against 78-79% in the PtM process. Still, substantial technological drawbacks still give PtM a significant advantage over Power to Methanol. PtM requires less down and upstream equipment and processes, in contrast to Power to Methanol which requires a recycling loop (which demands an additional compressor) and therefore additional preheating stage. Furthermore, if a two-step hydrogenation process is considered, an additional RWGS reactor is required. If no energy integration exists, the losses due to pre-heating and compressing may reach 11.3% (with a recycling) and a further 21.3% of a RWGS reactor is added [31].

Uebbing et al. [27] concluded similarly by comparing methane and methanol as energy storage alternatives. Comparing the exergy flow of the product streams (on a heating value basis), methanol performs better than methane (CH_3OH 541 kW, CH_4 495 kW). However, the author detected a

significant difference in exergetic efficiency between the two processes. The main reason is the high electrical consumption in the methanol process due to the elevated reactor operating pressure (5 MPa against 1 MPa). Moreover, the considered methanol process requires a distillation unit and a reboiler, incurring in additional energy losses and required equipment, which makes Power to Methanol, unsuitable to small scale or decentralized applications [31]. Finally, the methanation reaction is more exothermic than the methanol synthesis ΔH_{CH4} = -164 kJ/mol, ΔH_{CH3OH} = -49.6 kJ/mol, allowing for better heat recovery integration.

Ammonia offers much of the same benefits as hydrogen, like carbon-free combustion and a better capability to operate as fuel in compression combustion engines [24]. Furthermore, its storage and transport show significant advantages over H_2 since it can be liquified at -33.4°C at atmospheric pressure. Unlike liquid H_2, ammonia has dragged the interest of big engine makers to develop marine four-stroke combustion engines for the shipping sector like Wärtsilä, Repsol and Knutsen OAS Shipping [33]. Still, some technical issues remain like ammonia is highly toxic and corrosive. In addition, it has poor combustion properties like slow flame speed, poor ignition, and higher NOx emissions [24]. Outside the energy sector, NH_3 remains relevant for nitrogen fertilizers production, nitric acid and as a refrigerant [13]. Currently Power to Ammonia shows a systems efficiency of 74% considering heat recovery [34].

II.2.4   Biogas as CO_2 source

In addition to IRE as hydrogen supply, a suitable CO_2 source appears as the second primary input for the methanation process. Current CO_2 sources are the thermal power generation plants (combustion), cement plants, industrial processes like steel mills (blast furnace and coke oven gas), atmospheric air and anaerobic digestion [35]. However, the capture of CO_2 from these sources carries with its own technical difficulties. Although technically feasible, the low CO_2 partial pressures in blended sources (combustion, steel mill gases, cement plants and air) makes the separation process complex and energetic intensive [36]. High order hydrocarbons, H_2S, CO, NH_3 and most of all, atmospheric N_2, need to be properly separated (e.g., Water absorption, membrane separation, scrubbing, pressure swing adsorption) [11]. However, biogas plants stand out as a good quality CO_2 source that can be incorporated in the methanation process without considerable additional costs. In the absence of cost efficient separation processes it is considered the best source of CO_2 for methanation [35]. As of 2019, most pilot or demonstration scale methanation plants use biogas or sewage gas as the main source of CO_2 [10]. Biogas composition consists mostly of methane (50-70%) and CO_2 (30-50%), H_2S and small traces of siloxanes and mercaptans [37], which need to be properly removed since they are mostly harmful for any catalysts due to poisoning [21]. A biogas based PtM process is depicted in Figure 6.
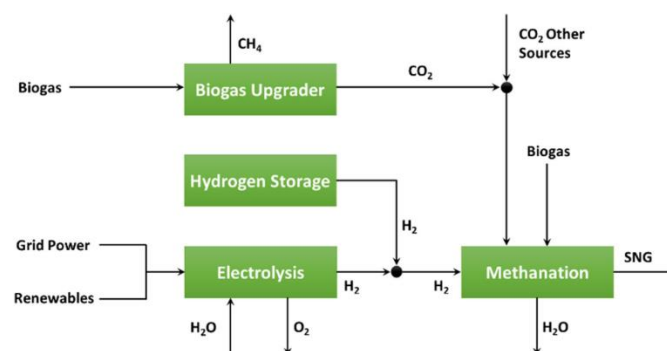
Figure 6. Biogas upgrade into SNG through CO_2 methanation. Source [37]

II.3 Technological challenges in methanation reaction design

Although most CO_2 methanation research groups do not publish design details of their reactors, still two broad classifications can be identified: according to the temperature profile, and design concept. Three temperature profiles are identified based on the reactor´s heat exchange characteristics namely, adiabatic, isothermal and polytropic. Adiabatic considers a reactor with no heat exchange. Isothermal corresponds to any reactor whose heat exchange rate allows to maintain a distinct uniform temperature in the whole reactor. While a polytropic reactor is characterized by a non-uniform temperature profile across its boundaries. In regards to reactor design the main types are: Fixed-bed (polytropic and adiabatic), structured (honeycomb, monolith, microchannel, metallic foam), Bubbling fluidized bed and Slurry bubble column [10], [21].

II.3.1 Heat management

Due to the Sabatier reaction high exothermicity, heat release and temperature control remain the leading challenges to the reactor designer. Thermal degradation and coke deposition are common heat-induced activity loss mechanisms in catalysts [21]. Furthermore, the methanation reaction suffers from kinetic and thermodynamic limitations at low and high temperatures respectively. According to Rönsch et al. (2016) the initial classification of methanation reactors is based on their heat dissipation performance and temperature profile in accordance with the Seminov number [38]:

$$Se = \frac{Da_I \cdot B}{St} = \frac{Heat\ production\ rate}{Cooling\ rate} \quad (9)$$

Where Da_1 is the first order Damköhler number (ratio of the reaction rate and the convective mass transport rate), B the heat production potential and St, the Stanton number (ratio of heat transferred into a fluid to the thermal capacity of fluid).

- $Se \rightarrow \infty$, Adiabatic temperature profile: Usually, tubular fixed bed reactors without cooling adopt an adiabatic behaviour with a distinct hot-spot at the reactor outlet. Recycle and interstage cooling are usually incorporated as temperature management.

- $Se \rightarrow 0$, Isothermal temperature profile: Fluidized bed reactors, three phase reactor (slurry bubble column) are considered to operate almost under isothermal conditions.

- $0 < Se < \infty$, Polytropic (i.e., cooled reactor) temperature profile: Common to cooled fixed bed, monoliths and structured reactors. Contrary to the adiabatic profile, cooled reactors will always show a distinct hot-spot near the inlet where the reactants concentration is higher. Product gas leaves the reactor at moderate temperatures due to wall cooling. The great advantage of the polytropic profile is that at the reactor´s entrance (hot-spot area) a fast conversion zone appears dominated by kinetics, while downstream the lower temperature (due to active cooling) allows to overcome some of the thermodynamic limitations due to the presence of products (methane and water).

II.3.2 Methanation reactors: Limitations and advantages

Adiabatic Fixed bed reactors, Figure 7: are the most prevalent concept in CO_2 methanation [39]. Adiabatic reactors, [40], [41], consist of a cascade process with interstage cooling and usually at least one recycle loop. Additionally, interstage water removal may be included to further enhance CO_2 conversion. Adiabatic reactors are simple to construct and also provide for good heat recovery through steam generation between stages. However, they suffer from poor dynamic behaviour in front of sudden changes of feed composition or inlet temperature [42], in addition to additional auxiliary

equipment (recycle compressor and heat exchangers). Current commercial methanation technology is only available in the adiabatic concept from the following manufacturers: Etogas, Outotec and MAN.
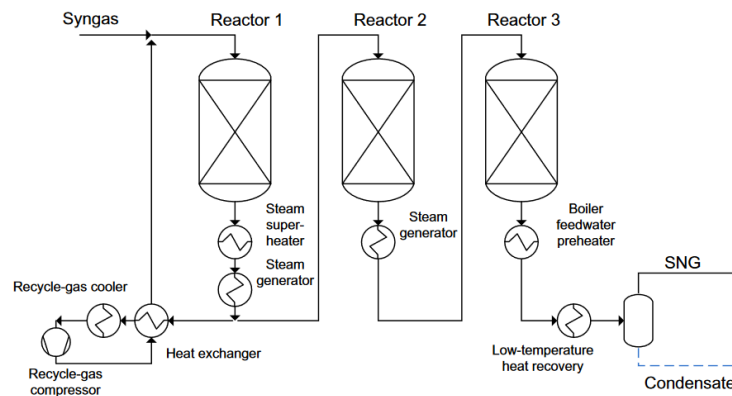
Figure 7. Adiabatic methanation concept from Haldor Topsoe (TREMP methanation). Source [21].

Polytropic Fixed-Bed reactors, Figure 8: also called tube bundle reactor, wall cooled reactor and tubular reactor [43], [44] consist of an array of tubes in parallel, whose number is determined by the required production rate, while their length and diameter are selected to optimize the heat exchange area [39]. In order to overcome radial heat transport limitations, smaller diameters are usually preferred (5-25 mm), [45]. Most of the current CO_2 methanation theoretical and experimental research works, [46], [47], are focused on this concept for its potential to be deployed as an industrial solution in the near future. Their main drawback is their capability to withstand sudden operational condition changes (inlet composition, temperature etc.) [8],[16]. However, the mentioned limitations seem contradictory to the fact that the only concept to be experimentally proved under PtM conditions is the Polytropic Fixed-Bed reactor [44].
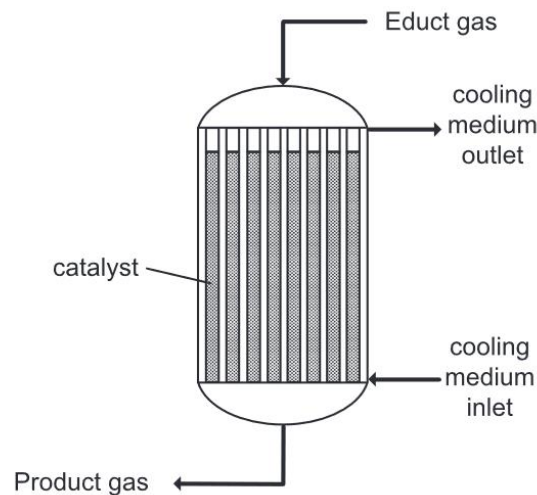
Figure 8. Tubular (polytropic) methanation reactor concept. Source [48].

Monolith, Figure 9 a) and microchannel reactors, Figure 9 b): [49], [50], [51] they offer a high specific surface area, small pressure drop (due to high porosity) and usually they tend to reach the steady state quickly than other reactors. However, ceramic monoliths are brittle, and both reactor types are single use (if deactivation occurs, the whole reactor needs to be changed).
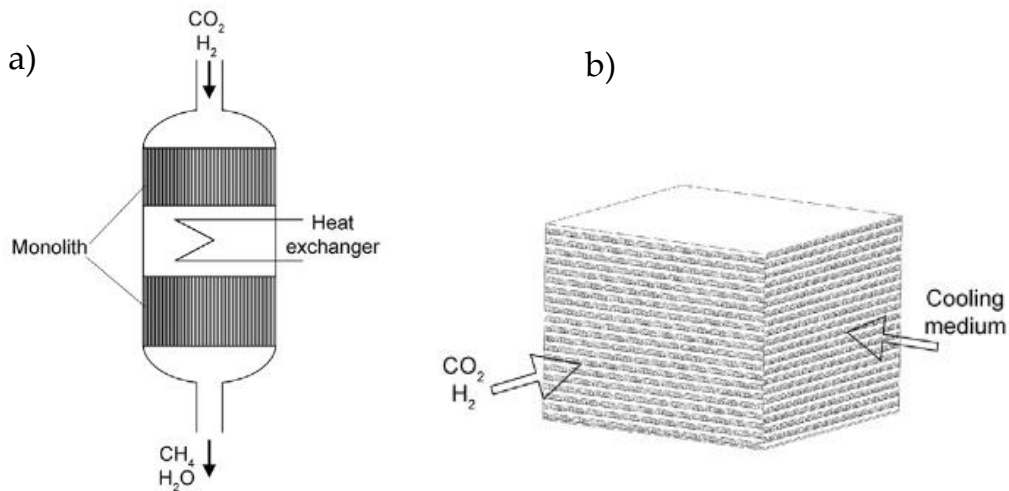
Figure 9 a) Monolith reactor concept. 9 b) Methanation microchannel module. Source: [39].

Membrane reactors, Figure 10: [52], [53] allows for better temperature control since H_2 and CO_2 are fed separately, therefore the reaction rate can be adjusted in the longitudinal direction, avoiding hot-spot formation. Additionally, making use of the Le Chatelier's principle, it is possible to remove water from the product stream allowing for a shift in the equilibrium to the right side, increasing the selectivity towards CH_4. Their main drawbacks are the membrane costs and necessity to change them at periodical intervals.
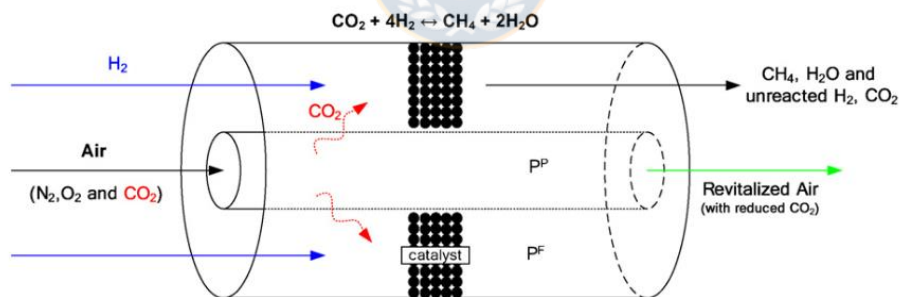
Figure 10. Membrane methanation reactor for air purification. Source [52].

Sorption-enhanced reactor, Figure 11: [54] like membrane reactors, they are based on the Le Chatelier's principle by removing H_2O from the reaction zone through a high adsorbent material mixed with the catalyst bed. The loaded adsorbent must be continuously renewed; therefore, the reactor has a short lifetime and may be not suitable to industrial applications.

Bubbling fluidized bed reactor, Figure 12: [55], [56], inherently suited to highly exothermic reaction due to their isothermal flow properties. Mass and heat transfer are greatly promoted by turbulence and better surface contact between catalyst and gas. Although optimal from a thermal point of view, fluidized bed reactors tend to consume large quantities of catalyst due to attrition losses, [21].
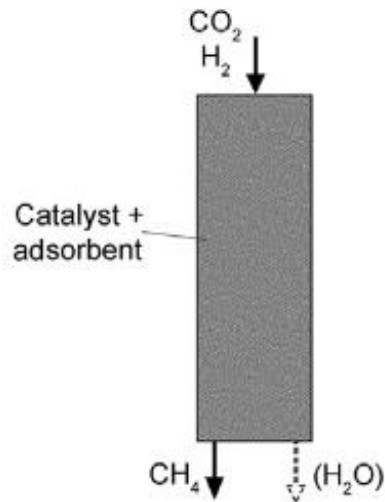
Figure 11. Sorption enhanced reactor concept. Source: [39].
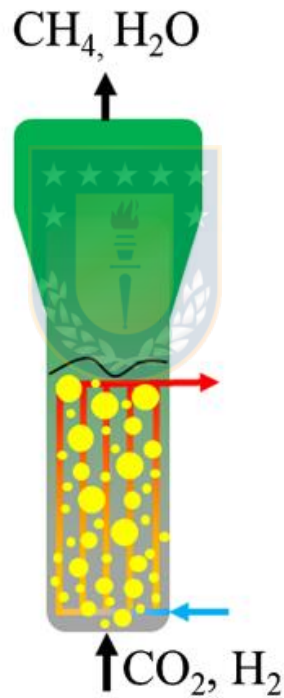
Figure 12. Bubbling fluidized bed reactor concept. Source: [55].

Slurry bubble column reactor, Figure 13: [48], three phase reactors are characterized for almost ideal isothermal conditions without attrition induced catalyst loss. The high heat capacity of the liquid phase allows for good temperature control, especially under dynamic operation. However, the high mass transfer limitations imposed by the liquid gas interphase still leaves this concept in the development stage for CO_2 methanation.
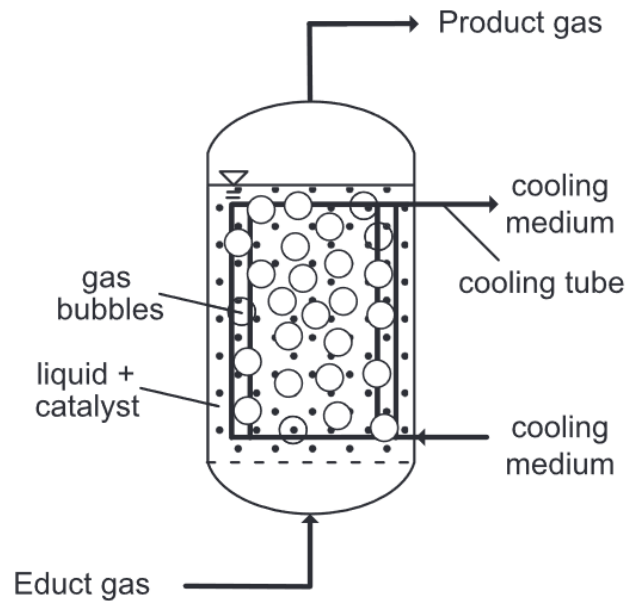
Figure 13. Slurry Bubble reactor concept. Source: [48].

II.4 Reactor modelling theoretical background

In general, there are two approaches for fixed bed reactor modelling. A CFD modelling approach, which gives the velocity field by solving the Navier Stokes Equations for fluid flow, and non CFD modelling approaches, which estimate the pressure drop across the bed usually with the aid of an empirical expression like the Darcy law. Although the present work focuses on CFD modelling, non CFD models are also considered for its relevance in the field of Power to Gas. Two methodologies stand out as the most relevant in the field of fixed bed reactor modelling: "Particle Resolved CFD models" (PRCFD) or heterogeneous reactor model, in which a true solution for the fluid field and porous matrix is attained. On the contrary, simplified approaches like "Eulerian-Eulerian" or "Porous Media Model" (PMM) ignore the presence of catalyst particles and the whole catalytic bed is assumed as a continuum [57]. Since the focus of this work falls in the field of industrial multitubular reactors modelling, PRCFD will only be briefly discussed. Currently, tubular reactors, whether they are based on pelletized or structured catalysts, still have the utmost relevance in the field of reactor modelling and simulation. Consequently, the shell and tube configuration remain an attractive alternative for PtM reactors.

II.4.1 Heterogeneous Reactor Model (PRCFD)

The most realistic representation of a packed or fixed bed is carried on models, which can reproduce the heterogeneous mixture of both solid and gas phase. These heterogeneous models, rely on a randomly generated particle matrix (mostly spherical in shape) to depict explicitly mass and energy transfer phenomena between bulk (gas) and particle (solid) phase. As particles true geometry is present in the model, this approach can reproduce accurately complex flow features like turbulence (vortex formation/dissipation) [58]. However, due to the extreme demand of computational resources (3000 times the computational cost of the equivalent PMM), this modelling approach remains suitable only for small geometries, where the main interest lies in the fluid flow, and therefore, large catalyst size > 6 mm or low tube-to-particle diameter ratios ($d_t/d_P < 4$) are used [59].

II.4.2 Eulerian-Eulerian (PMM)

Plant engineering design demands simulation capability for large, mostly 3D, multitubular chemical reactors. This strict requirement can only be met through PMM models [1]. A decisive advantage of the

Eulerian-Eulerian approach is its computational inexpensiveness. Both phases are represented as a continuum; discrete particles are not explicitly modelled. Phase conditions and properties on each cell are volume averaged and adjusted with its proper volume fraction. In addition, interaction between phases is included by means of source terms which account for momentum, energy and mass transfer. Nevertheless, this approach still presents some drawbacks. PMM assumes that catalyst particles are uniformly distributed along the reactor bed. This means that species generation/consumption takes place everywhere like a volumetric (homogeneous) reaction. Even so, PMM still allows the assessment of important engineering design features like the temperature increase and pressure drop. In addition, as the porous matrix is not physically present, its effects on the flow must be taken into consideration through accurate mean porosity estimation.

II.4.3   Mean Porosity in Packed Beds

Mean porosity for spherical packings (φ), usually lie between 0.25-0.47 [60]. An appropriate porosity value is of utter importance in the study of fixed bed reactor performance, since it directly influences two of the most important design features: pressure drop and catalyst load. Although smaller particle diameters (< 1mm) and non-uniform shapes are useful for better heat removal and process intensity [61], it is also true that it may severely impact the pressure drop, because they tend to form an increasingly "compact" bed. As stated by Méndez [62] spherical catalyst pellets of 2–4 mm diameter are recommended, which is also the range for commercial methanation catalyst . In addition, an accurate estimation of the porosity will lead also to a proper estimation of the catalyst mass (1- φ), and therefore, of the reactive phase. The key design parameter for an accurate estimation of the mean porosity is the tube to particle diameter ratio (d_t/d_P). According to Foumeny [63] the maximum φ value (for spherical packings) correspond to 0.67 for a d_t/d_P=1.62, while a constant minimum value of 0.39 appears for d_t/d_P > 10. Likewise, advantageous flow conditions (minimization of wall effects) demand a d_t/d_P of at least 10 [64]. The reader is directed to the contributions of Méndez [62] for useful correlations to estimate mean porosity.

II.4.4   Momentum Balance in PMM

The most relevant parameter to characterize any kind of flow whether they are internal or external, is the Reynolds number. A common expression used in packed beds is defined [60]:

$$Re_{dp} = \frac{\rho_g U d_p}{\mu_g} \quad (2)$$

Where Re_{dp} is the Reynolds number based on the particle diameter, ρ fluid density, U mean flow velocity, based on the superficial velocity formulation, d_p particle diameter and μ dynamic viscosity. Based on Equation 2, the flow can be categorized in the following regimes: laminar (Re_{dp} < 10), transitional (10 < Re_{dp} < 300) and fully turbulent (Re_{dp} > 300) [65]. Nevertheless, Baker [66] suggests that to better characterize the flow through porous media, an appropriate expression should include the mean porosity either as an expression based on particle diameter, Equation 3 or tube diameter, Equation 4 [66], [67]:

$$Re_p = \frac{\rho_g U d_p}{\mu_g(1-\varphi)} \quad (3) \qquad\qquad Re_{dt} = \frac{\rho_g U \varphi d_t}{\mu_g} \quad (4)$$

PMM assumes a mean value for bed porosity and the velocity is calculated from the volumetric flow (Superficial Velocity Formulation). This approach provides an accurate description of the bulk pressure loss across the porous matrix. But the validity of the Reynolds number relies on the physical velocity and real particle length. Consequently, the absence of a real solid matrix, hinders the validity of the Reynolds number. To capture turbulent flow features, all confining geometry must be clearly defined. Large turbulent structures (eddies) are driven by the kinetic energy the gain from viscous stresses and

strains from fluid-wall interchange. Smaller eddies are viscosity dependent and governed by Kolmogorov length scales [58]. In addition, the porous matrix induces re-lamination, in which flow through different pore sizes (large converging to small) damp out large scale eddies [66]. Clearly, a PMM does not allow the study of secondary flows, such as re-lamination, separation, and vortex formation, since the physical structures that give rise to turbulence are not present and the velocity is based on a volumetric approximation. Regarding turbulence modelling in PMM, Zhang [68] and Gao [69] reported that for a transitional regime (Re_{dp}=67 Equation 2) there is no significant effect on the thermal behaviour of the bed, whether a laminar or turbulent model is chosen. Guardo [70] and Gao [69] recommended the Spalart–Allmaras turbulence model to be included for Re_{dp} in the transition to turbulent regimes (Re_{dp} = 67 equation 2) in PMM. However, Guardo [70] simulated the fluid flow and heat transfer in a nonregular packing bed (PRCFD), therefore their conclusions are not applicable to continuum models. In the same way, Jiang [71] following the recommendation from Guardo [70], simulated a multi-tubular fixed bed reactor using a laminar and the Spalart-Allmaras model. They also concluded that no significant differences were found for a transitional flow regime (23-436). Following the experiences of Gao [69] and Jiang [71], it can be concluded that both laminar and turbulent models are appropriate to predict the hydrodynamic of the gas–solid flow and catalytic reaction in the fixed-bed reactor. Hence, the inclusion of turbulence models in PMM appears futile, since industrial fixed bed tubular reactors operate under relatively low superficial velocities (1-3 m/s) to avoid an excessive pressure drop.

II.4.5 Mass balance in PMM

II.4.5.1 Mass diffusion model

Fick's law appears as the basic approach to model mass fluxes in continuum models [72] where the flux of a component is proportional to the gradient of the species concentration. Nevertheless, this constitutive "law" is strictly valid only in the following circumstances: diffusion of a dilute specie in a multicomponent mixture, binary mixtures and absence of significant body forces [73]. In general, this approach may suffice when the species mass fraction is <<1, except for the solvent or carrier gas [72]. On the contrary, if no specie can be identified as a solvent, being all concentrations of the same order of magnitude, a multi-component diffusion approach is recommended to account for molecular interactions among species. As an alternative to the Fickian approach, the Maxwell-Stefan equations [74] can be used to derive mass fluxed in multicomponent systems in which species concentrations are of the same order of magnitude. Binary diffusivities are usually obtained through "kinetic theory" based correlations like Chapman-Enskog [75] or Fuller [76]. A simpler model for mass diffusivity coefficients estimation in multicomponent mixtures is the well-known Wilke correlation [77]. Both Wilke and Maxwell-Stefan models assume exclusively bulk diffusion whereas the dusty gas model and Wilke-Bosanquet are used to describe the combined effect of both bulk and Knudsen diffusion fluxes [78]. Nevertheless in cases where molecular transport processes are significant, like diffusion dominated laminar flows, the Maxwell-Stefan approach is encouraged [79]. The most complete diffusion modelling approach will take into consideration an effective axial and radial dispersion coefficient. However, if plug flow behaviour is ensured, radial dispersion effects may be neglected under the following conditions: ratio of catalytic bed length to catalyst particle (L_{bed}/d_P) > 150 and internal reactor to particle diameter, d_t/d_P >10 [64]. Besides, the dispersion coefficient in the axial direction is at least five times greater than the radial dispersion coefficient for $Re_{dp} > 10$. In fact, radial dispersion can be completely neglected in the turbulent regime $Re_{dp} > 300$ [80].

II.4.5.2 Chemical reaction model

The discussion of whether pseudo-homogeneous or heterogeneous models represent chemical reaction phenomena properly has been presented in detail in classic [81] and recent works [53], [82]. Essentially, most continuum models work under the assumption of the pseudo-homogeneous hypothesis, which

means that resistances to mass transfer occurring between the solid phase and fluid phases are negligible, assuming that the catalyst surface is exposed to bulk fluid conditions and intraparticle diffusion effects are ignored. Nevertheless, it is still possible to include heat and mass diffusional limitations in using a PMM. Regarding mass transport limitation, usually it is easily incorporated in continuous models by means of the well-known effectiveness factor [81]. In addition Matthischke [40] considered diffusion limitations through a constant activity factor. Only minor differences were observed between pure heterogeneous or pseudo-homogeneous model with variable effectiveness factor, and a pseudo-homogeneous model with constant activity factor. However, a reduction in one order of magnitude in computational time resulted from the latter approach. If experimental data is available, an "scaling factor" will be necessary to incorporate alongside the rate law to calibrate the whole kinetic expression (intrinsic rate law + effectiveness factor) to experimental data [82], [68]. Despite heterogenous reactions can only be modelled explicitly through PRCFD as stated before, it is still possible to include a particle mass balance in PMM with the aid of an "external 1D particle model" which is related to the 3D or 2D continuum model through energy and mass balance equations [83]. COMSOL makes use of this strategy through the "Reactive Pellet Bed" feature available in the "Transport of Diluted Species" model of the same software. As already stated by Schlereth [53] and Parlikkad [84] the inclusion of a full heterogeneous model seems only justifiable, when severe mass and heat transfer limitations are expected i.e.: large catalyst pellets, small pore radii and small Reynolds numbers.

II.4.6   Energy balance in PMM

Concerning the treatment of the energy conservation equation in PMM models the default approach considers both phases in thermal equilibrium, which is the basic assumption of pseudo-homogeneous models [81]. An equilibrium model relies on an effective thermal conductivity computed as the volume average of the fluid conductivity and the solid conductivity. Nevertheless, this assumption may not be acceptable for transient simulations and industrial size reactors. Hence, an energy balance which allows for heat transfer between phases is desirable. ANSYS FLUENT employs a dual cell method, where a spatially coincident solid/porous-fluid zone, interact only regarding heat transfer. Energy balance between phases is then achieved by means of a surface heat transfer coefficient calculated according to [67] and the "interfacial area density, which is the ratio of the fluid/solid interface and the volume of the porous zone volume. If the effective radial thermal conductivity is to be included, the reader is directed to the methodology proposed by Martínez [45]. In regard to heat transfer by radiation, in fixed bed reactors operating at temperatures below 400°C [85], the radiative heat transfer is negligible in comparison to conductive and convective mechanisms occurring inside the bed. Radiation becomes important usually in reformers, where maximum operational temperatures may be as high as 1273 K [86]. In such cases, catalyst surface optical properties must be also considered since they may further reduce radiation mean beam length.

II.4.7   Turbulence models and near wall treatment in shell side (coolant flow)

One of the key objectives of this study is precisely to give some insights regarding shell side flow modelling in tubular fixed bed reactors. As very few reactor studies consider the coolant system, there is no detailed methodology regarding the modelling of the shell side flow. By analogy, it is possible to consider the multi-tubular reactor as a shell and tube heat exchanger. Indeed, multi-tubular reactors have been successfully designed according to Tubular Exchanger Manufacturers Association "TEMA" standards using a correlation based approach [87]. In this field, turbulence simulation plays a paramount role. The standard k-ε model together with standard wall functions, correspond to the basic approach for its robustness, accuracy and computational economy [88], and it is the standard model for current multitubular reactor models [89], [90]. Still, this approach may not be suitable to flows involving

curved geometries and swirling flows. Although the Re-Normalisation Group (RNG) k-ε model [91] corrects the deficiencies of the standard k-ε [92] improving the prediction of the near-wall flow, the realizable k- ε model can provide a better performance for flows involving moderate swirl and vortex shedding behind bluff bodies [93], [94], [95]. In addition it has been reported that RNG models are harder to converge than Realizable [79]. An even superior alternative but also computational demanding may be found in k-Ω SST model. This model shows superior performance for wall-bounded boundary layer and low Reynolds numbers, features that are of especial interest to solve the drastic thermal transfer on tube walls in sections where hot spot is expected as shown in similar heat exchanger simulations [96], [97]. Unlike k-ε models , k-Ω models are very demanding in terms of mesh refinement, , and they don't rely on wall functions to solve the boundary layer, instead they fully solve the Viscous Sub-layer region completely [58]. Consequently, the first grid cell needs to be at y+ ≈ 1, which in turn significantly increases the mesh count. On the contrary standard wall function are usually preferred to simplify the model and save computation time, therefore mesh refinement is done to guarantee 30<= y+ <= 300. However, parametric studies involving changes in the mean flow velocity and consequently the y+ value, scalable or enhancement wall treatment approaches, are a better option to avoid the successive mesh refinements proper of a standard wall function approach [94].

II.5   References

[1]   A. Ajanovic and R. Haas, "On the long-term prospects of power-to-gas technologies," *WIREs Energy and Environment*, vol. 8, no. 1, p. e318, 2019, doi: 10.1002/wene.318.

[2]   P. Denholm and T. Mai, "Timescales of energy storage needed for reducing renewable energy curtailment," *Renewable Energy*, vol. 130, pp. 388–399, Jan. 2019, doi: 10.1016/j.renene.2018.06.079.

[3]   İ. Dinçer, "Numerical Modeling and Simulation," in *Thermal Energy Storage*, John Wiley & Sons, Ltd, 2021, pp. 383–483. doi: 10.1002/9781119713173.ch5.

[4]   D. Romanchenko, J. Kensby, M. Odenberger, and F. Johnsson, "Thermal energy storage in district heating: Centralised storage vs. storage in thermal inertia of buildings," *Energy Conversion and Management*, vol. 162, pp. 26–38, Apr. 2018, doi: 10.1016/j.enconman.2018.01.068.

[5]   C. Cheng, A. Blakers, M. Stocks, and B. Lu, "Pumped hydro energy storage and 100 % renewable electricity for East Asia," *Global Energy Interconnection*, vol. 2, no. 5, pp. 386–392, Oct. 2019, doi: 10.1016/j.gloei.2019.11.013.

[6]   Y. Gao, Z. Pan, J. Sun, Z. Liu, and J. Wang, "High-Energy Batteries: Beyond Lithium-Ion and Their Long Road to Commercialisation," *Nano-Micro Lett.*, vol. 14, no. 1, p. 94, Apr. 2022, doi: 10.1007/s40820-022-00844-2.

[7]   C. Schnuelle, J. Thoeming, T. Wassermann, P. Thier, A. von Gleich, and S. Goessling-Reisemann, "Socio-technical-economic assessment of power-to-X: Potentials and limitations for an integration into the German energy system," *Energy Research & Social Science*, vol. 51, pp. 187–197, May 2019, doi: 10.1016/j.erss.2019.01.017.

[8]   C. Panzone, R. Philippe, A. Chappaz, P. Fongarland, and A. Bengaouer, "Power-to-Liquid catalytic CO2 valorization into fuels and chemicals: focus on the Fischer-Tropsch route," *Journal of CO2 Utilization*, vol. 38, pp. 314–347, May 2020, doi: 10.1016/j.jcou.2020.02.009.

[9]   L. de S. N. S. Barbosa, D. Bogdanov, P. Vainikka, and C. Breyer, "Hydro, wind and solar power as a base for a 100% renewable energy supply for South and Central America," *PLOS ONE*, vol. 12, no. 3, p. e0173820, Mar. 2017, doi: 10.1371/journal.pone.0173820.

[10]   M. Thema, F. Bauer, and M. Sterner, "Power-to-Gas: Electrolysis and methanation status review," *Renewable and Sustainable Energy Reviews*, vol. 112, pp. 775–787, Sep. 2019, doi: 10.1016/j.rser.2019.06.030.

[11]   D. Hidalgo and J. M. Martín-Marroquín, "Power-to-methane, coupling CO2 capture with fuel production: An overview," *Renewable and Sustainable Energy Reviews*, vol. 132, p. 110057, Oct. 2020, doi: 10.1016/j.rser.2020.110057.

[12]   D. Parigi, E. Giglio, A. Soto, and M. Santarelli, "Power-to-fuels through carbon dioxide Re-Utilization and high-temperature electrolysis: A technical and economical comparison between synthetic methanol and methane," *Journal of Cleaner Production*, vol. 226, pp. 679–691, Jul. 2019, doi: 10.1016/j.jclepro.2019.04.087.

[13]   J. Ikäheimo, J. Kiviluoma, R. Weiss, and H. Holttinen, "Power-to-ammonia in future North European 100 % renewable power and heat system," *International Journal of Hydrogen Energy*, vol. 43, no. 36, pp. 17295–17308, Sep. 2018, doi: 10.1016/j.ijhydene.2018.06.121.

[14]   H. Mehrjerdi, H. Saboori, and S. Jadid, "Power-to-gas utilization in optimal sizing of hybrid power, water, and hydrogen microgrids with energy and gas storage," *Journal of Energy Storage*, vol. 45, p. 103745, Jan. 2022, doi: 10.1016/j.est.2021.103745.

[15]   A. V. Sepman, V. M. van Essen, A. V. Mokhov, and H. B. Levinsky, "The effects of hydrogen addition on Fenimore NO formation in low-pressure, fuel-rich-premixed, burner-stabilized CH4/O2/N2 flames," *International Journal of Hydrogen Energy*, vol. 33, no. 20, pp. 5850–5857, Oct. 2008, doi: 10.1016/j.ijhydene.2008.07.004.

[16]   A. Rao, Y. Liu, and F. Ma, "Study of NOx emission for hydrogen enriched compressed natural along with exhaust gas recirculation in spark ignition engine by Zeldovich' mechanism, support vector machine and regression correlation," *Fuel*, vol. 318, p. 123577, Jun. 2022, doi: 10.1016/j.fuel.2022.123577.

[17]   G. Mallouppas and E. A. Yfantis, "Decarbonization in Shipping Industry: A Review of Research, Technology Development, and Innovation Proposals," *Journal of Marine Science and Engineering*, vol. 9, no. 4, Art. no. 4, Apr. 2021, doi: 10.3390/jmse9040415.

[18]   L. E. Klebanoff, J. W. Pratt, and C. B. LaFleur, "Comparison of the safety-related physical and combustion properties of liquid hydrogen and liquid natural gas in the context of the SF-BREEZE high-speed fuel-cell ferry," *International Journal of Hydrogen Energy*, vol. 42, no. 1, pp. 757–774, Jan. 2017, doi: 10.1016/j.ijhydene.2016.11.024.

[19]   J. Serrano, F. J. Jiménez-Espadafor, and A. López, "Prediction of hydrogen-heavy fuel combustion process with water addition in an adapted low speed two stroke diesel engine: Performance improvement," *Applied Thermal Engineering*, vol. 195, p. 117250, Aug. 2021, doi: 10.1016/j.applthermaleng.2021.117250.

[20]   M. Ye, P. Sharp, N. Brandon, and A. Kucernak, "System-level comparison of ammonia, compressed and liquid hydrogen as fuels for polymer electrolyte fuel cell powered shipping," *International Journal of Hydrogen Energy*, vol. 47, no. 13, pp. 8565–8584, Feb. 2022, doi: 10.1016/j.ijhydene.2021.12.164.

[21]   S. Rönsch *et al.*, "Review on methanation – From fundamentals to current projects," *Fuel*, vol. 166, pp. 276–296, Feb. 2016, doi: 10.1016/j.fuel.2015.10.111.

[22]   R. Peters, M. Baltruweit, T. Grube, R. C. Samsun, and D. Stolten, "A techno economic analysis of the power to gas route," *Journal of CO2 Utilization*, vol. 34, pp. 616–634, Dec. 2019, doi: 10.1016/j.jcou.2019.07.009.

[23]   E. Moioli, N. Gallandat, and A. Züttel, "Model based determination of the optimal reactor concept for Sabatier reaction in small-scale applications over Ru/Al2O3," *Chemical Engineering Journal*, vol. 375, p. 121954, Nov. 2019, doi: 10.1016/j.cej.2019.121954.

[24]   F. Y. Al-Aboosi, M. M. El-Halwagi, M. Moore, and R. B. Nielsen, "Renewable ammonia as an alternative fuel for the shipping industry," *Current Opinion in Chemical Engineering*, vol. 31, p. 100670, Mar. 2021, doi: 10.1016/j.coche.2021.100670.

[25]   S. Drünert, U. Neuling, T. Zitscher, and M. Kaltschmitt, "Power-to-Liquid fuels for aviation – Processes, resources and supply potential under German conditions," *Applied Energy*, vol. 277, p. 115578, Nov. 2020, doi: 10.1016/j.apenergy.2020.115578.

[26]   V. Dieterich, A. Buttler, A. Hanel, H. Spliethoff, and S. Fendt, "Power-to-liquid via synthesis of methanol, DME or Fischer–Tropsch-fuels: a review," *Energy Environ. Sci.*, vol. 13, no. 10, pp. 3207–3252, Oct. 2020, doi: 10.1039/D0EE01187H.

[27]   C. I. Méndez, J. Ancheyta, and F. Trejo, "Modeling of Catalytic Fixed-Bed Reactors for Fuels Production by Fischer–Tropsch Synthesis," *Energy Fuels*, vol. 31, no. 12, pp. 13011–13042, Dec. 2017, doi: 10.1021/acs.energyfuels.7b01431.

[28]   J. R. G. Sánchez-López, A. Martínez-Hernández, and A. Hernández-Ramírez, "Modeling of transport phenomena in fixed-bed reactors for the Fischer-Tropsch reaction: a brief literature review," *Reviews in Chemical Engineering*, vol. 33, no. 2, pp. 109–142, Apr. 2017, doi: 10.1515/revce-2015-0044.

[29]   F. C. Barbosa, "Power to Liquid (PtL) Synthetic Aviation Fuel - A Sustainable Pathway for Jet Fuel Production," Feb. 2022, pp. 2021-36–0034. doi: 10.4271/2021-36-0034.

[30]   "Lurgi MegaMethanol™," *Air Liquide*, Feb. 25, 2016. https://www.engineering-airliquide.com/lurgi-megamethanol (accessed Jun. 17, 2022).

[31]   E. Moioli, R. Mutschler, and A. Züttel, "Renewable energy storage via CO2 and H2 conversion to methane and methanol: Assessment for small scale applications," *Renewable and Sustainable Energy Reviews*, vol. 107, pp. 497–506, Jun. 2019, doi: 10.1016/j.rser.2019.03.022.

[32]   J. Uebbing, L. K. Rihko-Struckmann, and K. Sundmacher, "Exergetic assessment of CO2 methanation processes for the chemical storage of renewable energies," *Applied Energy*, vol. 233–234, pp. 271–282, Jan. 2019, doi: 10.1016/j.apenergy.2018.10.014.

[33]   Wartsila, "World's first full scale ammonia engine test - an important step towards carbon free shipping," *Wartsila.com*, 2020. https://www.wartsila.com/media/news/30-06-2020-world-s-first-full-scale-ammonia-engine-test---an-important-step-towards-carbon-free-shipping-2737809 (accessed Sep. 16, 2021).

[34]   H. Zhang, L. Wang, J. Van herle, F. Maréchal, and U. Desideri, "Techno-economic comparison of green ammonia production processes," *Applied Energy*, vol. 259, p. 114135, Feb. 2020, doi: 10.1016/j.apenergy.2019.114135.

[35]   M. Götz *et al.*, "Renewable Power-to-Gas: A technological and economic review," *Renewable Energy*, vol. 85, pp. 1371–1390, Jan. 2016, doi: 10.1016/j.renene.2015.07.066.

[36]   G. Cau, V. Tola, F. Ferrara, A. Porcu, and A. Pettinau, "CO2-free coal-fired power generation by partial oxy-fuel and post-combustion CO2 capture: Techno-economic analysis," *Fuel*, vol. 214, pp. 423–435, Feb. 2018, doi: 10.1016/j.fuel.2017.10.023.

[37]   D. Devaraj, E. Syron, and P. Donnellan, "Synthetic Natural Gas Production: Production cost, key cost facto rs and optimal configuration," *Int. J. EQ*, vol. 5, no. 2, pp. 91–101, Jun. 2020, doi: 10.2495/EQ-V5-N2-91-101.

[38]   L. Kiewidt and J. Thöming, "Predicting optimal temperature profiles in single-stage fixed-bed reactors for CO2-methanation," *Chemical Engineering Science*, vol. 132, pp. 59–71, Aug. 2015, doi: 10.1016/j.ces.2015.03.068.

[39]   K. Ghaib and F.-Z. Ben-Fares, "Power-to-Methane: A state-of-the-art review," *Renewable and Sustainable Energy Reviews*, vol. 81, pp. 433–446, Jan. 2018, doi: 10.1016/j.rser.2017.08.004.

[40]   S. Matthischke, S. Roensch, and R. Güttel, "Start-up Time and Load Range for the Methanation of Carbon Dioxide in a Fixed-Bed Recycle Reactor," *Industrial and Engineering Chemistry Research*, vol. 57, no. 18, pp. 6391–6400, 2018, doi: 10.1021/acs.iecr.8b00755.

[41]   S. Theurich, S. Rönsch, and R. Güttel, "Transient Flow Rate Ramps for Methanation of Carbon Dioxide in an Adiabatic Fixed-Bed Recycle Reactor," *Energy Technology*, vol. 8, no. 3, p. 1901116, 2020, doi: 10.1002/ente.201901116.

[42]   X. Li, J. Li, B. Yang, and Y. Zhang, "Dynamic analysis on methanation reactor using a double-input–multi-output linearized model," *Chinese Journal of Chemical Engineering*, vol. 23, no. 2, pp. 389–397, Feb. 2015, doi: 10.1016/j.cjche.2014.11.007.

[43]   G. Tauer, C. Kern, and A. Jess, "Transient Effects during Dynamic Operation of a Wall-Cooled Fixed-Bed Reactor for CO2 Methanation," *Chemical Engineering & Technology*, vol. 42, no. 11, pp. 2401–2409, 2019, doi: 10.1002/ceat.201900367.

[44]   M. Gruber, D. Wiedmann, M. Haas, S. Harth, A. Loukou, and D. Trimis, "Insights into the catalytic CO2 methanation of a boiling water cooled fixed-bed reactor: Simulation-based analysis," *Chemical Engineering Journal*, vol. 406, p. 126788, Feb. 2021, doi: 10.1016/j.cej.2020.126788.

[45]   M. Martinez, C. Kern, and A. Jess, "Catalytic Hydrogenation of Carbon Dioxide to Methane in Wall-Cooled Fixed-Bed Reactors‡," *Chemical Engineering and Technology*, vol. 39, no. 12, pp. 2404–2415, 2016, doi: 10.1002/ceat.201500614.

[46]   V. Soto, C. Ulloa, and X. Garcia, "A CFD Design Approach for Industrial Size Tubular Reactors for SNG Production from Biogas (CO2 Methanation)," *Energies*, vol. 14, no. 19, Art. no. 19, Jan. 2021, doi: 10.3390/en14196175.

[47]   V. Soto, C. Ulloa, and X. Garcia, "A 3D Transient CFD Simulation of a Multi-Tubular Reactor for Power to Gas Applications," *Energies*, vol. 15, no. 9, Art. no. 9, Jan. 2022, doi: 10.3390/en15093383.

[48]   J. Lefebvre, S. Bajohr, and T. Kolb, "Modeling of the transient behavior of a slurry bubble column reactor for CO2 methanation, and comparison with a tube bundle reactor," *Renewable Energy*, vol. 151, pp. 118–136, May 2020, doi: 10.1016/j.renene.2019.11.008.

[49]   N. Engelbrecht, S. Chiuta, R. C. Everson, H. W. J. P. Neomagus, and D. G. Bessarabov, "Experimentation and CFD modelling of a microchannel reactor for carbon dioxide methanation," *Chemical Engineering Journal*, vol. 313, pp. 847–857, Apr. 2017, doi: 10.1016/j.cej.2016.10.131.

[50]   F. Kosaka *et al.*, "Effect of Ni content on CO2 methanation performance with tubular-structured Ni-YSZ catalysts and optimization of catalytic activity for temperature management in the reactor," *International Journal of Hydrogen Energy*, vol. 45, no. 23, pp. 12911–12920, Apr. 2020, doi: 10.1016/j.ijhydene.2020.02.221.

[51]   D. Schollenberger, S. Bajohr, M. Gruber, R. Reimert, and T. Kolb, "Scale-Up of Innovative Honeycomb Reactors for Power-to-Gas Applications – The Project Store&Go," *Chemie Ingenieur Technik*, vol. 90, no. 5, pp. 696–702, 2018, doi: 10.1002/cite.201700139.

[52]   H. T. Hwang, A. Harale, P. K. T. Liu, M. Sahimi, and T. T. Tsotsis, "A membrane-based reactive separation system for CO2 removal in a life support system," *Journal of Membrane Science*, vol. 315, no. 1, pp. 116–124, May 2008, doi: 10.1016/j.memsci.2008.02.018.

[53]   D. Schlereth and O. Hinrichsen, "A fixed-bed reactor modeling study on the methanation of CO2," *Chemical Engineering Research and Design*, vol. 92, no. 4, pp. 702–712, Apr. 2014, doi: 10.1016/j.cherd.2013.11.014.

[54]   S. Walspurger, G. D. Elzinga, J. W. Dijkstra, M. Sarić, and W. G. Haije, "Sorption enhanced methanation for substitute natural gas production: Experimental results and thermodynamic considerations," *Chemical Engineering Journal*, vol. 242, pp. 379–386, Apr. 2014, doi: 10.1016/j.cej.2013.12.045.

[55]   S. I. Ngo, Y.-I. Lim, D. Lee, K. S. Go, and M. W. Seo, "Flow behaviors, reaction kinetics, and optimal design of fixed- and fluidized-beds for CO2 methanation," *Fuel*, vol. 275, p. 117886, Sep. 2020, doi: 10.1016/j.fuel.2020.117886.

[56]   C. Jia, Y. Dai, Y. Yang, and J. W. Chew, "A fluidized-bed model for NiMgW-catalyzed CO2 methanation," *Particuology*, vol. 49, pp. 55–64, Apr. 2020, doi: 10.1016/j.partic.2019.05.004.

[57]   A. G. Dixon and B. Partopour, "Computational Fluid Dynamics for Fixed Bed Reactor Design," *Annu. Rev. Chem. Biomol. Eng.*, vol. 11, no. 1, pp. 109–130, Jun. 2020, doi: 10.1146/annurev-chembioeng-092319-075328.

[58]   H. K. Versteeg and W. Malalasekera, *An Introduction to Computational Fluid Dynamics THE FINITE VOLUME METHOD*, Second. Pearson Education, 2007.

[59]   D. Pashchenko, "Flow dynamic in a packed bed filled with Ni-Al2O3 porous catalyst: Experimental and numerical approach," *AIChE Journal*, vol. 65, no. 5, p. e16558, 2019, doi: 10.1002/aic.16558.

[60]   D. A. Nield and A. Bejan, *Convection in Porous Media*. Springer, 2017.

[61]   G. Chabot, R. Guilet, P. Cognet, and C. Gourdon, "A mathematical modeling of catalytic milli-fixed bed reactor for Fischer–Tropsch synthesis: Influence of tube diameter on Fischer Tropsch

selectivity and thermal behavior," *Chemical Engineering Science*, vol. 127, pp. 72–83, May 2015, doi: 10.1016/j.ces.2015.01.015.

[62]   C. I. Méndez, J. Ancheyta, and F. Trejo, "Modeling of Catalytic Fixed-Bed Reactors for Fuels Production by Fischer–Tropsch Synthesis," *Energy Fuels*, vol. 31, no. 12, pp. 13011–13042, Dec. 2017, doi: 10.1021/acs.energyfuels.7b01431.

[63]   E. A. Foumeny, H. A. Moallemi, C. Mcgreavy, and J. a. A. Castro, "Elucidation of mean voidage in packed beds," *The Canadian Journal of Chemical Engineering*, vol. 69, no. 4, pp. 1010–1015, 1991, doi: 10.1002/cjce.5450690425.

[64]   H. S. Fogler, *Elements of Chemical Reaction Engineering*. Prentice Hall PTR, 2006.

[65]   I. Ziółkowska and D. Ziółkowski, "Fluid flow inside packed beds," *Chemical Engineering and Processing: Process Intensification*, vol. 23, no. 3, pp. 137–164, Apr. 1988, doi: 10.1016/0255-2701(88)80012-6.

[66]   M. Baker, "CFD Simulation of Flow through Packed Beds using the Finite Volume Technique," Doctoral dissertation, University of Exeter, Cornwall TR10 9FE, UK, 2011. Accessed: Mar. 23, 2021. [Online]. Available: https://ore.exeter.ac.uk/repository/handle/10036/3396

[67]   N. Wakao, "Heat and mass transfer in packed beds, N. Wakao and S. Kaguei, Gordon and Breach Science Publishers, 1983,364 pages," *AIChE Journal*, vol. 29, no. 6, pp. 1055–1055, 1983, doi: https://doi.org/10.1002/aic.690290627.

[68]   W. Zhang, H. Machida, H. Takano, K. Izumiya, and K. Norinaga, "Computational fluid dynamics simulation of CO2 methanation in a shell-and-tube reactor with multi-region conjugate heat transfer," *Chemical Engineering Science*, vol. 211, p. 115276, Jan. 2020, doi: 10.1016/j.ces.2019.115276.

[69]   X. Gao, Y.-P. Zhu, and Z. Luo, "CFD modeling of gas flow in porous medium and catalytic coupling reaction from carbon monoxide to diethyl oxalate in fixed-bed reactors," *Chemical Engineering Science*, vol. 66, no. 23, pp. 6028–6038, Dec. 2011, doi: 10.1016/j.ces.2011.08.031.

[70]   A. Guardo, M. Coussirat, M. A. Larrayoz, F. Recasens, and E. Egusquiza, "Influence of the turbulence model in CFD modeling of wall-to-fluid heat transfer in packed beds," *Chemical Engineering Science*, vol. 60, no. 6, pp. 1733–1742, Mar. 2005, doi: 10.1016/j.ces.2004.10.034.

[71]   B. Jiang, L. Hao, L. Zhang, Y. Sun, and X. Xiao, "Numerical investigation of flow and heat transfer in a novel configuration multi-tubular fixed bed reactor for propylene to acrolein process," *Heat Mass Transfer*, vol. 51, no. 1, pp. 67–84, Jan. 2015, doi: 10.1007/s00231-014-1384-3.

[72]   ANSYS, Inc., *ANSYS Fluent User's Guide*, 15th ed. Canonsburg, PA 15317, U.S.: ANSYS, Inc., 2013.

[73]   R. Krishna and J. A. Wesselingh, "The Maxwell-Stefan approach to mass transfer," *Chemical Engineering Science*, vol. 52, no. 6, pp. 861–911, Mar. 1997, doi: 10.1016/S0009-2509(96)00458-7.

[74]   R. Taylor and R. Krishna, *Multicomponent Mass Transfer*. John Wiley & Sons, 1993.

[75]   P. P. J. M. Schram, "Chapman-Enskog Theory: Asymptotic Solution to the Boltzmann Equation; Transport Coefficients," in *Kinetic Theory of Gases and Plasmas*, P. P. J. M. Schram, Ed. Dordrecht: Springer Netherlands, 1991, pp. 92–132. doi: 10.1007/978-94-011-3612-9_5.

[76]   E. N. Fuller, P. D. Schettler, and J. Calvin. Giddings, "NEW METHOD FOR PREDICTION OF BINARY GAS-PHASE DIFFUSION COEFFICIENTS," *Ind. Eng. Chem.*, vol. 58, no. 5, pp. 18–27, May 1966, doi: 10.1021/ie50677a007.

[77]   D. F. Fairbanks and C. R. Wilke, "Diffusion Coefficients in Multicomponent Gas Mixtures," *Ind. Eng. Chem.*, vol. 42, no. 3, pp. 471–475, Mar. 1950, doi: 10.1021/ie50483a022.

[78]   J. Solsvik and H. A. Jakobsen, "A Survey of Multicomponent Mass Diffusion Flux Closures for Porous Pellets: Mass and Molar Forms," *Transp Porous Med*, vol. 93, no. 1, pp. 99–126, May 2012, doi: 10.1007/s11242-012-9946-7.

[79]   ANSYS, Inc., *ANSYS Fluent Theory Guide*, 15th ed. Canonsburg, PA 15317, U.S.: ANSYS, Inc., 2013.

[80]   J. M. P. Q. Delgado, "A critical review of dispersion in packed beds," *Heat Mass Transfer*, vol. 42, no. 4, pp. 279–310, Feb. 2006, doi: 10.1007/s00231-005-0019-0.

[81]   G. F. Froment and K. B. Bischoff, *Chemical reactor analysis and design*. Wiley, 1979.

[82]   V. Scharl, F. Fischer, S. Herrmann, S. Fendt, and H. Spliethoff, "Applying Reaction Kinetics to Pseudohomogeneous Methanation Modeling in Fixed-Bed Reactors," *Chemical Engineering & Technology*, vol. n/a, no. n/a, 2020, doi: 10.1002/ceat.201900535.

[83]   K. Huang, S. Lin, J. Wang, and Z. Luo, "Numerical evaluation on the intraparticle transfer in butylene oxidative dehydrogenation fixed-bed reactor over ferrite catalysts," *Journal of Industrial and Engineering Chemistry*, vol. 29, pp. 172–184, Sep. 2015, doi: 10.1016/j.jiec.2015.04.001.

[84]   N. R. Parlikkad *et al.*, "Modeling of fixed bed methanation reactor for syngas production: Operating window and performance characteristics," *Fuel*, vol. 107, pp. 254–260, May 2013, doi: 10.1016/j.fuel.2013.01.024.

[85]   G. D. Wehinger, "Radiation Matters in Fixed-Bed CFD Simulations," *Chemie Ingenieur Technik*, vol. 91, no. 5, pp. 583–591, 2019, doi: 10.1002/cite.201800179.

[86]   G. D. Wehinger and S. Flaischlen, "Computational Fluid Dynamics Modeling of Radiation in a Steam Methane Reforming Fixed-Bed Reactor," *Ind. Eng. Chem. Res.*, vol. 58, no. 31, pp. 14410–14423, Aug. 2019, doi: 10.1021/acs.iecr.9b01265.

[87]   TEMA, *Standards of the Tubular Exchanger Manufacturers Association*, 9th edition. Tarrytown, New York, United States of America: TEMA, 2007.

[88]   Y. You, S. Xiao, N. Pan, and Z. Deng, "Full Model Simulation of Shellside Thermal Augmentation of Small Heat Exchanger with Two Tube Passes," *Heat Transfer Engineering*, vol. 39, no. 12, pp. 1024–1035, Jul. 2018, doi: 10.1080/01457632.2017.1358484.

[89]   A. Mirvakili, A. Bakhtyari, and M. R. Rahimpour, "A CFD modeling to investigate the impact of flow mal-distribution on the performance of industrial methanol synthesis reactor," *Applied Thermal Engineering*, vol. 128, pp. 64–78, Jan. 2018, doi: 10.1016/j.applthermaleng.2017.08.145.

[90]   J. Moon, D. Q. Gbadago, and S. Hwang, "3-D Multi-Tubular Reactor Model Development for the Oxidative Dehydrogenation of Butene to 1,3-Butadiene," *ChemEngineering*, vol. 4, no. 3, Art. no. 3, Sep. 2020, doi: 10.3390/chemengineering4030046.

[91]   V. Yakhot and S. A. Orszag, "Renormalization group analysis of turbulence. I. Basic theory," *J Sci Comput*, vol. 1, no. 1, pp. 3–51, Mar. 1986, doi: 10.1007/BF01061452.

[92]   X. Zhang, D. Han, W. He, C. Yue, and W. Pu, "Numerical simulation on a novel shell-and-tube heat exchanger with screw cinquefoil orifice baffles," *Advances in Mechanical Engineering*, vol. 9, no. 8, p. 1687814017717665, Aug. 2017, doi: 10.1177/1687814017717665.

[93]   X. Wang, N. Zheng, Z. Liu, and W. Liu, "Numerical analysis and optimization study on shell-side performances of a shell and tube heat exchanger with staggered baffles," *International Journal of Heat and Mass Transfer*, vol. 124, pp. 247–259, Sep. 2018, doi: 10.1016/j.ijheatmasstransfer.2018.03.081.

[94]   A. El Maakoul *et al.*, "Numerical comparison of shell-side performance for shell and tube heat exchangers with trefoil-hole, helical and segmental baffles," *Applied Thermal Engineering*, vol. 109, pp. 175–185, Oct. 2016, doi: 10.1016/j.applthermaleng.2016.08.067.

[95]   N. Li *et al.*, "Analysing thermal-hydraulic performance and energy efficiency of shell-and-tube heat exchangers with longitudinal flow based on experiment and numerical simulation," *Energy*, vol. 202, p. 117757, Jul. 2020, doi: 10.1016/j.energy.2020.117757.

[96]   Y. Yan, Z. Ni, X. Zhi, and J. Yin, "Numerical study on thermal performance of a BOG heat exchanger in the inclined condition," *Journal of Natural Gas Science and Engineering*, vol. 34, pp. 616–626, Aug. 2016, doi: 10.1016/j.jngse.2016.07.040.

[97]   N. Zheng, W. Liu, Z. Liu, P. Liu, and F. Shan, "A numerical study on heat transfer enhancement and the flow structure in a heat exchanger tube with discrete double inclined ribs," *Applied Thermal Engineering*, vol. 90, pp. 232–241, Nov. 2015, doi: 10.1016/j.applthermaleng.2015.07.009.

III.   Hypothesis

Considering the abovementioned background, and the reviewed literature, the following hypothesis is proposed to conduct the research work:

"A 3D CFD design methodology capable of assessing the impacts of relevant Power to Gas operational features of a tubular fixed bed reactor stands out as an essential tool for designing industrial-sized CO2 methanation plants for intermittent renewable energy storage."

IV. Results

This section comprises two articles encompassing the main results of this thesis. Article I *"A CFD Design Approach for Industrial Size Tubular Reactors for SNG Production from Biogas (CO₂ Methanation)"* addresses the first two specific objectives stated in section I.6, namely the design of the reactor and its performance analysis under steady state with a focus on coolant flow efficiency. Article II *"A 3D Transient CFD Simulation of a Multi-Tubular Reactor for Power to Gas Applications"*, studies the effects of dynamic disruptions pertinent to a Power to Gas context on the reactor's performance with a focus on temperature control and minimum methane content. Given a biogas / hydrogen inlet composition, the methodology iterates until a satisfactory design is proposed in terms of CH_4 quality and thermal safety (hot-spot control). Inlet gas composition, pressure and temperature are considered the main variables to characterize the chemical reaction. The rest of the variables are geometrical in nature and associated to toe required reactor volume (number and length of tubes) and heat transfer enhancement features (e.g., shell and tube baffle arrangement and tubes diameter).

The proposed methodology is unique and novel in terms of the integration of all the relevant transport phenomena in a single model allowing for the production of a fully representative 3D basic design which may be further upgraded to a true "Virtual Twin" reactor depicted in flow chart below:
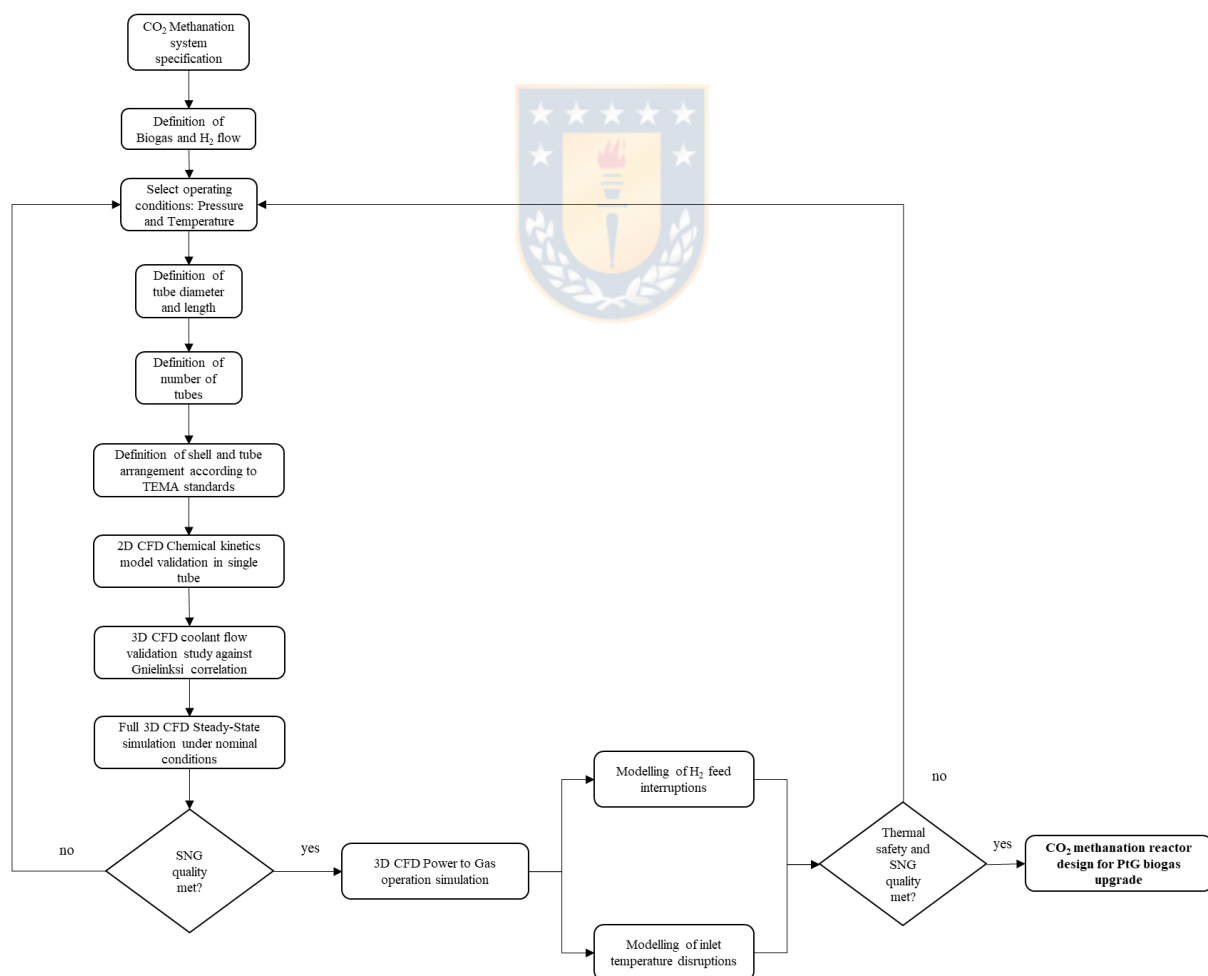
IV.1 A CFD Design Approach for Industrial Size Tubular Reactors for SNG Production from Biogas (CO$_2$ Methanation)

Victor Soto [1],*, Claudia Ulloa [2] and Ximena Garcia [1]

[1] Carbon and Catalysis Laboratory (CarboCat), Department of Chemical Engineering, Faculty of Engineering, Universidad de Concepción, P.O. Box 160-C, Concepción, Chile; xgarcia@udec.cl

[2] Environmental Engineering Department, Faculty of Environmental Sciences and EULA Chile Centre, Universidad de Concepción, P.O. Box 160-C, Concepción, Chile; claudiaulloa@udec.cl

* Correspondence: vsotop@udec.cl

Abstract: A tubular reactor based on the disk and doughnut concept was designed as an engineering solution for biogas upgrading via CO$_2$ methanation. CFD (Computational Fluid Dynamics) benchmarks agreed well with experimental and empirical (correlation) data, giving a maximum error of 8.5% and 20% for the chemical reaction and heat transfer models, respectively. Likewise, hot spot position was accurately predicted, with a 5% error. The methodology was used to investigate the effect of two commercially available coolants (thermal oil and molten salts) on overall reactor performance through a parametric study involving four coolant flow rates. Although molten salts did show higher heat transfer coefficients at lower coolant rates, 82% superior, it also increases, by five times, the pumping power. A critical coolant flow rate (3.5 m^3/h) was found, which allows both a stable thermal operation and optimum pumping energy consumption. The adopted coolant flow range remains critical to guarantee thermal design validity in correlation-based studies. Due to the disk and doughnut configuration, coolant flow remains uniform, promoting turbulence (Re ≈ 14,000 at doughnut outlet) and maximizing heat transfer at hot spot. Likewise, baffle positioning was found critical to accommodate and reduce stagnant zones, improving the heat transfer. Finally, a reactor design is presented for SNG (Synthetic Natural Gas) production from a 150 Nm^3 h^{-1} biogas plant.

Keywords: CO$_2$ methanation; CFD; multi-tubular reactor

1. Introduction

The world is currently experiencing an energy revolution without precedents, motivated by social, environmental, and economic drivers. Still, an ambitious target of a 100% renewable energy supply will never be attainable due to the transient nature of wind and solar energy [1]. As an alternative, Power-to-Methane (PtM) stands out as a promising option to absorb and exploit surplus renewable energy in the form of "synthetic natural gas" (SNG). The possibility of using the existing natural gas infrastructure to store and transport the SNG to the end-user confers a critical advantage over other concepts. PtM systems consist of: (1) a H$_2$ source (water electrolyser), (2) CO$_2$ source, and (3) methanation reactor [2]. H$_2$ and CO$_2$, are converted in a methanation reactor into a gas mixture of CH$_4$ and H$_2$O through the Sabatier reaction (Equation (1)).

$$CO_2 + 4H_2 \leftrightarrow CH_4 + 2H_2O \ \Delta H_r^0 = -165.0 \frac{kJ}{mol} \tag{1}$$
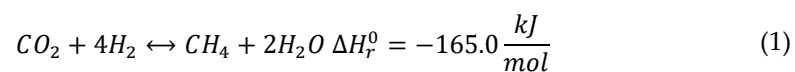
Potential sources for CO$_2$ are diverse: cement, iron and steel industries, flue gas from fossil-fuelled power plants, atmospheric air or biogas [3]. However, the abovementioned CO$_2$ sources, with the exception of biogas, require an additional carbon capture/upgrading step, which furthers reduces the energy efficiency and increases the costs significantly [4].

1.1. Current Trends in Fixed Bed Reactor Design

Since CO$_2$ methanation is the core step in PtM, this topic has been the focus of extensive research with a particular interest in reactor design and optimization [5]. In methanation processes, multi-tubular (fixed bed) reactors appear as the standard concept for their simple design and straightforward

manufacturing. Because of the high exothermicity of the Sabatier reaction, the shell and tube configuration appears as a practical and effective engineering solution for temperature control [6]. As depicted in Table 1, tubular reactors remain the focus of the most recent research works. The conventional design methodology for multi-tubular fixed bed reactors assumes that a single tube may be considered an appropriate representation of the whole system. Heat transfer is calculated assuming a constant heat transfer coefficient or a fixed temperature at wall boundaries [5-8]. Consequently, both coolant flow and temperature distributions along the shell-side are neglected. This approach leads to the assumption that all tubes are exposed to the same cooling conditions. From an operational point of view, this can only occur if the coolant flow is parallel and completely uniform to the reactor bundle. In addition, energy efficiency demands coolant flow minimization to reduce pumping energy consumption. Sun and Simakov [9] asserted that mineral oils are unsuitable for tubular reactor cooling systems due to their incapacity to handle high-temperature flows, hence molten salts are recommended. Indeed, most methanation studies consider this approach, incorporating molten salts as cooling systems [10]. Along with the problem mentioned above, most single tube models impose high external heat transfer coefficients [9-12]. Remarkably, no technical basis is given to that choice; neither is the nature of the cooling systems declared. Such high external heat transfer coefficients may only be found in boiling cooling systems, not conventional systems based on molten salts or thermal oil [13].

1.2. Research Scope and Contribution

To the best of our knowledge, no multi-tubular methanation reactor involving coolant side flow has been modelled in detail so far. Even in the field of reactor modelling, works of this kind are scarce. The work of Hukkanen et al. [14] is notable for being one of the first simulations which considers CFD modelling of the coolant flow. They correctly conclude that isothermal shell-side coolant behaviour was not observed, and distinctive coolant zones were identified through the reactor length. Nevertheless, individual tubes were not really included in the reactor. Instead, reaction heat was simulated through a simplified methodology [15]. Since the physical presence of tubes is neglected, it was not possible to model a realistic shell flow. Wu et al. [16], using a segmental baffled shell and tube reactor, proposed a correlation-based approach to evaluate the performance of the considered design. Correctly, this author highlights the importance of understanding the flow phenomenon inside the shell to assess the causes of weaknesses in the cooling system. However, there is no information regarding the performance of the reactor in terms of yield, conversion or selectivity of desirable products. Satisfactory heat transfer and flow features must be reflected in terms of reactor performance parameters. Jiang et al. [17] developed a CFD simulation of a multi-tubular reactor based on the disk and doughnut concept for the propylene to acrolein process. Remarkably, a whole bundle reactor comprising 790 tubes was modelled, and the actual effects of baffles and tubes on coolant flow were analysed. Although the superior performance of the disk and doughnut concept over the segmented baffle was probed, chemical reactions were not included. Instead, its effects were replaced through polynomial temperature distributions at reactive tube walls. Moon et al. [18] developed a CFD model of a multi-tubular reactor for oxidative dehydrogenation of butene to 1,3-butadiene, based on the standard segmented baffle design. Unlike Jiang [17], detailed Langmuir-Hinshelwood-Hougen-Watson (LHHW) kinetics was considered, but coolant flow, although included, was not studied. Thus, the necessity to account for the cooling jacket and the cooling medium, in order to get closer to real industrial-scale, remains a relevant topic in fixed bed reactor modelling, as highlighted by several authors [4,7].

One of the most critical problems in CO_2 methanation is the presence of a hot spot and the subsequent thermal runaway in reactor scale-up design and operation. A proper design of the cooling system is therefore of great significance. Furthermore, to understand the causes of weaknesses in the cooling system, the flow pattern inside the shell should also be considered. Therefore, a realistic approach is mandatory to study the key aspects that affect coolant performance and hot spot control. The traditional "single-tube" approach makes it possible to predict the general patterns of reactors' behaviour and performance; however, a full CFD model can also visualise the coolant flow and temperature fields in detail under industrially relevant conditions. In this research, a novel modelling approach of multi-physics simulation of chemical reaction, fluid flow and heat transfer based on ANSYS Fluent is

proposed for multi-tubular fixed bed methanation reactors. Relevant transport phenomena (turbulence, heat transfer and complex chemical kinetics) for both reactive and coolant flow are covered through a cost-effective computational method. From a methodological point of view, this study may be seen as a contribution to the work of Jiang et al. [17], adding a realistic interaction between coolant flow and an actual chemical reaction heat source. Consequently, coolant flow optimisation should be considered an essential step in reactor design, effectively improving the temperature uniformity and heat removal in reactive tubes. The focus of this study is the design of a tubular reactor, its cooling system and the subsequent performance evaluation. A design case study is developed, based on the "disk and doughnut" configuration, addressing the current needs of methanation technology: small units for decentralised plants based on biogas and an optimal coolant system for stable and energetic efficient operation.

Table 1. Summary of published fixed bed methanation models.

Modelling Approach	Reactor Type	Dim.	Code	Ref.
Pseudo-homogeneous models based on intrinsic kinetics	Tubular	2D	COMSOL	[19]
	Tubular	2D	Presto-Kinetics	[11]
	Tubular	2D	COMSOL	[20]
	Tubular	2D&3D	Fluent	[8]
	Tubular	1D	Matlab & Athena	[21]
	Metallic-Honeycomb	2D	COMSOL	[22]
	Tubular	1D	FlexPDE	[23]
	Tubular	1D	N/A	[24]
	Tubular-Structured	2D	COMSOL	[25]
	Tubular	2D	OpenFoam	[26]
	Tubular	1D	Fortran 90	[27]
	Tubular	1D	AMPL& IPOPT	[28]
Pseudo-homogeneous models with effectiveness factor	Tubular	1D	Python	[29]
	Tubular	1D	Matlab	[9]
	Tubular	1D	CONOPT	[30]
	Tubular	2D	Matlab	[7]
	Structured-wall	1D&3D	COMSOL 1D, Fluent 3D	[31]
	Tubular	1D	Fortran 90	[6]
	Tubular	1D	Matlab	[32]
	Tubular	1D	Matlab	[12]
	Tubular	1D	Matlab	[33]
	Tubular	1D	Matlab	[10]
	Tubular	1D	Matlab	[34]
	Tubular	3D	Fluent	[35]
	Tubular	1D	Matlab	[36]
	Tubular	0D, 2D, 3D	COMSOL	[37]
Heterogeneous models with intraparticle mass balance	Tubular, Structured	1D&2D	Matlab (1D) COMSOL (2D)	[38]
	Catalytic wall reactor	1D&2D	COMSOL	[39]
	Micro channel	3D	COMSOL	[40]
	Tubular-annular	1D&2D	COMSOL	[41]
	Micro-structured	1D	gPROMS ModelBuilder	[42]
	Tubular	2D	Fortran 90	[43]
	Tubular	2D	Fortran 90	[44]
	Tubular, Fluidized bed	1D	Matlab	[45]
	Tubular	1D	Matlab	[46]
	Tubular, low d_t/d_P	3D (PRCFD-DEM)	COMSOL	[47]

2. Reactor Model

2.1. Reactor Description

The proposed design must suit the special technical constraints of a cooperative 150 Nm^3 h^{-1} biogas plant [48]. It was deducted that the reactor must be a compact modular unit of simple maintenance and operation. In addition, shell-side design demands an even heat transfer effect among tubes. Hence, a disk-doughnut configuration was adopted for such considerations. This concept makes extensive use of radial flow (crossflow) across tubes, maximizing heat transfer rates in the reactor [49]. The uniform flow rate distribution into the shell-side through the disk-doughnut configuration is the premise to ensure uniform cooling and better reactor performance. In addition, radial design minimizes both shell-side pressure drop and baffle-shell leakage [50]. Modular reactor dimensions are deducted from TEMA [51] standards and the Heat Exchanger Design Handbook [49]. A modular length of 1 m was selected to allow easy handling of the equipment and further plant scaling as needed. An inner tube diameter of 25 mm has been set to fulfil the recommended ratio of reactor internal diameter to catalyst particle >10 for a 2.5 mm spherical particle, thus reducing wall effects. Based on Jiang et al. [17] results, a co-current cooling system was selected as it shows better effectiveness in hot spot control than counter-current. According to these requirements and constraints, a disk-doughnut reactor concept is presented in Figure 1.
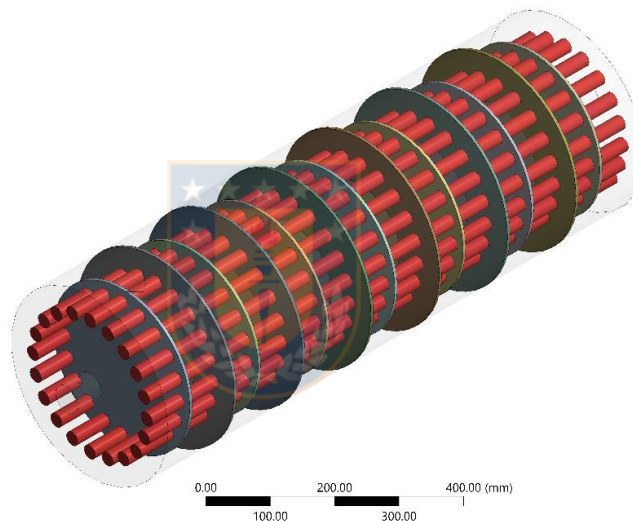
Figure 1. Proposed 1 m reactor module for biogas methanation (case study).

Since CO_2 methanation is an equilibrium reaction, high conversion rates (≈100%) may be extremely difficult to achieve. The final configuration (length and/or number of modules) will be determined in function of desired product composition. A restrictive target quality of $CH_4 \geq 95\%$, $H_2 \leq 5\%$ and $CO_2 \leq 2.5\%$ has been adopted, as suggested by Guilera et al. [52]. An operational temperature of 523.15 K was selected to reach a good compromise between kinetic restrictions and hot spots formation, with a maximum operational temperature of 650 K, which corresponds to catalyst admissible operating temperature [32]. Operational pressure is one of the most important parameters to define. It significantly influences investment and operational costs and reactor performance, favouring reaction kinetics and shifting the reaction equilibrium towards products. In addition, it has been reported that higher pressures prevent carbon formation. At 11 bar, carbon begins to appear just above 788 K for nickel-based catalysts [11]. Jürgensen et al. [53] reports that, for biogas-based carbon sources, methane may hinder carbon conversion greatly at pressures ≈ 1 bar. This effect can be easily compensated at pressures above 8 bar, while at 10 bar, the impact of methane content is nearly zero. Therefore, an operational pressure of 10 bar was chosen for its multiple benefits in terms of reactor performance and the availability of industrial equipment that may fulfil the technical requirements of hydrogen or biogas compression. CO formation was neglected as supposed by related works [9,24]. A non-stochiometric H_2/CO_2 ratio of 3.8 has been selected in order to easily meet product gas quality requirements following

the experience of Jürgensen et al. [53]. Shell and tube characteristics and operating conditions are summarized in Table 2.

Table 2. Design and operational parameters for simulated multi-tubular fixed-bed reactor. Biogas composition from [53].

Parameter	Unit	Value
Shell and tube dimensions		
Shell inside diameter	mm	345
Tube outside diameter	mm	25
Tube length	mm	975
Number of tubes	-	20
Tube pitch	mm	40
Number of baffles	-	13
Baffle spacing	mm	70
Operational parameters		
Reaction pressure	bar	10
Inlet temperature	K	523
Cooling temperature	K	523
GHSV	h^{-1}	3200
Limit op. temperature	K	923
Gas flow per tube	Nm^3/hr	1.5
Feed gas composition		
CH_4 inlet mole fraction	mol/mol	0.28
CO_2 inlet mole fraction	mol/mol	0.146
H_2 inlet mole fraction	mol/mol	0.55
H_2O inlet mole fraction	mol/mol	0.015
O_2 inlet mole fraction	mol/mol	0.004

2.2. Model Setup

In this work, CO_2 hydrogenation over a commercial nickel catalyst in a 3D multi-tubular shell and tube type reactor was investigated through CFD simulations. To accurately validate the adequacy of the CFD model (conservation equations and kinetic model [54]), experimental results from Gruber et al. [37] were used for comparison. In addition, due to the high relevance of the coolant flow in methanation reactors, simulation results were used to calculate shell-side heat transfer coefficients at tube walls. CFD results were further compared against the Gnielinski correlation [55] to check the validity of the shell-side heat transfer coefficients. Validation simulation was split into two benchmark problems and sub-domains, each of which concentrates on a particular phenomenon: (i) Chemical Kinetics (tube side) to verify validity of the model selected for the reaction kinetics, and (ii) Heat transfer-flow dynamics (shell side) to validate the calculated heat transfer coefficients. Once the heat transfer and kinetic model were satisfactorily validated, both simulations were merged into a whole model that accurately represented mass and energy transport. Thus, to save computation time while focusing on the relevant phenomena (heat transfer and chemical reactions), the simulation was divided into four steps which are described below.

Step 1: Benchmark simulation for single tube: A single tube model was first developed to check and validate the LHHW kinetic model as adopted in Fluent via a User Defined Function (UDF). As only chemical reactions were of interest at this stage, a 2D simplified model was adopted. This Single Tube model was validated against experimental data reported by Gruber et al. [56]. Since heat transfer is the focus of this research, the experimental temperature profile was chosen as a reference variable for kinetic validation purposes at single tube level. Model geometry and simulation conditions were implemented to reflect both real experimental reactor geometry and conditions.

Step 2: Benchmark simulation for shell-side: A non-reactive tube bundle was fully modelled to represent best the heat transfer interface between reactive tubes and coolant. This means that all

structures that alter the flow were present (baffles, tube bundle, shell walls, coolant inlet and outlet). Since the focus was on heat transfer between individual tube walls and coolant, no chemical reactions were considered. Instead, as Jiang et al. [17] proposed, constant wall temperature distribution was incorporated as a boundary condition, emulating the presence of chemical reactions. Surface heat transfer coefficients at tube walls were then validated against Gnielinski [55] correlation for tube bundles.

Step 3: Mesh independency: After validation of both phenomena (chemical kinetics and heat transfer), these were merged into a full model, and mesh independency was assessed for four mesh sizes. Boundary conditions considered for the mesh independency test reflect nominal operation of the proposed design, as declared in Table 2.

Step 4: Study Case: A modular multi-tubular reactor was designed to fulfil the operational requirements of a small biogas plant. As already stated, it is in the best interest of an efficient reactor to reach the desired conversion under safe and stable thermal conditions while pumping work is minimized. The influence of coolant flow and type regarding pumping energy consumption and hot spot temperature control were analysed. Furthermore, the benefits of the disk-doughnut configuration were discussed from a thermal and hydrodynamic perspective. Finally, the number of required modules and final reactor configuration were determined to fulfil the needed SNG quality and biogas production.

2.3. Governing Equations

Governing equations (Table 3) reflect the physical models that represent transport phenomena inside reactive tubes and shell-side flow. A porous media model (PMM) was adopted to represent the reactive tubes as a good compromise between accuracy and computational resources [57]. Interaction between phases is included through source terms that account for momentum, energy and mass transfer. Momentum balance between phases is modelled using a momentum exchange term, Equation (4), derived from the Ergun equation [58]. A mean porosity value was adopted in momentum (Equation (3)) and energy (Equation (5)) governing equations to account for the presence of voids in the continuum. Since all species concentrations are of the same order of magnitude, a multi-component diffusion model [58] was adopted to account for the diffusive mass flux, (Equation (8)). Radial dispersion effects were neglected as plug-flow conditions were assumed, that is, the ratio of catalytic bed length to catalyst particle (L_{bed}/d_P) > 150 and internal reactor to particle diameter, d_t/d_P > 10 [59]. An equilibrium model is adopted to represent the energy equation (Equation (5)) based on an effective thermal conductivity computed as the volume average of fluid and solid conductivity (Equation (6)). Since (d_t/d_P > 10), wall effects were discarded [59]. Radiation heat transfer remains negligible since operational temperatures do not surpass 400 °C [60]. Regarding mass transport limitation, a constant activity factor A_f was incorporated to the species source term in Equation (7) following the experience of Matthischke et al. [12]. Chemical reactions were incorporated into Fluent as User Defined Functions (UDF) in C language [61]. Turbulence in the shell-side was modelled using the realizable k-ε turbulence model known to accurately represent flows involving curved geometries and swirling flows [62]. Gas flow in the porous medium exhibited a low Reynolds number (143, according to Equation (10)), which corresponds to a transition flow regime [63]. According to Jiang et al. [17] and Zhang et al. [26] turbulence effects in the transition regime are not very strong. Therefore, a laminar model was adopted in reactive tubes. Rigorous reaction kinetics based on the experimental work of Koschany et al. [54] with parameters of Matthischke et al. [12] were considered. Among current CO_2 hydrogenation kinetics, the model of Koschany et al. [54] remains remarkably useful in engineering applications since it was derived for a state-of-the-art catalyst and considering industrial operational conditions. Moreover, derived kinetics expressions cover a wide range of relevant operational conditions from the differential regime to the thermodynamic equilibrium [54]. For a detailed description of the kinetics adopted the reader is directed to Appendixes A and B.

Table 3. Governing and constitutive equations used in this CFD model.

Reactive flow (tubes)

Gas phase continuity: $\nabla \cdot (\varphi \rho_g \vec{v}) = 0$ (2)

Gas phase momentum: $\nabla \cdot (\varphi \rho_g \vec{v} \, \vec{v}) = -\varphi \nabla p + \nabla \cdot (\varphi \bar{\bar{\tau}}) - \vec{S}$ (3)

Gas-solid momentum exchange: $\vec{S} = \left(\frac{\mu_\varphi}{\kappa}\vec{v} + C_2 \frac{1}{2}\rho|\vec{v}|\vec{v}\right)$ (4)

Gas phase Energy: $\nabla \cdot \left(\vec{v}\left(\rho_g E_g + p\right)\right) = \nabla \cdot (\varphi \lambda_\varphi \nabla T_g - \sum_i h_i j_i) + S_{h,rxn}$ (5)

$\lambda_\varphi = \varphi \lambda_g + (1-\varphi)\lambda_s$ (6)

Species: $\nabla \cdot (\rho_g \vec{v} \, Y_i) = -\nabla \cdot \vec{J_i} + A_f \cdot R_i$ (7),

Diffusive mass flux: $\vec{J_i} = \sum_{j=1}^{N-1} \rho_g D_{ij} \nabla Y_i$ (8),

Gas phase equation of state: $\rho_g = RT_g$ (9)

Reynolds number based on the particle diameter:

$$Re_{dp} = \frac{\rho_g U d_p}{\mu_g(1-\varphi)} \quad (10)$$

Coolant flow (shell-side):

Fluid phase continuity: $\nabla \cdot (\rho_f \vec{v}) = 0$ (11)

Fluid phase momentum: $\nabla \cdot (\rho_f \vec{v} \, \vec{v}) = -\nabla p + \nabla \cdot (\bar{\bar{\tau}})$ (12)

Fluid phase energy: $\nabla \cdot \left(\vec{v}\left(\rho_f E_f + p\right)\right) = \nabla \cdot (\lambda_{eff} \nabla T)$ (13)

$\lambda_{eff} = (\lambda + \lambda_t)$ (14)

Baffles & tube walls:

Solid phase energy: $\nabla \cdot (\lambda_{st} \nabla T) = 0$ (15)

2.4. Numerical Methods

Pressure and velocity coupling was achieved through the SIMPLE algorithm. Second-order upwind discretization schemes were selected for momentum, energy and species equations, and a standard scheme for pressure. Variable gradients were discretised through the least-squares cell-based method. Under-relaxation factors for momentum and mass balances were set at 0.6. For the energy equation, the selected value was 0.4. Convergence was checked as the consecutive decrease in residuals by at least three orders of magnitude, 10^{-6} and 10^{-5} for the continuity, energy and mass balance, respectively. For simulations involving coolant flow, wall y+ was monitored and evaluated to guarantee standard wall functions requirements (y+ > 30) and heat transfer coefficient on tube walls. Additionally, CO_2 molar concentration at the tube's outlet was checked for full model simulations. All steady-state governing equations, Table 3, were discretised and solved by the finite volume method using the commercially available CFD code ANSYS Fluent 19.

3. Results and Discussion

3.1. Benchmark Simulation for Single Tube

In order to verify the applicability of the adopted kinetics model [54], a 2D axisymmetric single tube model was implemented considering the geometry and operational conditions from Gruber et al. [56] (20 kW, 10 bar case): reactor inner diameter and length 30 mm and 1000 mm, respectively, operational pressure of 10 bar, reactants and coolant temperature of 523 K, gas hourly space velocity ($GHSV_n$) of 2250 h^{-1} and H_2/CO_2 ratio of 4. A convection boundary condition was adopted at tube walls. Heat transfer coefficient was taken from [32], based on nucleate boiling water. A comparative plot between the experimental run and the CFD simulation for the individual tube is shown in Figure 2. There is a good match between results using the adopted kinetic model and the experimental temperature profile. The maximum discrepancy between simulation and experimental data is 20% at the tube inlet and 5% at the hot spot. This can partly be attributed to the lack of information regarding thermophysical catalyst properties (thermal conductivity and heat capacity) and to the adopted dilution profile. Simulation results also showed a similar trend with the experimental data (Figure 2). Gas temperature increases quickly until it reaches the hot spot at 80 mm from the inlet. Then, temperature steadily decreases, resulting in an outlet temperature of ≈523.15 K, which is coincident with the coolant temperature. The temperature at the hot spot was overestimated by 5% (860 K), but its position matches

the experiment. It is concluded that an activity factor of 0.1 fits well the intrinsic kinetics to experimental data, and therefore it was adopted in subsequent simulations.
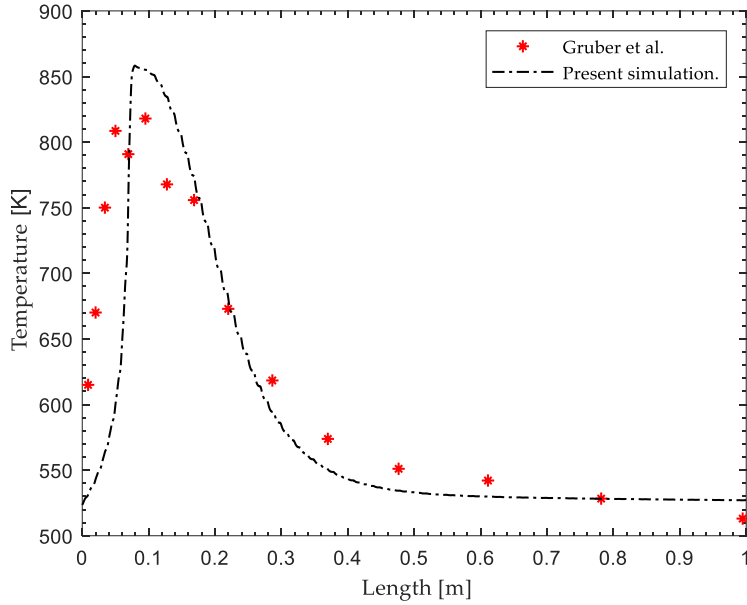
Figure 2. Axial Temperature profile comparison between Experimental data and current 2D validation model.

3.2. Benchmark Simulation for Shell-Side ★ ★ ★ ★ ★

Research and correlations that may suit disk-and-doughnut multi-tubular reactors are scarce and may not be adequate for systems with a small number of tubes. A proper alternative should represent the heat transfer from coolant bulk flow to reactor walls as accurately as possible. Due to the intrinsic symmetry of the flow in a disk-doughnut configuration, it is possible to assume that each tube section between two consecutive baffles behaves like a single row of tubes in crossflow. The Gnielinski [55] correlation for a single row of tubes stands out as the best model resembling this flow conditions, and therefore, was adopted for heat transfer CFD results verification. The Nusselt number for a row of tubes was calculated according to Equation (22), considering a laminar and a turbulent contribution. The associated Reynolds number was calculated from Equation (16), where l corresponds to the "streaming length" (the length of the flow path traversed over a single tube), the void fraction, ψ, which in turn depends on the transverse pitch ratio in the row, was obtained from Equation (18). Calculation of U_w, is based on the mass conservation principle and the effective crossflow area, as specified by Slipcevic [49]. The heat transfer coefficient was evaluated through Equation (23), while numerical heat transfer performance was evaluated through Equation (24) by ANSYS CFD Post after the temperature field had been obtained.

$$Re_{\psi,l} = \frac{U_w l}{\psi \nu} \tag{16}$$

$$10 < Re_{\psi,l} < 10^6 \qquad Pr = \frac{\nu}{\alpha} \tag{17}$$

$$0.6 < Pr < 10^3 \quad \psi = 1 - \frac{\pi}{4(t_p/d_t)} \tag{18}$$

$$l = \left(\frac{\pi}{2}\right) d_t \tag{19}$$

$$Nu_{l,lam} = 0.664 + \sqrt{Re_{\psi,l}} \ \sqrt[3]{Pr} \tag{20}$$

$$Nu_{l,tur} = \frac{0.037 Re_{\psi,l}^{0.8} Pr}{1 + 2.443 Re_{\psi,l}^{-0.1} \left(Pr^{\frac{2}{3}} - 1 \right)} \tag{21}$$

$$Nu_{0,row} = 0.3 + \sqrt{Nu_{l,lam}^2 + Nu_{l,turb}^2} \tag{22}$$

$$h_{row} = \frac{Nu_{0,row} \lambda_f}{l} \tag{23}$$

$$h_{num} = \frac{Q_w}{A(T_w - T_{bulk})} \tag{24}$$

$$P_h = \frac{q \rho g h_w}{3.6^6} \tag{25}$$

T_{bulk} is the flow weighted average temperature of the coolant fluid and T_w the surface temperature near the external wall side Q_w is the heat flux across tube walls and A the tube wall surface area. Six test problems were performed for shell-side flow in the range of 1.7–4.6 kg/s. In Figure 3 the selected arrangement (mesh model and boundary conditions) is presented. Boundary conditions for shell-side test problems summarize as follows: Mass flow rate in kg/s at 473.15 K in coolant inlet (I), constant temperature at tube walls of 495 K (II) and adiabatic external walls (III). Thermally coupled interface boundary conditions were adopted when fluid (IV) and solid (V) cell zones (baffles) match. Operational pressure was set at 1 bar. The coolant chosen was thermal oil. Figure 4 gives the comparisons between correlation data and the shell-side simulation data. It reveals a good agreement between Gnielinski correlation and the CFD results. A maximum error of 10% between numerical and correlation values (at 4.5 kg/s) was obtained, which is acceptable for engineering applications. As a result, it can be concluded that the developed numerical approach was accurate enough to calculate tube to coolant heat transfer coefficients and thus effectively applicable to investigate the effect of the coolant flow on reactor performance in the considered range. For lower coolant flows, there was not a good agreement between Gnielinski correlation and CFD results. This becomes especially relevant for single tube simulations, in which the external heat transfer coefficient is calculated from correlations such as Fache [6]. In those situations, the range of validity of such correlations must be clearly stated.
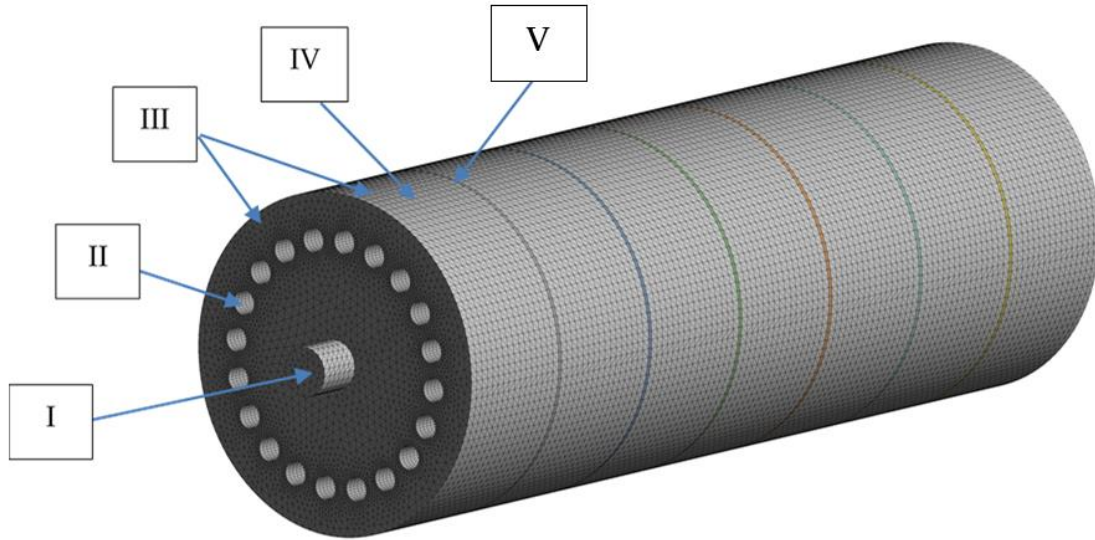
Figure 3. Mesh model and boundary conditions for shell-side flow test problems.
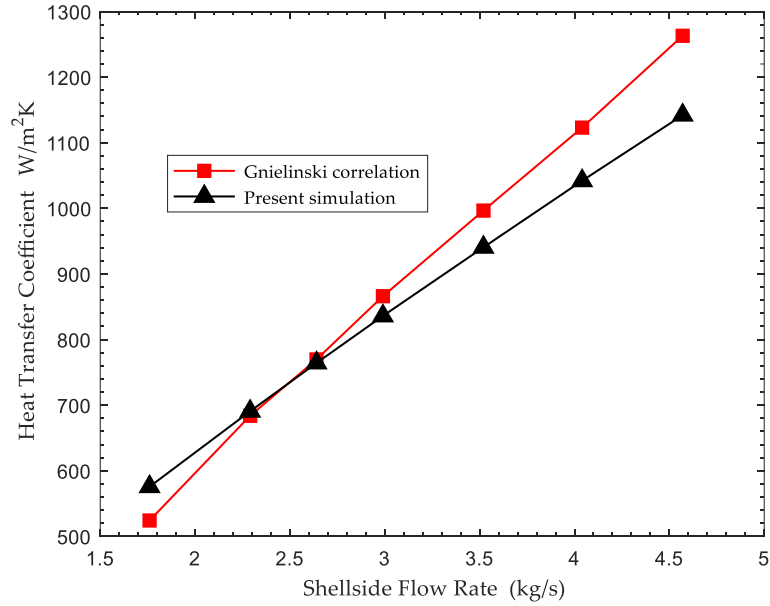
Figure 4. Average heat transfer coefficient comparison between Gnielinski correlation and CFD shell-side flow model.

3.3. *Mesh Independency*

Geometrical models and mesh systems were created with ANSYS Design Modeler and ANSYS Meshing. As shown in Figure 5, tetrahedral grids were adopted as the main mesh structure, and a non-conformal mesh approach has been considered to account for fluid (coolant, V), solid (baffles, VI) and porous media (reactor tubes VII) sub-domains. Different cell zones are coupled together through interface boundary conditions to allow heat transfer. Coolant cell zones (fluid domain) were modelled by means of tetrahedral grids, which were made finer in near wall regions through appropriate inflation layers. A structured (hexahedral) mesh was adopted for reactor tubes (porous media). These were made finer near tubes inlet to capture the chemical reaction phenomena and the heat coming from the catalyst bed to the fluid (coolant) domain. Refinement has been performed until the y+ value of the first layer grid meets standard wall functions requirements. Mesh independence tests are carried out considering four mesh densities (Table 4). Average CO_2 mole fraction at tube outlets and hot spot temperature inside tubes were calculated as representative variables. All mesh systems differ slightly in terms of maximum temperature and CO_2 mole fraction as well. As a result, the first mesh (4.2×10^6) system was adopted to represent the physical model considering the balance between accuracy and workload. Boundary conditions for mesh independence summarize as follows: Thermal oil flow rate of 7 m³/h (1.7 kg/s) at 523.15 K in coolant inlet (I), thermally coupled interface boundary conditions at coolant-tube and baffle-coolant interfaces (II), adiabatic external walls (III) and pressure outlet (IV). Operational pressure has been set at 1 bar for coolant cell zones and 10 bar for tube cell zones.
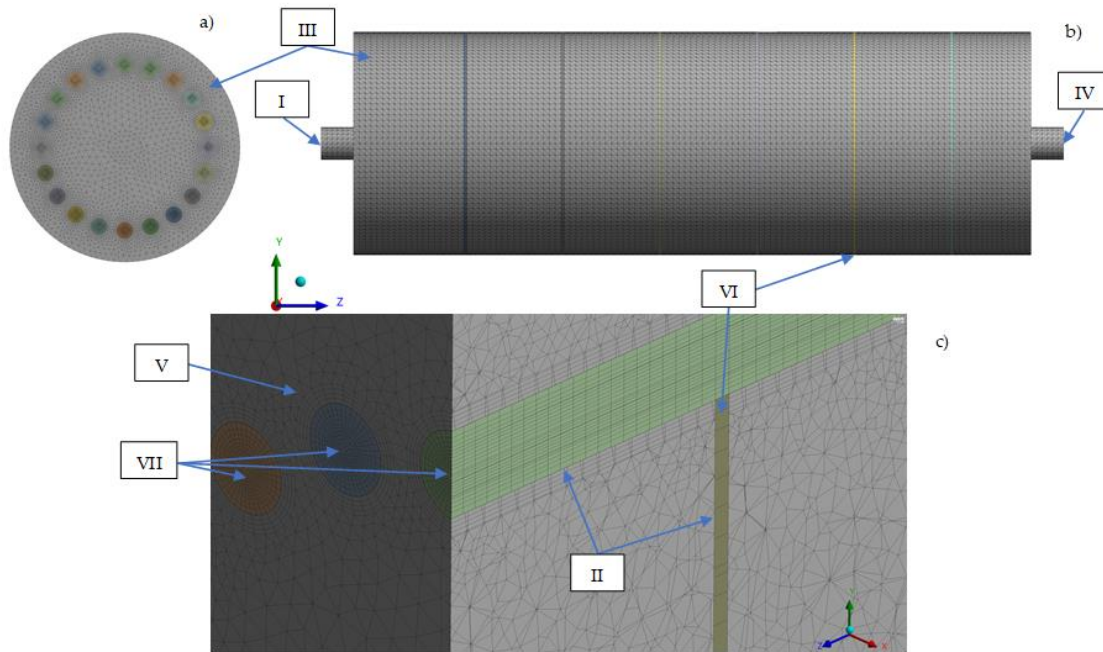
Figure 5. Mesh system for 1 m methanation module. (**a**) Front view of the reactor. (**b**) Longitudinal view. (**c**) Mesh system and sub domains detail.

Table 4. Mesh independence test results.

Mesh Count	Tube Average Outlet Temperature (K)	Tube Average CO_2 Outlet (mol Fraction)
4.2×10^6	251.768	0.01430
4.7×10^6	251.764	0.01428
5.1×10^6	251.759	0.01425
6.8×10^6	251.748	0.01419

3.4. Design study

Parametric studies were conducted to investigate the effect of coolant flow rate and coolant type (molten salts and thermal oil). In addition, key reactor performance parameters were evaluated: (1) maximum tube temperature, (2) CO_2 conversion, (3) shell-side flow pressure drop and (4) average coolant temperature. CFD simulations were performed at coolant (molten salts and thermal oil) feed rates of: (1) **14**, (2) **7**, (3) **3.5** and (4) **1 m³/h**. Scalable wall functions were implemented for near wall numerical calculation to avoid problems of successive mesh refinements due to different y+ values in each case. Furthermore, the impact of coolant type on reactor performance was considered in terms of consumed specific pumping power (kW of pumping power/kmol CH_4 produced) and hot spot temperature. Two commercially available coolants were selected: thermal oil [64] and molten salt [65]. Disk and doughnut potential in controlling the hot spot was also analysed by comparing two baffle configurations. Although numerical heat transfer results showed a good agreement with Gnielinski correlation in the range of 7–18 m³/h, lower flow rates (1–3.5 m³/h) were also considered for their relevance in hot spot generation and control. However, for the sake of design safety, results in the lower flow bracket should be taken only qualitatively.

3.4.1. Coolant Type Analysis

After the successful validation of the CFD model, the effect of coolant type and flow was investigated. First, by contrasting the coolant type and volumetric flow, the effects of these factors on reactor performance (heat transfer, CO_2 conversion and pumping power) were assessed. Performance parameters predicted by the CFD model are presented in Table 5. Regarding maximum (hot spot) temperature, there was a difference of 20 K between maximum and minimum flow rates, but no significant differences among coolant types for equal flows. Likewise, average tube temperature

45

exhibits an expected difference between maximum and minimum flow rates (58 K). The lowest flow rate pair also shows a significant difference (max. 26 K) among coolant types. It is important to consider that a larger increment of coolant temperature may result into a considerable loss in coolants density, diminishing its capacity to remove heat. In this study however, it was assumed a constant density given the small differences in coolant temperature. This behaviour is clearly explained from tube to coolant average heat transfer coefficient results, where molten salt exhibits a better performance in terms of heat transfer rate, especially for low coolant flowrates (5% superior to oil at 0.2 kg/s). This effect becomes less pronounced as the flow increases, since molten salt's thermophysical properties represented in the Prandtl number, Equation (17), play an important role in increasing heat transfer at low Reynold numbers (Equations (20) and (21)). However, the most important difference between the selected coolants lies in the field of energy efficiency. The thermophysical properties which make molten salts more effective in low-flow regimes (kinematic viscosity and density) increase the pumping power required by five times (Equation (25)), with respect to thermal oil, for the same flow rate. Consequently, positive heat transfer properties of molten salts are greatly overcome by their unsatisfactory hydrodynamic performance. Therefore, thermal oil was chosen as the standard coolant for subsequent simulations.

Table 5. Reactor Performance comparison between coolants (molten salt vs. thermal oil).

Coolant Flow and Type	Max Temperature (K)	Tube Average Temperature (K)	Coolant Average Temperature (K)	CO_2 Conversion (%)	Shell-Side Pressure Drop (Pa)	Average Heat Transfer Coefficient (W/m²K)	Specific Pumping Power (kW/kgmol CH_4)
Molten salt Thermal oil (1 m³/h)	890.9 896.3	590.9 616.1	528.3 541.2	93.0 94.0	29 12	104 57	56 23
Molten salt Thermal oil (3.5 m³/h)	885.6 885.2	566.7 571.5	525.5 526.9	91.2 91.7	491 218	235 184	3310 660
Molten salt Thermal oil (7 m³/h)	880.8 880.7	561.5 563.4	524.3 525.1	90.2 90.6	1954 871	413 338	26,880 5360
Molten salt Thermal oil (14 m³/h)	880.1 879.5	558.3 558.9	523.7 524.1	89.4 89.4	7750 3480	760 645	215,500 43250

3.4.2. Coolant Flow Rate Analysis

In this study, one of the most critical problems is the elucidation of the minimum thermal oil flow rate at which the temperature control problem is efficiently solved. CFD simulations were carried out at thermal oil feed rates of: (1) **0.2**, (2) **1**, (3) **1.7** and (4) **3.5 kg/s** (**1**, **3.5**, **7** and **14 m³/h** respectively). As coolant mass flow varies, the minimum flow rate to control the temperature at hot spot position is thus determined. Figure 6a reports the simulated axial temperature profile along reactor length, while Figure 6b shows the radial temperature profile at hot spot. Based on simulation results, it is possible to position the hot spot at 75 mm from the tubes inlet, as seen in Figure 6a. As heat transfer coefficient increases, there is an obvious decrease on the reactor temperature profile. This improvement in reactor performance is less evident for faster coolant flow rates. The highest coolant flow rate (14 m³/h) shows only a marginal difference against the 7 m³/h temperature profile. The same trend applies for shell-side average temperature, where the fastest flow implies a nearly isothermal operation for the coolant, while at the lowest feed rate, an increase in nearly 50 K is appreciated. This suggests that subsequent increments in coolant flow rate beyond 3.5 m³/h does not promote hot spot control significantly and just slightly contribute to maintaining the average tube temperature at an enormous cost in additional pumping power. Only the slowest flow rate (1 m³/h) reaches a significantly higher outlet temperature (549 K), while all other cases tend to reach the operational coolant temperature ≈ 523.15 K. Figure 7, depicts the average heat transfer coefficient at tube surface and the hot spot temperature at Z=400 mm

from the inlet. While maximum temperature is well managed below 923 K in all cases, as coolant flow goes below 3.5 m³/h, a drastic increase in maximum temperature was observed, suggesting that an average heat transfer coefficient of less than ≈200 W/m²K promotes thermal run-away and therefore it can be considered as a limit to allow a safe and stable operation. This drastic decrease in temperature observed at the critical 3.5 m³/h flow (Reynolds 6700) may be attributed to the fact that this heat transfer rate closely overcomes the heat generation rate due to chemical reactions ($S_{h,rxn}$, Equation (7)). Although a flow of 3.5 m³/h (1 kg/s) appears as an optimal operational point, it was not considered for subsequent simulations (Flow field and Species distribution) since it lies out of Gnielinski correlation validity (Figure 4). Therefore, a coolant flow of 7 m³/h (1.7 kg/s) was adopted as the optimal design coolant flow.

Figure 6. (**a**) Effect of thermal oil feed rate on the axial temperature profile, at representative tube centerline (1-m reactor module). (**b**) Effect of thermal oil feed rate on the radial temperature profile at hot-spot (1-m reactor module).
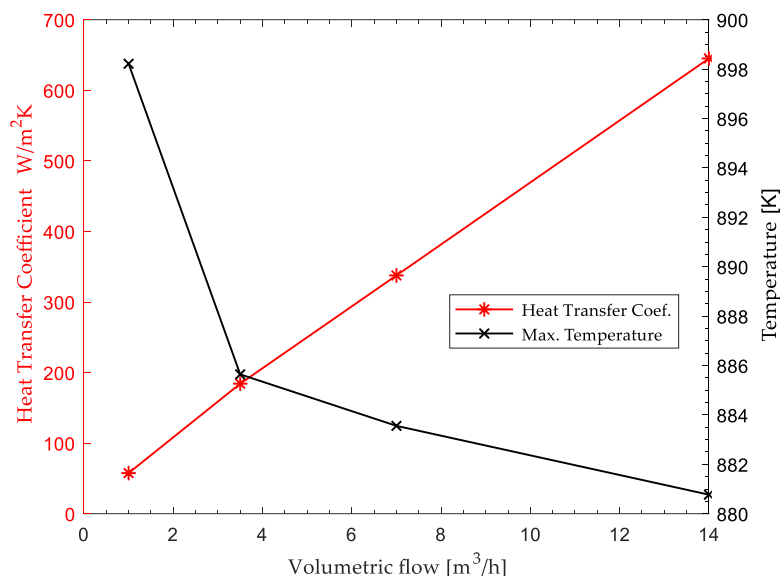
Figure 7. Average heat transfer coefficient at reactor tubes surface (1-m reactor module) and maximum hot spot temperatures for different Thermal oil feed rates.

3.4.3. Coolant Flow Field Analysis

Figure 8 describes the longitudinal coolant velocity field at reactor middle plane (yz) x = 0 for a feed rate of 7 m³/h (1.7 kg/s) and thermal oil as the fluid of choice. As coolant flows proceed across all baffles, it is possible to distinguish zones in crossflow (1) and vortex formation through doughnut openings (2). Crossflow zones, while maximizing heat transfer, also generate intermittent recirculation zones, which lead to the existence of stagnant areas of low heat transfer (3). Nevertheless, a regular flow pattern assures that all tubes are subjected to the same cooling conditions across the reactor length, guaranteeing performance uniformity among individual tubes. Indeed, coolant flow distribution suggests that an additional row of tubes may be added to make use of the parallel flow zones (4), contributing to process intensification in terms of CH_4 production. Figure 9 shows the characteristic transverse sections of coolant flow in the Disk and Doughnut reactor. Figure 9a shows the radial flow velocity vector at the hot spot position. Clearly, tubular reactors benefit from the Disk and Doughnut configuration since the baffle arrangement maximizes radial velocity at the first disk. This greatly improves the heat transfer capability if the first disk is correctly positioned to match the hot spot, as shown in Figure 10. Conversely, Figure 9b is positioned at the recirculation zone, showing poor flow features due to stagnation. Figure 9c shows a uniform crossflow zone among all tubes converging through the doughnut, while Figure 9d illustrates the expansion zone at the doughnut's outlet. Both zones maintain a uniform crossflow pattern of an average of 0.2 m/s between tubes, which promotes turbulence (Re ≈ 14,000) and heat transfer as well.
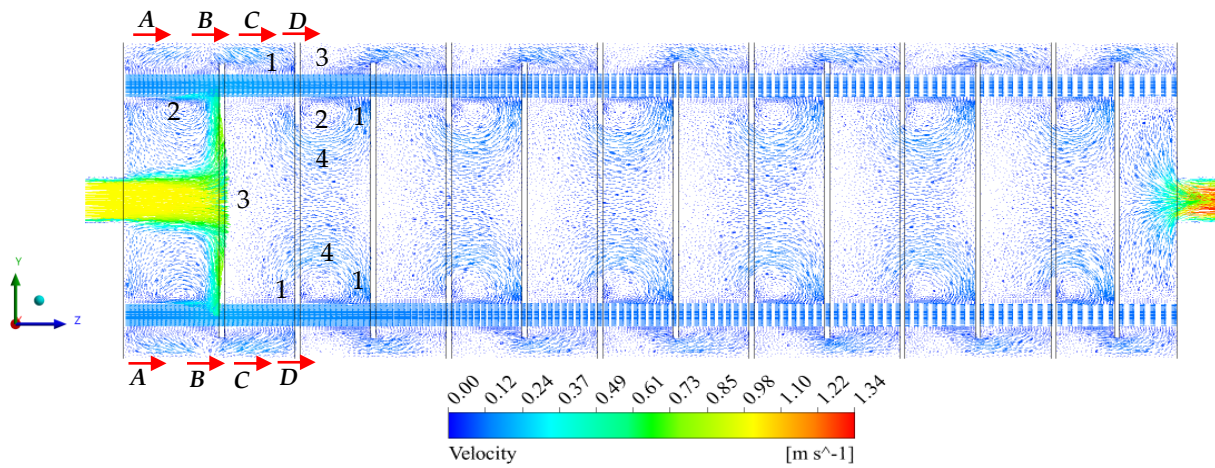
Figure 8. Reactor, longitudinal Velocity Flow field at X = 0, plane-YZ.
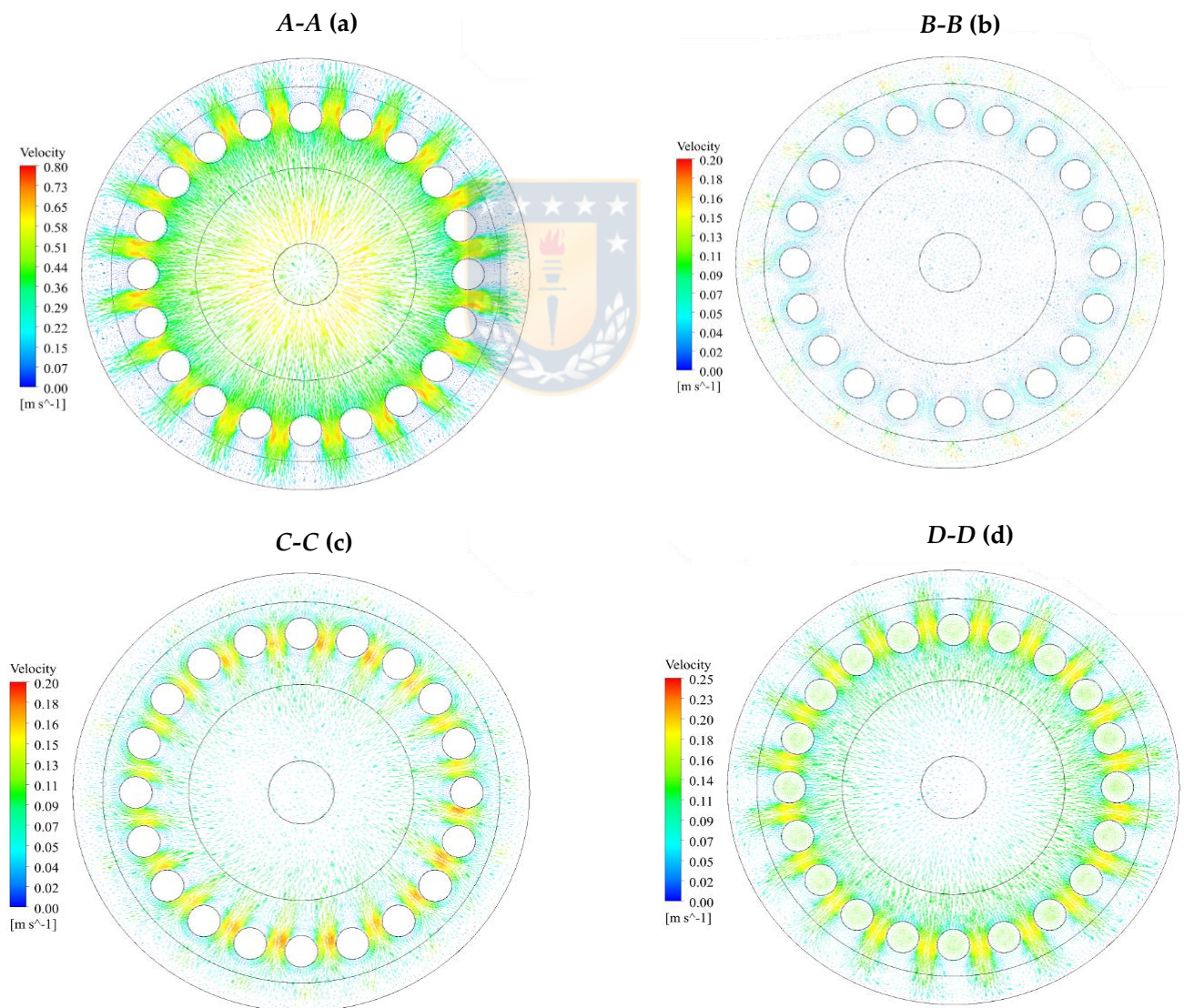
Figure 9. Reactor, Transversal cuts at Z = 65-mm (*A-A*) (**a**), 95-mm (*B-B*) (**b**), 130-mm (*C-C*) (**c**), 175-mm (*D-D*) (**d**).
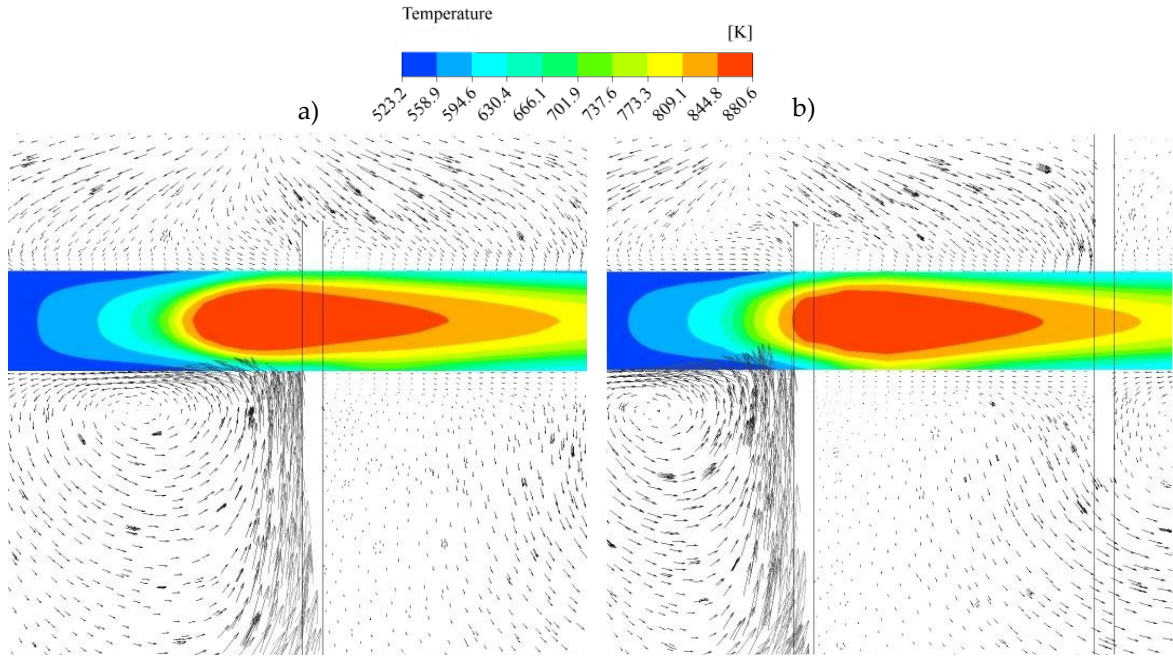
Figure 10. Hot spot detail at x = 0 cut plane, (**a**) baffle at hot spot position, (**b**) baffle positioned according to standards.

Figure 10 illustrates the temperature distribution along the longitudinal section x = 0, for two alternative baffle positions at nominal operation conditions and thermal oil coolant flow of 7 m³/h. Figure 10b shows the reactor with baffle distancing as recommended by Thulukkanam [49], while Figure 10a shows an optimized baffle positioning to fit the hot spot location. The temperature distribution is visibly related to the baffle position, redirecting the main coolant flow radially as it expands from the inlet. Fluid velocity and heat removal are thus maximized, reducing the temperature gradient at the hot spot. Therefore, baffle positioning seems critical in the reactor design process to accommodate and reduce stagnant zones, improving the heat transfer effects.

3.4.4. Species Concentration Analysis

As it is characteristic of all exothermic processes, most of the reaction takes place in the first quarter of the tubular reactor. This can be appreciated from the drastic reduction in CO_2 concentration shown in Figure 11. The high reactants concentrations greatly promote reaction kinetics and reaction heat released. In this section, heat control is essential to guarantee a safe reactor operation and minimize carbon deposition and sintering.

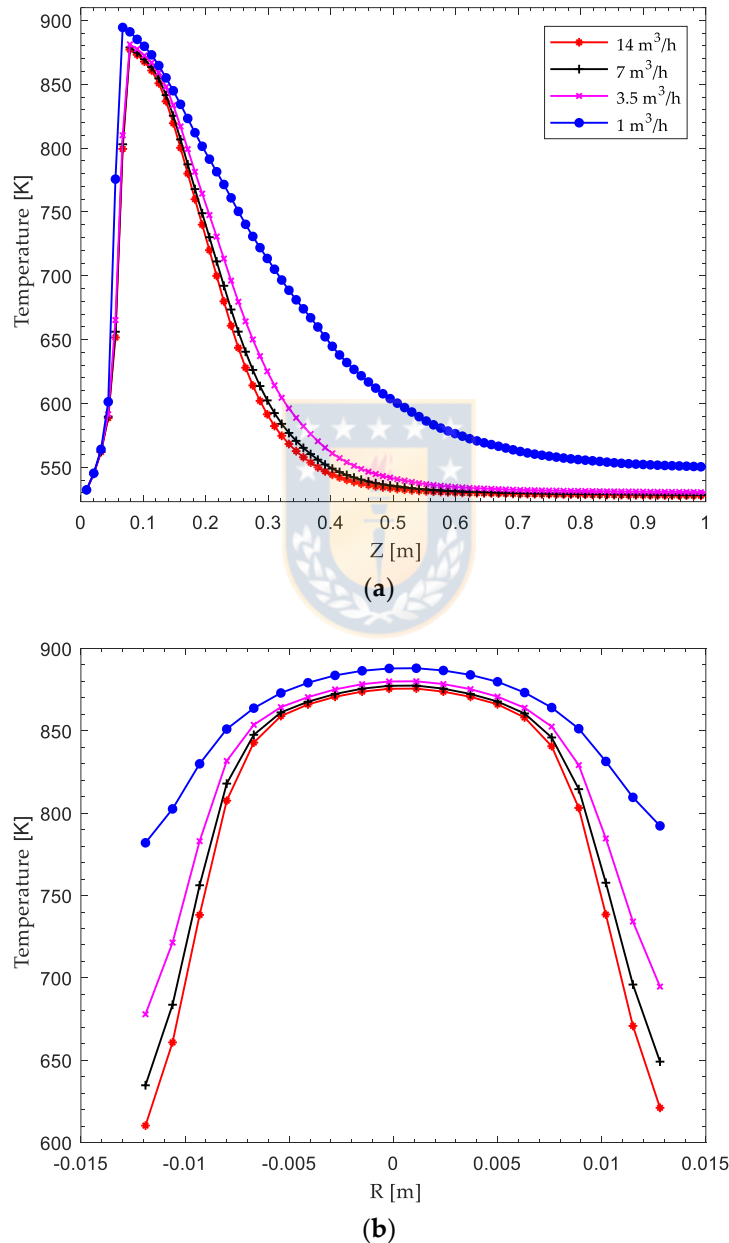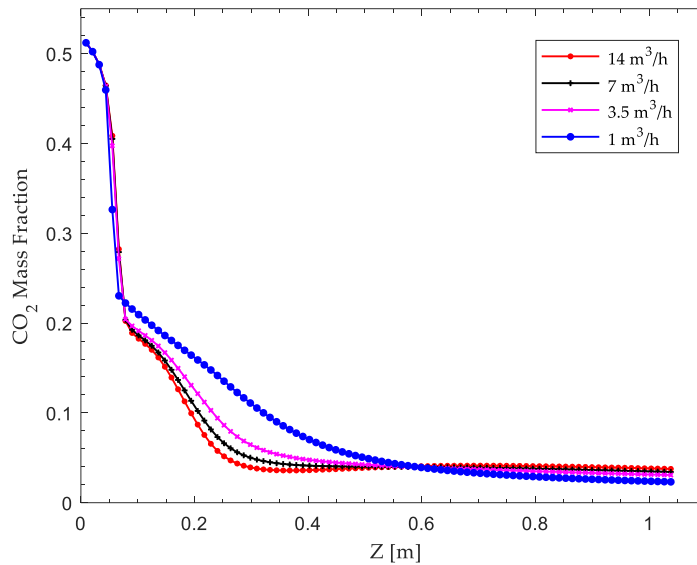**Figure 11.** Effect of thermal oil feed rate on the axial CO_2 profile at representative tube centerline (1-m reactor module).

At z = 0.575 m from the inlet, it is evident that as reactants concentration diminish, heat generation decreases accordingly due to slower reaction rates. In this reactor section, kinetics becomes less relevant as the reaction (Equation (1)) approaches equilibrium. Consequently, thermodynamic effects gain relevance as the reactor temperature reaches the coolant temperature. Therefore, it is critical to ensure that the chosen catalyst remains active at coolant temperature in this second section. While heat removal in the "kinetic" section is improved at lower coolant temperatures, in the "thermodynamic driven" section, it may hinder CO_2 conversion due to diminished catalyst activity.

Figures 12 and 13 reports the resulting CH_4 and CO_2 mass fraction at the Y = 0 longitudinal cut at nominal conditions and a 7 m^3/h thermal oil flow, showing a maximum methane mass fraction of 0.537 at reactor outlet, which means a methane mole fraction of 0.89 after water condensation as detailed in Table 6. Despite the reaction extent reached in a 1 m length reactor, it is not possible to achieve the quality required for the produced SNG to be injected into the gas grid. Therefore, an additional module is needed. Back to Table 5, it is important to notice that slower coolant flow rates promote CO_2 conversion up to 5% more than the nominal case (thermal oil 1 m^3/h) due to a poorer heat removal capability, resulting in an increase of 50 K in the average reactor temperature. Although this may seem like an alternative to improve CO_2 conversion, thermal runaway risks make this option not recommendable. Therefore, a second 0.5 m reactor of the same configuration described in Table 2 is proposed to convert the remaining CO_2 and fulfil SNG quality requirements after an intermediate condensation step, as proposed by El-Sibai et al. [30] and Witte et al. [21]. For simplicity, all water is removed and product gases after the first reactor are assumed as the second reactor inlet composition. The rest of the boundary conditions remain the same. As most produced water is removed, reaction equilibrium is shifted to products, improving reaction performance in this second step as shown in Figures 14 and 15. After this second methanation step, final SNG quality reaches acceptable levels. See Table 7 below. The proposed design proved able to upgrade biogas to SNG and under thermally safe operational conditions.
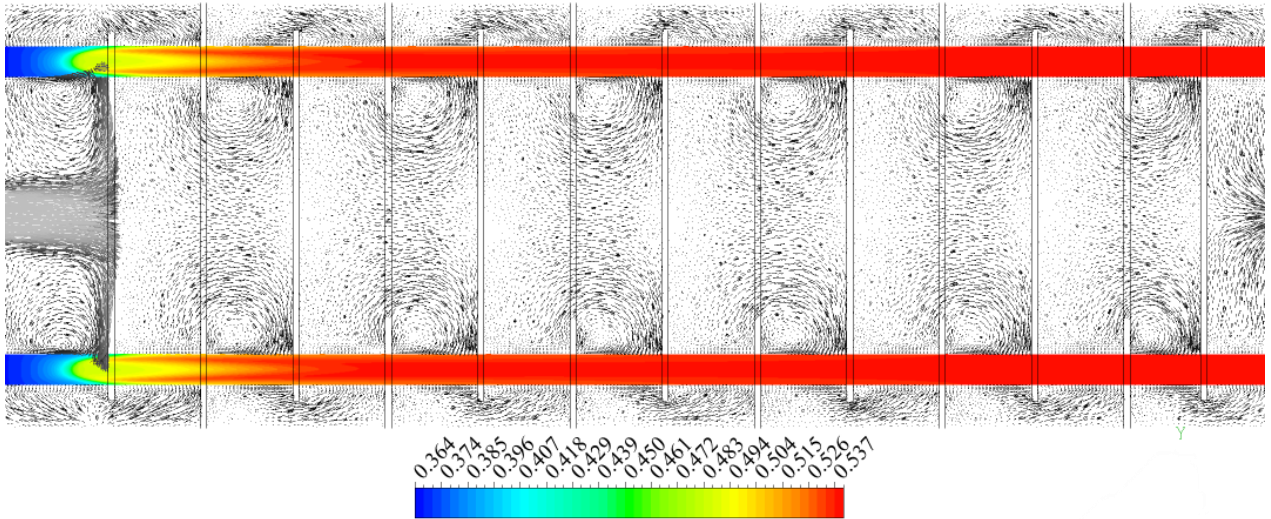
Figure 12. Reactor, longitudinal CH_4 mass fraction profile at x = 0, plane yz.
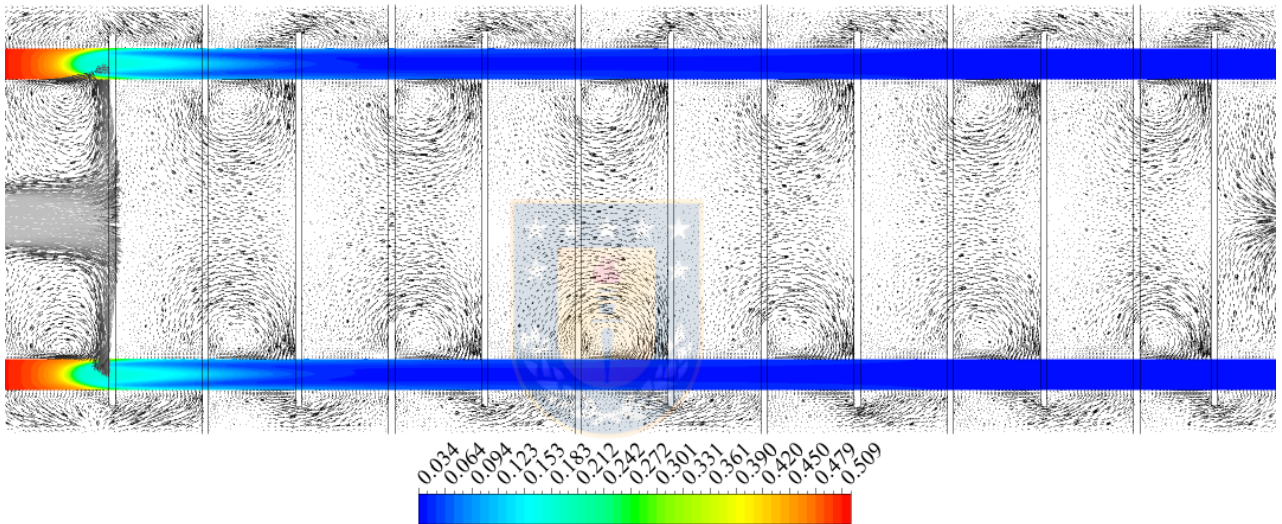
Figure 13. Reactor, longitudinal CO_2 mass fraction profile at x = 0, plane yz.

Table 6. Outlet gas composition and SNG quality requirements (1 m reactor module).

Species (Inert Species Neglected)	SNG Target Composition % [52]	Outlet Comp. after H_2O Cond. %	Mass Fraction at Outlet
CH_4	≥ 95	89	0.54
CO_2	≤ 2.5	2	0.036
H_2	≤ 5	9	0.007
H_2O	≈ 0	≈ 0	0.418

Table 7. Outlet gas composition and SNG quality requirements (0.5 m reactor module).

Species (Inert Species Neglected)	SNG Target Composition % [52]	Outlet Comp. after H_2O Cond. %	Mass Fraction at Outlet
CH_4	≥ 95	97.8	0.9475
CO_2	≤ 2.5	0.42	0.0044
H_2	≤ 5	1.68	0.0008
H_2O	≈ 0	≈ 0	0.0472
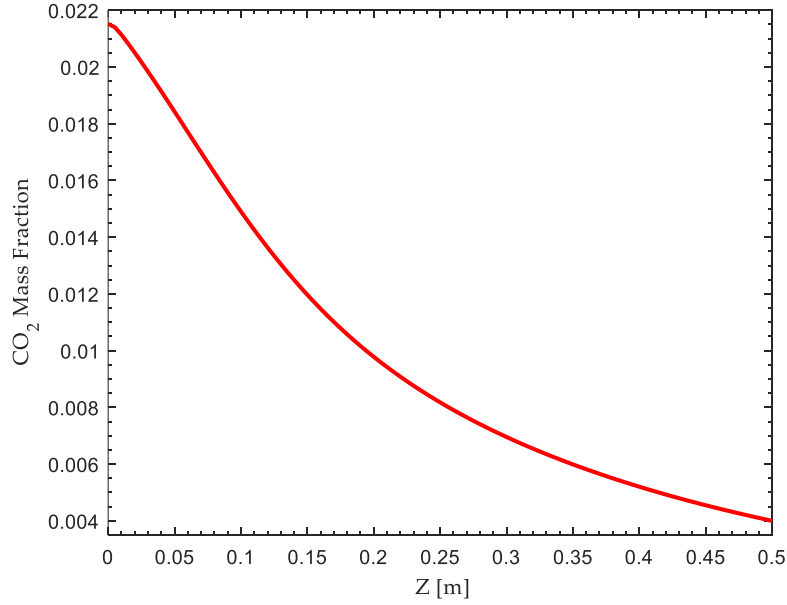
Figure 14. Axial CO_2 mass fraction profile at representative tube centerline (0.5-m reactor module) under 7-m³/h thermal oil feed rate.
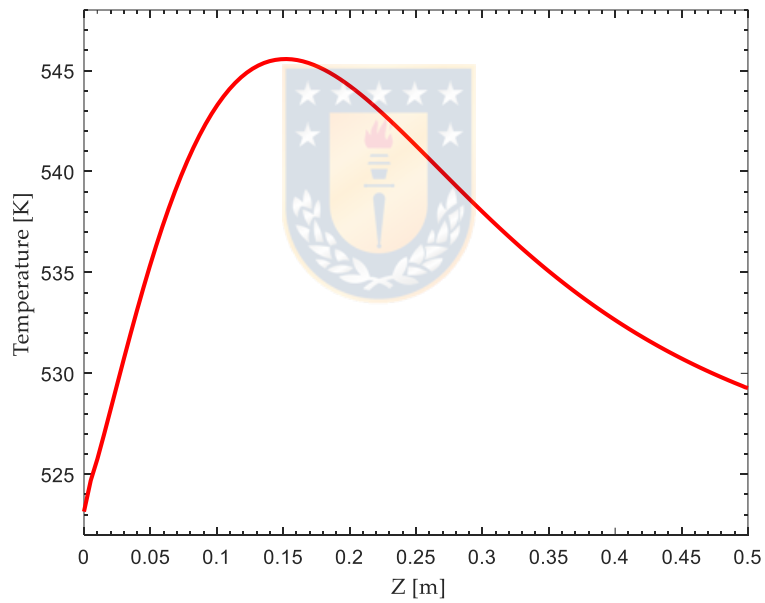
Figure 15. Axial temperature profile at representative tube centerline (0.5-m reactor module) under 7-m³/h thermal oil feed rate.

4. Conclusions

In this study, the relevance of design features and coolant types on a fixed bed multi-tubular reactor were evaluated through a CFD-based methodology. A comprehensive disk and doughnut design was used for parametric studies involving thermal oil and molten salts for four different coolant flow rates. The adopted kinetics parameters can satisfactorily represent the hydrogenation of CO_2 under the considered operational conditions, with a maximum error of 20% at tube inlet. Moreover, hot spot position is accurately predicted with a 5% error between numerical and experimental data. CFD-calculated heat transfer coefficients coincide with Gnielinski correlation for a coolant mass flow range of 1.7–4.6 kg/s (7–18 m³/h for thermal oil) with a maximum error of 10%. Tube to coolant heat transfer coefficients calculated from empirical correlations should consider the range of validity of such correlations to represent the actual tube to coolant heat transfer. At the lowest coolant flow (1 m³/h),

53

heat transfer coefficients obtained for molten salt cooling were 82% higher than thermal oil. Average temperature inside tubes for the molten salt-cooled reactor, were 26 K lower than the equivalent thermal oil-cooled reactor. Hot spot temperature difference between coolants was less pronounced (6 K). Regarding coolant maximum temperature, no significant increments were observed in all simulations (561 K max. for 1 m^3/h thermal oil flow). Therefore, coolant decomposition is not expected. As the coolant flow increases, the heat transfer performance difference between coolants tends to diminish. A critical flow of 3.5 m^3/h has been identified, after which no substantial improvements in heat transfer performance are observed. An increase in coolant flow from 3.5 m^3/h to 7 m^3/h implies an increment in eight times the pumping power in return for marginal improvements. An additional increment in cooling from 7 m^3/h to 14 m^3/h further increases the consumed pumping power, with almost no performance improvement. Among coolants, it is found that molten salt cooling increases the pumping power required per k_{mol} of methane produced by five times (in comparison with thermal oil) due to a greater viscosity and density. The disk and doughnut configuration proved highly efficient in terms of maintaining a uniform flow-field among tubes. All tubes are subjected to the same cooling conditions, no matter the position. Stagnation zones found behind baffles did not severely impact the cooling performance of the tubes; neither showed relevant increments in coolant temperature. Regarding hot spot temperature control, the first baffle position was critical to allowing the fastest coolant stream to match the hot spot's intensifying heat transfer in the most demanded zone. CFD results demonstrated that faster coolant flow rates generated a sharper declining temperature profile in the reactor, diminishing CO_2 conversion (89.4% at max. cooling), while the slower coolant flow rate (1 m^3/h) promotes the conversion up to 94%, due to a lesser heat removal capability resulting in an increase of 50 K in the average reactor temperature. Nevertheless, operation at such low flows is not encouraged due to the observance of thermal runaway behaviour. Although product gas at the reactor outlet does not fulfil SNG requirements, an intermediate condensation step and a second reactor of 0.5 m are incorporated, improving CO_2 conversion and enhancing CH_4 content. Final number of modules (1 m reactor + intermediate condensation + 0.5 m reactor) required to upgrade 150 Nm^3/h of biogas are 30 and 1200 tubes in total.

Author Contributions: V.S. contributed with CFD simulations and writing the original draft. X.G. and C.U. contributed with writing, supervision, and editing.

5. Abbreviations

CFD	Computational Fluid Dynamics
UDF	User Defined Function
PMM	Porous Media Model
PRCFD	Particle resolved CFD
TEMA	Tubular Exchanger Manufacturers Association
RNG	Renormalisation group
SNG	Substitute natural gas
LHHW	Langmuir Hinshelwood Hougen Watson
SIMPLE	Semi-Implicit Method for Pressure Linked Equations
PtM	Powe to methane
GHSV	Gas hourly space velocity

Symbols:

A	Tube external area	(m^2)
c_p	Specific heat capacity	(J kg^{-1} K^{-1})
C_μ	Realizable coefficient	(-)
d_t	Tube external diameter	(m)
D_p	Particle diameter	(m)
D_{ij}	Binary molecular diffusion coefficient	(m^2/s)
E	Total energy	(J/kg)

Symbol	Description	Units
E_A	Activation Energy	(J/mol)
g	Acceleration of gravity	(9.81 m/s^2)
h	Enthalpy	(J/kg)
h_{row}	Heat transfer coefficient, Gnielinski	(W m^{-2} K^{-1})
h_{num}	Heat transfer coefficient, CFD	(W m^{-2} K^{-1})
h_w	Differential head	(m)
ΔH	Enthalpy change	(kJ/mol)
$h_i{}^0$	Enthalpy of formation of species i	(J/kg)
ΔH_{ads}	Heat of adsorption	(J/mol)
I	Identity matrix	(-)
j	Mass diffusion flux	(Kg s^{-1} m^{-2})
k_0	Arrhenius Pre exponential factor	(kmol bar^{-1} kg$_{cat}{}^{-1}$)
K_0	Van't Hoff Pre exponential factor	(bar$^{-0.5}$)
K_i	Adsorption constant of species i	(bar$^{-0.5}$)
K_{eq}	Equilibrium constant	(-)
k_r	Reaction rate coefficient	(kmol bar^{-1} kg$_{cat}{}^{-1}$ s^{-1})
k	Turbulent kinetic energy	(m^2 s^{-2})
L_{bed}	Catalytic bed length	(m)
l	Tube streaming length	(m)
M_{wi}	Molecular weight of species i	(kg/kmol)
$Nu_{l,lam}$	Laminar component of Nusselt number	(-)
$Nu_{l,tur}$	Turbulent component of Nusselt number	(-)
$Nu_{0,row}$	Nusselt number for a single row of tubes	(-)
p	Static pressure	(Pa)
Pr	Prandtl number	(-)
P_h	Pumping power	(kW)
r_i	Molar Rate of formation of species i	(kmol m^{-3}s^{-1})
q	Coolant flow	(m^3/h)
Q_w	Surface heat flux at tube walls	(W)
R_i	Mass rate of formation of species i	(kg m^{-3}s^{-1})
R	Universal Gas Constant	(8.314 J mol^{-1} K^{-1})
R_{dp}	Reynolds number based on particle diameter	(-)
Re_p	Reynolds number based on particle diameter and mean porosity	(-)
Re_{dt}	Reynolds number based on particle diameter and confining diameter	(-)
$Re_{\psi,l}$	Reynolds number for a single row of tubes in crossflow	(-)
T	Temperature	(K)
T_{ref}	Reference temperature	(K)
t_p	Tube pitch	(-)
U	Mean flow velocity	(m s^{-1})
U_w	Mean average velocity in the void between tubes	(m s^{-1})
v	Linear velocity	(m s^{-1})
$y+$	Dimensionless wall distance	(-)
Y	Species mass fraction	(kg/kg)
	Greek letters	
α	Thermal diffusivity	(m^2 s^{-1})
ε	Turbulent dissipation rate	(m^2 s^{-3})
ρ	Density	(kg m^{-3})
λ	Thermal conductivity	(W m^{-1} K^{-1})
λ_t	Turbulent thermal conductivity	(W m^{-1} K^{-1})

λ_{eff}	Effective thermal conductivity	(W m⁻¹ K⁻¹)	
φ	Bed porosity	(-)	
$\bar{\bar{\tau}}$	Shear Stress tensor	(-)	
κ	Permeability	(m²)	
μ_φ	Effective viscosity in porous media	(kg m⁻¹ s⁻¹)	
μ_t	Turbulent viscosity	(kg m⁻¹ s⁻¹)	
μ_g	Gas phase viscosity	(kg m⁻¹ s⁻¹)	
ν	Kinematic viscosity	(m² s⁻¹)	
ψ	Void fraction between adjacent tubes in a row	(-)	
	Subscripts		
f	Fluid (liquid) phase		
g	Fluid (gas) phase		
i	Species index		
j	Species index		
s	Solid (catalyst)		
st	Solid (stainless steel)		

6.   Appendix A. Thermodynamic, Physical Properties and Kinetic Parameters

Property	Value	Unit	Reference
Gas mixture			
Specific heat (C_{pg})	Mixing-law	J kg⁻¹K⁻¹	[58]
Thermal conductivity (λ_g)	Ideal gas mixing law	W m⁻¹ K⁻¹	[58]
Density (ρ_g)	Incomp. ideal gas	Kg m⁻³	[58]
Viscosity (μ_g)	Ideal gas mixing law	Kg m⁻¹ s⁻¹	[58]
Binary molecular diffusion coefficient (D_{ij})	Chapman-Enskog	m² s⁻¹	[61]
Catalyst bed			
Bulk density (ρ_s)	1535	Kg m⁻³	[35]
Specific heat (C_{ps})	880	J kg⁻¹K⁻¹	[20]
Thermal conductivity (λ_s)	0.67	W m⁻¹ K⁻¹	[41]
Particle Diameter (d_p)	2.6	mm	[11]
Bed porosity	0.39	-	[20]
Permeability	1.045×10^{-8}	m²	[58]
Inertial resistance	12,000	m⁻¹	[58]
Coolant (molten salt)			
Density (ρ_f)	1930	Kg m⁻³	[65]
Specific heat (C_{pf})	1590	J kg⁻¹K⁻¹	[65]
Viscosity (μ_g)	0.004	Kg m⁻¹ s⁻¹	[65]
Thermal conductivity (λ_f)	0.49	W m⁻¹ K⁻¹	[65]
Coolant (thermal oil)			
Density (ρ_f)	867	Kg m⁻³	[64]
Specific heat (C_{pf})	2181	J kg⁻¹K⁻¹	[64]
Viscosity (μ_g)	2.88×10^{-5}	Kg m⁻¹ s⁻¹	[64]
Thermal conductivity (λ_f)	0.1055	W m⁻¹ K⁻¹	[64]
Baffles & tube walls (Steel)			
Density (ρ_f)	8030	Kg m⁻³	[66]
Specific heat (C_{pf})	502	J kg⁻¹K⁻¹	[66]
Thermal conductivity (λ_{st})	16	W m⁻¹ K⁻¹	[66]
Kinetic parameters			
k_0	3.46×10^{-4}	kmol bar⁻¹ kg_cat⁻¹ s⁻¹	
E_A	77,500	J mol⁻¹	
$K_{0.OH}$	0.5	bar⁻⁰·⁵	[12]
$\Delta H_{ads,OH}$	22,400	J mol⁻¹	
$K_{0.H_2}$	0.44	bar⁻⁰·⁵	

$\Delta H_{ads,H_2}$	−6200	J mol^{-1}
$K_{0.mix}$	0.88	bar$^{-0.5}$
$\Delta H_{ads,mix}$	−10,000	J mol^{-1}
Activity factor	0.1	-

7. Appendix B. Kinetics Expressions

$$r_{CO2} = \frac{k p_{H2}^{0.5} p_{CO2}^{0.5} \left(1 - \frac{p_{CH4} p_{H2O}^2}{p_{CO2} p_{H2}^4 K_{eq}}\right)}{\left(1 + K_{OH} \frac{p_{H2O}}{p_{H2}^{0.5}} + K_{H2} p_{H2}^{0.5} + K_{mix} p_{CO2}^{0.5}\right)^2} \ , k_r = k_0 \exp\left[\frac{E_A}{R}\left(\frac{1}{T_{ref}} - \frac{1}{T}\right)\right]$$

$$K_i = K_{0.i} \exp\left[\frac{\Delta H_{ads,i}}{R}\left(\frac{1}{T_{ref}} - \frac{1}{T}\right)\right], K_{eq} = 137 \, T^{-3.998} \exp\left[\frac{158700}{RT}\right]$$

8. References

1. Denholm, P.; Mai, T. Timescales of energy storage needed for reducing renewable energy curtailment. *Renew. Energy* **2019**, *130*, 388–399, doi:10.1016/j.renene.2018.06.079.

2. Ghaib, K.; Ben-Fares, F.-Z. Power-to-Methane: A state-of-the-art review. *Renew. Sustain. Energy Rev.* **2018**, *81*, 433–446, doi:10.1016/j.rser.2017.08.004.

3. Götz, M.; Lefebvre, J.; Mörs, F.; Koch, A.M.; Graf, F.; Bajohr, S.; Reimert, R.; Kolb, T. Renewable Power-to-Gas: A technological and economic review. *Renew. Energy* **2016**, *85*, 1371–1390, doi:10.1016/j.renene.2015.07.066.

4. Schnuelle, C.; Thoeming, J.; Wassermann, T.; Thier, P.; von Gleich, A.; Goessling-Reisemann, S. Socio-technical-economic assessment of power-to-X: Potentials and limitations for an integration into the German energy system. *Energy Res. Soc. Sci.* **2019**, *51*, 187–197, doi:10.1016/j.erss.2019.01.017.

5. Rönsch, S.; Schneider, J.; Matthischke, S.; Schlüter, M.; Götz, M.; Lefebvre, J.; Prabhakaran, P.; Bajohr, S. Review on methanation—From fundamentals to current projects. *Fuel* **2016**, *166*, 276–296, doi:10.1016/j.fuel.2015.10.111.

6. Fache, A.; Marias, F.; Guerré, V.; Palmade, S. Optimization of fixed-bed methanation reactors: Safe and efficient operation under transient and steady-state conditions. *Chem. Eng. Sci.* **2018**, *192*, 1124–1137, doi:10.1016/j.ces.2018.08.044.

7. Bremer, J.; Rätze, K.H.G.; Sundmacher, K. CO₂ methanation: Optimal start-up control of a fixed-bed reactor for power-to-gas applications. *AIChE J.* **2016**, *63*, 23–31, doi:10.1002/aic.15496.

8. Alarcón, A.; Guilera, J.; Andreu, T. CO2 conversion to synthetic natural gas: Reactor design over Ni–Ce/Al₂O₃ catalyst. *Chem. Eng. Res. Des.* **2018**, *140*, 155–165, doi:10.1016/j.cherd.2018.10.017.

9. Sun, D.; Simakov, D.S. Thermal management of a Sabatier reactor for CO₂ conversion into CH4: Simulation-based analysis. *J. CO₂ Util.* **2017**, *21*, 368–382, doi:10.1016/j.jcou.2017.07.015.

10. Moioli, E.; Gallandat, N.; Züttel, A. Model based determination of the optimal reactor concept for Sabatier reaction in small-scale applications over Ru/Al₂O₃. *Chem. Eng. J.* **2019**, *375*, 121954, doi:10.1016/j.cej.2019.121954.

11. Molina, M.M.; Kern, C.; Jess, A. Catalytic Hydrogenation of Carbon Dioxide to Methane in Wall-Cooled Fixed-Bed Reactors‡. *Chem. Eng. Technol.* **2016**, *39*, 2404–2415, doi:10.1002/ceat.201500614.

12. Matthischke, S.; Roensch, S.; Güttel, R. Start-up Time and Load Range for the Methanation of Carbon Dioxide in a Fixed-Bed Recycle Reactor. *Ind. Eng. Chem. Res.* **2018**, *57*, 6391–6400, doi:10.1021/acs.iecr.8b00755.

13. Holman, J. *Heat Transfer*, 10th ed.; McGraw-Hill Education: Boston, MA, USA, 2009.

14. Hukkanen, E.J.; Rangitsch, M.J.; Witt, P.M. Non-Adiabatic Multitubular Fixed-Bed Catalytic Reactor Model Coupled with Shell-Side Coolant CFD Model. *Ind. Eng. Chem. Res.* **2013**, *52*, 15437–15446, doi:10.1021/ie4006832.

15. Hagan, P.S.; Herskowitz, M.; Pirkle, C. A Simple Approach to Highly Sensitive Tubular Reactors. *SIAM J. Appl. Math.* **1988**, *48*, 1083–1101, doi:10.1137/0148064.

16. K. Wu, K. Zhu, C. Kang, J. Zhang, X. Zhang, and C. Zhang, "Numerical Method and Its Application to Coupled System with Chemical Reaction, Fluid Flow and Heat Transfer: A Case Study of Shell-and-Tube Reactor," in 2015 IEEE 17th International Conference on High Performance Computing and Communications, 2015 IEEE 7th International Symposium on Cyberspace Safety and Security, and 2015 IEEE 12th International Conference on Embedded Software and Systems, New York, NY, USA, Aug. 2015; pp. 1488–1493, doi:10.1109/hpcc-css-icess.2015.227.

17. Jiang, B.; Hao, L.; Zhang, L.; Sun, Y.; Xiao, X. Numerical investigation of flow and heat transfer in a novel configuration multi-tubular fixed bed reactor for propylene to acrolein process. *Heat Mass Transf.* **2014**, *51*, 67–84, doi:10.1007/s00231-014-1384-3.

18. Moon, J.; Gbadago, D.Q.; Hwang, S. 3-D Multi-Tubular Reactor Model Development for the Oxidative Dehydrogenation of Butene to 1,3-Butadiene. *ChemEngineering* **2020**, *4*, 46, doi:10.3390/chemengineering4030046.

19. Chein, R.; Chen, W.; Yu, C. Numerical simulation of carbon dioxide methanation reaction for synthetic natural gas production in fixed-bed reactors. *J. Nat. Gas Sci. Eng.* **2016**, *29*, 243–251, doi:10.1016/j.jngse.2016.01.019.

20. Rönsch, S.; Ortwein, A.; Dietrich, S. Start-and-Stop Operation of Fixed-Bed Methanation Reactors—Results from Modeling and Simulation. *Chem. Eng. Technol.* **2017**, *40*, 2314–2321, doi:10.1002/ceat.201700229.

21. Witte, J.; Settino, J.; Biollaz, S.M.; Schildhauer, T.J. Direct catalytic methanation of biogas—Part I: New insights into biomethane production using rate-based modelling and detailed process analysis. *Energy Convers. Manag.* **2018**, *171*, 750–768, doi:10.1016/j.enconman.2018.05.056.

22. Schollenberger, D.; Bajohr, S.; Gruber, M.; Reimert, R.; Kolb, T. Scale-Up of Innovative Honeycomb Reactors for Power-to-Gas Applications—The Project Store&Go. *Chem. Ing. Tech.* **2018**, *90*, 696–702, doi:10.1002/cite.201700139.

23. Nuravifah, U.; Putri, S.E.; Wibisono, Y.; Budhi; Rizkiana, J. Simulation of Feed Modulation on Dynamic Fixed-Bed Reactor for CO Methanation over Ni-based Catalyst. *IOP Conf. Ser. Mater. Sci. Eng.* **2019**, *622*, 012024, doi:10.1088/1757-899x/622/1/012024.

24. Tauer, G.; Kern, C.; Jess, A. Transient Effects during Dynamic Operation of a Wall-Cooled Fixed-Bed Reactor for CO_2 Methanation. *Chem. Eng. Technol.* **2019**, *42*, 2401–2409, doi:10.1002/ceat.201900367.

25. Kosaka, F.; Yamaguchi, T.; Ando, Y.; Mochizuki, T.; Takagi, H.; Matsuoka, K.; Fujishiro, Y.; Kuramoto, K. Effect of Ni content on CO_2 methanation performance with tubular-structured Ni-YSZ catalysts and optimization of catalytic activity for temperature management in the reactor. *Int. J. Hydrogen Energy* **2020**, *45*, 12911–12920, doi:10.1016/j.ijhydene.2020.02.221.

26. Zhang, W.; Machida, H.; Takano, H.; Izumiya, K.; Norinaga, K. Computational fluid dynamics simulation of CO_2 methanation in a shell-and-tube reactor with multi-region conjugate heat transfer. *Chem. Eng. Sci.* **2019**, *211*, 115276, doi:10.1016/j.ces.2019.115276.

27. Fache, A.; Marias, F.; Guerré, V.; Palmade, S. Intermittent Operation of Fixed-Bed Methanation Reactors: A Simple Relation Between Start-Up Time and Idle State Duration. *Waste Biomass- Valorization* **2018**, *11*, 447–463, doi:10.1007/s12649-018-0507-3.

28. Fischer, K.L.; Freund, H. On the optimal design of load flexible fixed bed reactors: Integration of dynamics into the design problem. *Chem. Eng. J.* **2020**, *393*, 124722, doi:10.1016/j.cej.2020.124722.

29. Kiewidt, L.; Thöming, J. Predicting optimal temperature profiles in single-stage fixed-bed reactors for CO_2-methanation. *Chem. Eng. Sci.* **2015**, *132*, 59–71, doi:10.1016/j.ces.2015.03.068.

30. El Sibai, A.; Struckmann, L.K.R.; Sundmacher, K. Model-based Optimal Sabatier Reactor Design for Power-to-Gas Applications. *Energy Technol.* **2017**, *5*, 911–921, doi:10.1002/ente.201600600.

31. Gruber, M.; Wieland, C.; Habisreuther, P.; Trimis, D.; Schollenberger, D.; Bajohr, S.; Vonmorstein, O.; Schirrmeister, S. Modeling and Design of a Catalytic Wall Reactor for the Methanation of Carbon Dioxide. *Chem. Ing. Tech.* **2018**, *90*, 615–624, doi:10.1002/cite.201700160.

32. Giglio, E.; Deorsola, F.A.; Gruber, M.; Harth, S.R.; Morosanu, E.A.; Trimis, D.; Bensaid, S.; Pirone, R. Power-to-Gas through High Temperature Electrolysis and Carbon Dioxide Methanation: Reactor Design and Process Modeling. *Ind. Eng. Chem. Res.* **2018**, *57*, 4007–4018, doi:10.1021/acs.iecr.8b00477.

33. Uebbing, J.; Rihko-Struckmann, L.K.; Sundmacher, K. Exergetic assessment of CO_2 methanation processes for the chemical storage of renewable energies. *Appl. Energy* **2018**, *233-234*, 271–282, doi:10.1016/j.apenergy.2018.10.014.

34. Moioli, E.; Züttel, A. A model-based comparison of Ru and Ni catalysts for the Sabatier reaction. *Sustain. Energy Fuels* **2019**, *4*, 1396–1408, doi:10.1039/c9se00787c.

35. Scharl, V.; Fischer, F.; Herrmann, S.; Fendt, S.; Spliethoff, H. Applying Reaction Kinetics to Pseudohomogeneous Methanation Modeling in Fixed-Bed Reactors. *Chem. Eng. Technol.* **2020**, *43*, 1224–1233, doi:10.1002/ceat.201900535.

36. Theurich, S.; Rönsch, S.; Güttel, R. Transient Flow Rate Ramps for Methanation of Carbon Dioxide in an Adiabatic Fixed-Bed Recycle Reactor. *Energy Technol.* **2019**, *8*, doi:10.1002/ente.201901116.

37. Gruber, M.; Wiedmann, D.; Haas, M.; Harth, S.; Loukou, A.; Trimis, D. Insights into the catalytic CO_2 methanation of a boiling water cooled fixed-bed reactor: Simulation-based analysis. *Chem. Eng. J.* **2020**, *406*, 126788, doi:10.1016/j.cej.2020.126788.

38. Schlereth, D.; Hinrichsen, O. A fixed-bed reactor modeling study on the methanation of CO_2. *Chem. Eng. Res. Des.* **2014**, *92*, 702–712, doi:10.1016/j.cherd.2013.11.014.

39. Try, R.; Bengaouer, A.; Baurens, P.; Jallut, C. Dynamic modeling and simulations of the behavior of a fixed-bed reactor-exchanger used for CO2 methanation. *AIChE J.* **2017**, *64*, 468–480, doi:10.1002/aic.15874.

40. Engelbrecht, N.; Chiuta, S.; Everson, R.C.; Neomagus, H.; Bessarabov, D. Experimentation and CFD modelling of a microchannel reactor for carbon dioxide methanation. *Chem. Eng. J.* **2017**, *313*, 847–857, doi:10.1016/j.cej.2016.10.131.

41. Ducamp, J.; Bengaouer, A.; Baurens, P. Modelling and experimental validation of a CO_2 methanation annular cooled fixed-bed reactor exchanger. *Can. J. Chem. Eng.* **2016**, *95*, 241–252, doi:10.1002/cjce.22706.

42. Kreitz, B.; Wehinger, G.; Turek, T. Dynamic simulation of the CO_2 methanation in a micro-structured fixed-bed reactor. *Chem. Eng. Sci.* **2018**, *195*, 541–552, doi:10.1016/j.ces.2018.09.053.

43. Fache, A.; Marias, F. Dynamic operation of fixed-bed methanation reactors: Yield control by catalyst dilution profile and magnetic induction. *Renew. Energy* **2019**, *151*, 865–886, doi:10.1016/j.renene.2019.11.081.

44. Fache, A.; Marias, F.; Chaudret, B. Catalytic reactors for highly exothermic reactions: Steady-state stability enhancement by magnetic induction. *Chem. Eng. J.* **2020**, *390*, 124531, doi:10.1016/j.cej.2020.124531.

45. Ngo, S.I.; Lim, Y.-I.; Lee, D.; Go, K.S.; Seo, M.W. Flow behaviors, reaction kinetics, and optimal design of fixed- and fluidized-beds for CO2 methanation. *Fuel* **2020**, *275*, 117886, doi:10.1016/j.fuel.2020.117886.

46. Zimmermann, R.T.; Bremer, J.; Sundmacher, K. Optimal catalyst particle design for flexible fixed-bed CO_2 methanation reactors. *Chem. Eng. J.* **2019**, *387*, 123704, doi:10.1016/j.cej.2019.123704.

47. Shen, W.; Zhang, Y.; Zhao, L.; Ye, Y.; Tursun, Y. Micro-scale simulation and intensification of complex Sabatier reaction system in cylindrical catalyst bed. *Fuel* **2020**, *287*, 119399, doi:10.1016/j.fuel.2020.119399.

48. Gil-Carrera, L.; Browne, J.D.; Kilgallon, I.; Murphy, J.D. Feasibility study of an off-grid biomethane mobile solution for agri-waste. *Appl. Energy* **2019**, *239*, 471–481, doi:10.1016/j.apenergy.2019.01.141.

49. Thulukkanam, K. *Heat Exchanger Design Handbook*, 2nd ed.; CRC Press: Boca Raton, FL, USA, 2013.

50. Li, H.; Kottke, V. Analysis of local shellside heat and mass transfer in the shell-and-tube heat exchanger with disc-and-doughnut baffles. *Int. J. Heat Mass Transf.* **1999**, *42*, 3509–3521, doi:10.1016/s0017-9310(98)00368-8.

51. TEMA, Standards of the Tubular Exchanger Manufacturers Association, 9th edition. Tarrytown, New York, United States of America; TEMA, 2007.

52. Guilera, J.; Andreu, T.; Basset, N.; Boeltken, T.; Timm, F.; Mallol, I.; Morante, J.R. Synthetic natural gas production from biogas in a waste water treatment plant. *Renew. Energy* **2019**, *146*, 1301–1308, doi:10.1016/j.renene.2019.07.044.

53. Jürgensen, L.; Ehimen, E.A.; Born, J.; Holm-Nielsen, J.B. Dynamic biogas upgrading based on the Sabatier process: Thermodynamic and dynamic process simulation. *Bioresour. Technol.* **2015**, *178*, 323–329, doi:10.1016/j.biortech.2014.10.069.

54. Koschany, F.; Schlereth, D.; Hinrichsen, O. On the kinetics of the methanation of carbon dioxide on coprecipitated NiAl(O). *Appl. Catal. B Environ.* **2016**, *181*, 504–516, doi:10.1016/j.apcatb.2015.07.026.

55. *VDI Heat Atlas*, 2nd ed.; Springer-Verlag: Berlin/Heidelberg, Germany, 2010. Available online: https://www.springer.com/gp/book/9783540778769 (accessed on 14 October 2020).

56. Gruber, M.; Weinbrecht, P.; Biffar, L.; Harth, S.; Trimis, D.; Brabandt, J.; Posdziech, O.; Blumentritt, R. Power-to-Gas through thermal integration of high-temperature steam electrolysis and carbon dioxide methanation-Experimental results. *Fuel Process. Technol.* **2018**, *181*, 61–74, doi:10.1016/j.fuproc.2018.09.003.

57. Dixon, A.G.; Partopour, B. Computational Fluid Dynamics for Fixed Bed Reactor Design. *Annu. Rev. Chem. Biomol. Eng.* **2020**, *11*, 109–130, doi:10.1146/annurev-chembioeng-092319-075328.

58. ANSYS, Inc. *ANSYS Fluent Theory Guide*, 15th ed.; ANSYS, Inc.: Canonsburg, PA, USA, 2013.

59. Fogler, H.S. Elements of chemical reaction engineering. *Chem. Eng. Sci.* **1987**, *42*, 2493, doi:10.1016/0009-2509(87)80130-6.

60. Wehinger, G.D. Radiation Matters in Fixed-Bed CFD Simulations. *Chem. Ing. Tech.* **2019**, *91*, 583–591, doi:10.1002/cite.201800179.

61. ANSYS, Inc. *ANSYS Fluent User's Guide*, 15th ed.; ANSYS, Inc.: Canonsburg, PA, USA, 2013.

62. Wang, X.; Liang, Y.; Sun, Y.; Liu, Z.; Liu, W. Experimental and numerical investigation on shell-side performance of a double shell-pass rod baffle heat exchanger. *Int. J. Heat Mass Transf.* **2018**, *132*, 631–642, doi:10.1016/j.ijheatmasstransfer.2018.12.046.

63. Ziółkowska, I.; Ziółkowski, D. Fluid flow inside packed beds. *Chem. Eng. Process. Process. Intensif.* **1988**, *23*, 137–164, doi:10.1016/0255-2701(88)80012-6.

64. Therminol VP-1 Heat Transfer Fluid, Therminol VP-1 Heat Transfer Fluid. Available online: https://www.therminol.com/product/71093459 (accessed 25 April 2021).

65. Dynalene, Inc. Dynalene Molten Salts. Available online: https://www.dynalene.com/product-category/heat-transfer-fluids/dynalene-molten-salts/ (accessed 25 April 2021).

66. Kreith, F.; Bohn, M.; Kirkpatrick, A. Principles of Heat Transfer. *J. Sol. Energy Eng.* **1997**, *119*, 187–187, doi:10.1115/1.2887901.

IV.2 A 3D Transient CFD Simulation of a Multi-Tubular Reactor for Power to Gas Applications

Victor Soto [1,*], Claudia Ulloa [2] and Ximena Garcia [1]

[1] Carbon and Catalysis Laboratory (CarboCat), Department of Chemical Engineering, Faculty of Engineering, Universidad de Concepción, P.O. Box 160-C, Concepcion 4070386, Chile; xgarcia@udec.cl

[2] Environmental Engineering Department, Faculty of Environmental Sciences and EULA Chile Centre, Universidad de Concepción, P.O. Box 160-C, Concepcion 4070386, Chile; claudiaulloa@udec.cl

[*] Correspondence: vsotop@udec.cl

Abstract: A 3D stationary CFD study was conducted in our previous work, resulting in a novel reactor design methodology oriented to upgrading biogas through CO_2 methanation. To enhance our design methodology incorporating relevant power to gas operational conditions, a novel transient 3D CFD modelling methodology is employed to simulate the effect of relevant dynamic disruptions on the behaviour of a tubular fixed bed reactor for biogas upgrading. Unlike 1D/2D models, this contribution implements a full 3D shell cooled methanation reactor considering real-world operational conditions. The reactor's behaviour was analysed considering the hot-spot temperature and the outlet CH_4 mole fraction as the main performance parameters. The reactor start-up and shutdown times were estimated at 330 s and 130 s, respectively. As expected, inlet feed and temperature disruptions prompted "wrong-way" behaviours. A 30 s H_2 feed interruption gave rise to a transient low-temperature hot spot, which dissipated after 60 s H_2 feed was resumed. A 20 K rise in the inlet temperature (523–543 K) triggered a transient low-temperature hot spot (879 to 850 K). On the contrary, a 20 K inlet temperature drop resulted in a transient high-temperature hot spot (879 to 923 K), which exposed the catalyst to its maximum operational temperature. The maximum idle time, which allowed for a warm start of the reactor, was estimated at three hours in the absence of heat sources. No significant impacts were found on the product gas quality (% CH_4) under the considered disruptions. Unlike typical 1D/2D simulation works, a 3D model allowed to identify the relevant design issues like the impact of hot-spot displacement on the reactor cooling efficiency.

Keywords: CO_2 methanation; biogas upgrading; CFD; multi-tubular reactor; power to gas

1. Introduction

Renewable energy development is significantly hindered by the uncontrollable intermittence of most renewable resources and the unfeasibility of electricity storage. In this scenario, mass conversion of electrical power in the form of methane and/or hydrogen (power to gas) stands out as a potential solution to balance the electrical grids while at the same time offering an alternative for CO_2 valorisation if the Sabatier reaction Equation (1) is used for this purpose [1]. However, the high exothermicity of this reaction severely hinders the development of this technology on an industrial scale. Consequently, the design of heat removal/cooling systems remains a priority to further develop methanation reactors at the pilot and industrial scale.

The increasing interest in the development of methanation pilot plants [2,3] encourages the need for new models and designs capable of dealing with the operational challenges inherent to power to gas conditions.

$$CO_2 + 4H_2 \leftrightarrow CH_4 + 2H_2O \quad \Delta H_r^0 = -165.0 \frac{\text{kJ}}{\text{mol}} \tag{6}$$
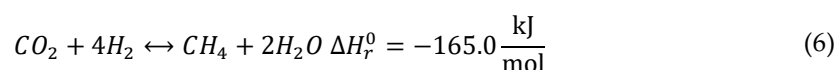
While the reviewed literature expresses a special interest in fixed-bed tubular models (for their simplicity and technological readiness [4]), a lack of insight regarding a comprehensive 3D simulation of a tubular methanation reactor under PtM conditions exists. 3D simulations remain the unique alternative to understanding how a reactor model behaves in close to real-world conditions. On the

contrary, current research works mainly focus on 1D single tube simplified reactors. Although they remain acceptable for process-focused studies [5,6], 3D models have proven necessary for designing industrial-sized reactors [7,8]. According to the authors' knowledge, no current research addressed a 3D transient reactor simulation for biogas upgrading. One of the main drawbacks of simplified models is the absence of insight regarding the interaction of heat transfer mechanisms (coolant flow) and reaction engineering. Unlike transient 1D models, which incorporate heat transfer phenomena through constant heat transfer coefficients, in this work, we consider a close to real-world modelling scenario by combining both flow dynamics and chemical kinetics into a single CFD model. Our previous research [4] demonstrated the relevance of considering a turbulent model to characterise the shell-side flow since heat transfer coefficients are not constant across the tube length. Although transient 1D models remain the standard for chemical reaction engineering issues like controlling the reaction exothermicity, important design features remain obscure for such models, where coolant flow dynamics are simplified [9] or replaced by constant heat transfer coefficients [10].

In our previous work [11], a 3D stationary CFD study was conducted, resulting in a novel reactor design methodology oriented to the upgrade of biogas through CO_2 methanation, Figure 1. CFD simulations were focused on coolant flow dynamics and heat transfer performance in the reactor. Therefore, the reactor's interaction with auxiliary equipment (e.g., compressors, separators) was not considered.
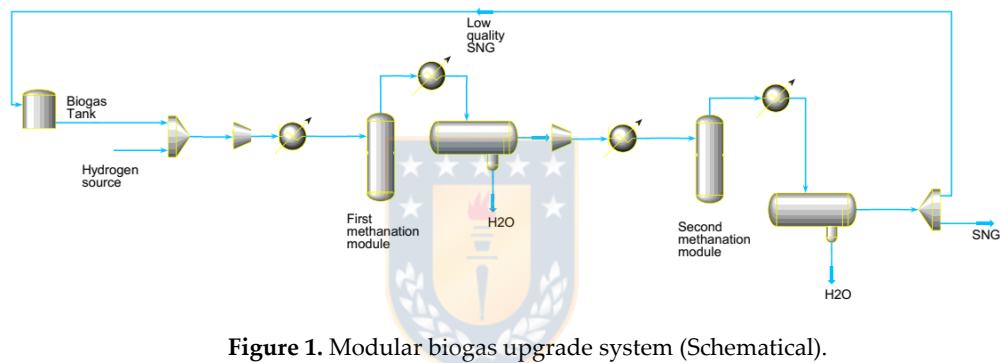

Figure 1. Modular biogas upgrade system (Schematical).

A disk and doughnut arrangement was selected for its advantages over traditional reactor arrangements. Due to the axisymmetric nature of the design, all tubes are subjected to the same flow and thermal conditions. In addition, an optimal baffle disposition allows for an optimal heat transfer performance at the hot spot position due to direct exposure to the incoming coolant stream. Finally, an optimal cooling flow was identified, which minimised the pumping energy requirement while maximising heat transfer in key areas.

To enhance our design methodology incorporating relevant power to gas operational conditions, a novel transient 3D CFD modelling methodology is employed to simulate the effect of relevant dynamic disruptions on the behaviour of a tubular fixed bed reactor for biogas upgrading. The reactor's behaviour was analysed considering the hot-spot temperature and the outlet CH_4 mole fraction as main performance parameters. According to reviewed literature, dynamic operation of fixed bed methanation reactors occurs by disruptions in the inlet temperature [12,13], flow rate [10] and composition [14]. In this work, due to the relevance of composition variation in the power to gas context, a disturbance of H_2 content in the inlet feed was considered, in addition, to temperature changes in the inlet stream. Finally, reactor start-up and shutdown times were determined alongside the maximum idle time (no coolant nor gas flow), which allowed for a warm start (i.e., condition in which the reactor and the coolant temperature allow for the reaction to ignite, without the need to change the design operational conditions substantially). It is expected that the present contribution will be useful for designers and engineers, providing a good reference in the field of biogas upgrade through CO_2 methanation.

2. Materials and Methods

2.1. Reactor Model Description

A twenty-tube fixed bed reactor 3D model for biogas upgrade into SNG (Synthetic Natural Gas) quality was considered as the study object of the present work. Additional parameters and full reactor description can be found in [11]. According to our previous research, two reactor modules of 1 m and 0.5 m and an intermediate condensation step are required to upgrade biogas to a SNG quality gas: 97.8 mol % CH_4, 0.42% CO_2, 1.68% H_2. This considers that the first module attains a product composition (on a dry basis) of: 90.2% CH_4, 2% CO_2 and 7.8% H_2. Feed composition of the biogas stream should comply with the following minimum standard: 64% CH_4, 32.5% CO_2, 2.5% H_2O and no sulphur. In addition, a H_2/CO_2 of 3.8 was adopted due to the difficulty of meeting the minimum H_2 content in the product gas. For the sake of simplicity, only the first module was simulated, considering that the most relevant phenomena occurred in the initial sections of the reactor. Figure 2 show the entire first reactor module as simulated in the present work.

$$r_{CO2} = \frac{kp_{H2}^{0.5}p_{CO2}^{0.5}\left(1 - \frac{p_{CH4}p_{H2O}^2}{p_{CO2}p_{H2}^4 K_{eq}}\right)}{\left(1 + K_{OH}\frac{p_{H2O}}{p_{H2}^{0.5}} + K_{H2}p_{H2}^{0.5} + K_{mix}p_{CO2}^{0.5}\right)^2} \tag{7}$$

$$k_r = k_0 \exp\left[\frac{E_A}{R}\left(\frac{1}{T_{ref}} - \frac{1}{T}\right)\right] \tag{8}$$

$$K_i = K_{0.i} \exp\left[\frac{\Delta H_{ads,i}}{R}\left(\frac{1}{T_{ref}} - \frac{1}{T}\right)\right] \tag{9}$$

$$K_{eq} = 137\, T^{-3.998} \exp\left[\frac{158,700}{RT}\right] \tag{10}$$

CO_2 methanation kinetics Equations (2)–(5) proposed by Koschany et al. [15] was incorporated into the CFD model by means of a UDF written in C language. Kinetic parameters were adopted from [5]. A commercial Ni-based catalyst (923 K maximum operational temperature) [16] was considered. The reactor is assumed to be fully insulated by a 50 mm mineral wool layer. Table 1 summarises the base case operational conditions and reactor technical specifications.

Table 1. Operational conditions and reactor technical specifications.

Parameter	Unit	Value
Reactor dimensions		
Tube outside diameter	mm	25
Tube length (First module)	mm	975
Tube length (Second module)	mm	500
Number of tubes	-	20
Insulation [17]		
Material	-	Mineral wool
Thickness	mm	50
Density	kg/m³	700
Specific Heat	j/kg·K	2310
Thermal conductivity	W/m·K	0.05
Operational parameters		
Biogas flow	Nm³/h	20
Reaction pressure	bar	10
Gas feed temperature	K	523
Cooling temperature	K	523
Catalyst maximum temperature **[16]**	K	923

Coolant flow	m³/h	3.5
GHSV	h^{-1}	3200
Gas flow per tube	Nm³/h	1.5
Feed gas composition		
CH$_4$ inlet mole fraction	mol/mol	0.280
CO$_2$ inlet mole fraction	mol/mol	0.146
H$_2$ inlet mole fraction	mol/mol	0.550
H$_2$O inlet mole fraction	mol/mol	0.015
O$_2$ inlet mole fraction	mol/mol	0.004

The proposed design is modular and suitable for decentralised biogas producing plants ≈ 150 Nm³ (biogas production). Operational conditions (pressure, stoichiometric molar ratio, reaction temperature, reactor dimensions) relates to optimal values determined in our previous work based on the relevant literature review. Table 2 compares our design with previous biogas methanation simulation/experimental works. Only industrial relevant reactors were considered for comparison purposes.

Table 2. Comparison of industrial sized biogas methanation reactors.

Reactor Type	Reactor Tubes Dimensions [DxL]	Biogas/Total Flow [Nm³/h]	Inlet Temperature [K]	Pressure [bar]	X_{CO_2} [%]	Cooling System	Study Type	Comments	Reference
Two stage multi tube packed bed	25 mm × 1 m 25 mm × 0.5 m	20	523	10	91 ≈99	Shell side thermal oil 523 K	Numerical CFD	20 tubes	This work
Multi tube packed bed	45 mm × 4 m	100	473–573	8–40	94–98	Shell side thermal oil 519 K	Numerical	60 tubes	[18]
Multi tube packed bed	20 mm × 8 m	450	476	1	96	Shell side Boiling Water	Numerical	1950 tubes	[19]
Single tube packed bed	200 mm × 1 m	- 382.5	550	5	≈80	Shell-side Molten Salt tubes 600 K	Numerical	13 cooling tubes	[20]
Three step multi tube packed bed with interstage condensation	10 mm × 1.13 m 10 mm × 0.95 m 10 mm × 0.36 m	1612	526 515 513	13.6–13.9	62 91 99.5	Shell side Molten Salt	Optimisation	588 tubes	[21]
Multi tube packed bed	9.25 mm × 250 mm	100	473	5	99	Tube wall set at T = 373 K	Numerical CFD	1000 tubes	[22]
Two stage multi tube packed bed	25 mm × 3.5 m 25 mm × 5 m	200	613–673	7–45	>90	Shell side cooled	Process design	N/A	[23]
Multi tube packed bed	Same as [21]	Same as [21]	442–526	13.4–13.9	Same as [21]	Shell side cooled 500–515	Exergetic analysis	Same as [21]	[24]
Two stage multi tube packed bed	2.3 m length	10	553.15	20	≈100	Boiling water 280 °C-65 bar	Experimental	2 tubes in series	[2]
Four stage multi tube packed bed	50 mm × 4 m	8–16	473.15	15	90	Thermal oil 370 °C	Experimental	4 tubes in series	[3]

Two stage multi tube packed bed	25.4 mm × 3 m	0.4–0.64	500–600	1–15	90–99	-	Numerical thermodynamic	20–24–28	[25]

2.2. Governing Equations

In this work, the unsteady form of the conservation laws of mass, energy and momentum Equations (6)–(13) in addition to the constitutive equations for the turbulence model (shell side), chemical kinetics (tubes), thermal model (tubes) and momentum exchange (tubes) were adapted from the steady-state conservation laws documented in detail in our previous work and detailed in Table 3.

Table 3. Governing equations of the transient CFD model.

Reactive Flow (Tubes)

Gas phase continuity: $\frac{\partial \rho}{\partial t} + \nabla \cdot \left(\varphi \rho_g \vec{v} \right) = 0$ (6)

Gas phase momentum: $\frac{\partial (\rho \vec{v})}{\partial t} + \nabla \cdot \left(\varphi \rho_g \vec{v} \vec{v} \right) = -\varphi \nabla p + \nabla \cdot \left(\varphi \overline{\overline{\tau}} \right) - \vec{S}$ (7)

Gas phase Energy: $\frac{\partial (\rho E)}{\partial t} + \nabla \cdot \left(\vec{v} \left(\rho_g E_g + p \right) \right) = \nabla \cdot \left(\varphi \lambda_\varphi \nabla T_g - \sum_i h_i j_i \right) + S_{h,rxn}$ (8)

Species: $\frac{\partial (\rho Y_i)}{\partial t} + \nabla \cdot \left(\rho_g \vec{v} Y_i \right) = -\nabla \cdot \vec{J_i} + A_f \cdot R_i$ (9),

Coolant flow (shell-side):

Fluid phase continuity: $\frac{\partial \rho}{\partial t} + \nabla \cdot \left(\rho_f \vec{v} \right) = 0$ (10)

Fluid phase momentum: $\frac{\partial (\rho \vec{v})}{\partial t} + \nabla \cdot \left(\rho_f \vec{v} \vec{v} \right) = -\nabla p + \nabla \cdot \left(\overline{\overline{\tau}} \right)$ (11)

Fluid phase energy: $\frac{\partial (\rho E)}{\partial t} + \nabla \cdot \left(\vec{v} \left(\rho_f E_f + p \right) \right) = \nabla \cdot (\lambda_{eff} \nabla T)$ (12)

Baffles & tube walls:

Solid phase energy: $\frac{\partial (\rho E)}{\partial t} + \nabla \cdot (\lambda_{st} \nabla T) = 0$ (13)

2.3. Numerical Methods

The SIMPLE algorithm was applied to couple the pressure and velocity equations. Discretisation schemes for momentum, energy and species were of the second-order upwind, while a standard approach was selected for the pressure equation. The temporal term was discretised with the first-order implicit formulation. The least-squares cell-based scheme was chosen to discretise variable gradients. Under-relaxation factors of 0.6 were considered for momentum and balance equations, while energy and species were set at 0.4. Wall y+ value was monitored for the coolant flow to guarantee standard wall function requirements (y+ > 30) and ensure an accurate approach for heat transfer coefficients estimation on tube walls. In addition, the maximum cell convective Courant number (≈20–40) was monitored inside the reactive tubes to confirm the suitability of the transient formulation (time step and max iterations per time step). A time step of 1 s complies with the convective Courant number requirements; however, in this work, a time step of 0.5 s was used to represent better the transient phenomena. Steady-state was verified through the following relevant variables: CO_2 and CH_4 mole fraction at the tube's outlet and maximum (hot-spot) temperature. Unsteady governing equations were discretised and solved using the CFD code ANSYS Fluent by the finite volume method.

2.4. Physical Models and Boundary Conditions

Figure 2 illustrates the reactor physical model and the implemented boundary conditions. The CFD model comprised three distinct cell zones (domains): (1) coolant (fluid), (2) tubes (porous media) and (3) baffles (solid). For a detailed description of the thermophysical properties in each cell zone, refer to Appendix A. A velocity inlet (4) of 0.5 m/s was utilised for the coolant inlet, equivalent to 3.5 m³/h of coolant flow at 523 K. Gas feed at tube inlets (5) was characterised by a mass flow inlet of 2.15 × 10⁻⁴ kg/s (≈30 Nm³/h). In order to calculate the pressure drop across reactive tubes and shell sides, a zero

static pressure condition was set at both outlets, tubes (6) and coolant (7). In addition, operating pressure was set at 1 and 10 bar for coolant and reactive tubes, respectively. Heat transfer surfaces (tube to coolant, baffle to coolant) were defined through thermal coupled walls (8). The reactor is assumed to be fully encapsulated in mineral wool insulation. A convective heat transfer coefficient of 5 $W \cdot m^2 \cdot K^{-1}$ [26] and a free stream temperature of 300 K to simulate heat loss to the environment were adopted at the reactor outer walls (9). Table 4 summarises the boundary and cell zone conditions used to set the CFD model.
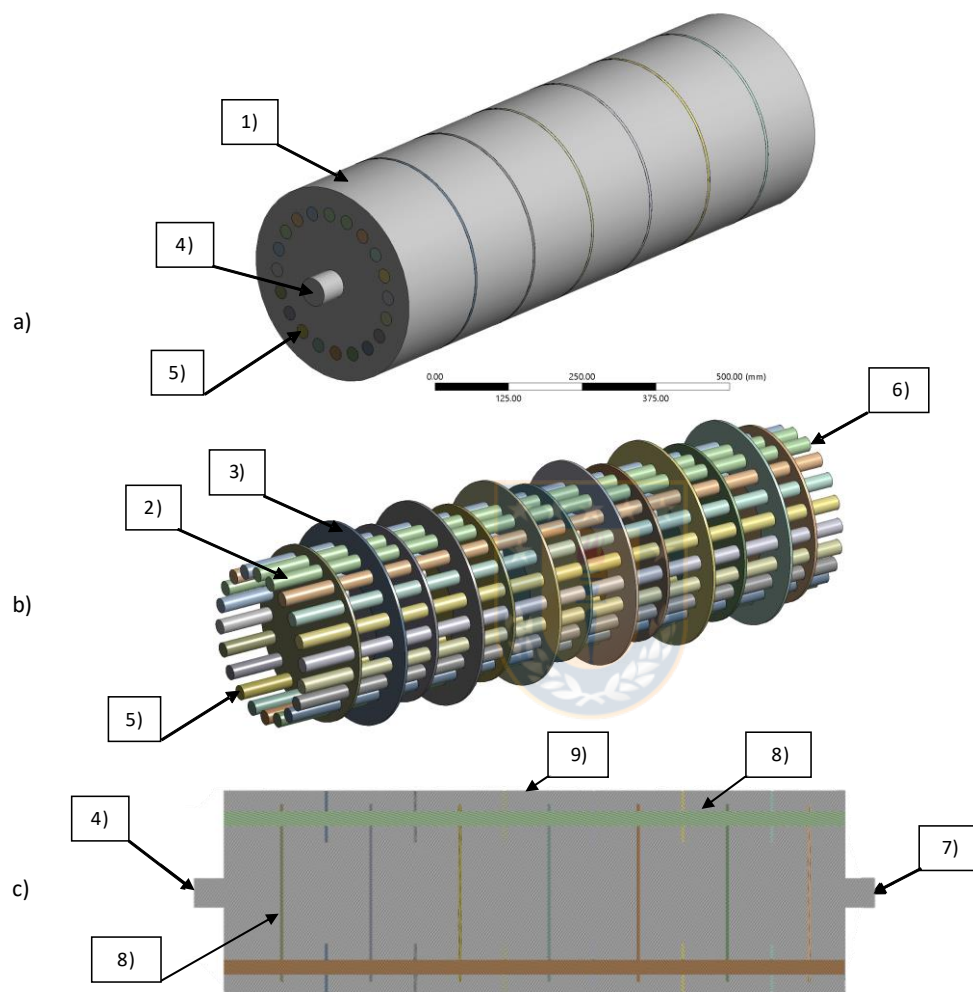
Figure 2. Physical domain and boundary conditions of the CFD model. (a) Full domain. (b) Tubes and baffle domains (porous media and solid). (c) Longitudinal cut view at plane YZ. 1) Coolant (fluid domain). 2) Tubes (porous media domain). 3) Baffles (solid domain). 4) Velocity inlet at coolant domain. 5) Mass flow inlet at porous media domain. 6) Tubes pressure outlet. 7) Coolant domain pressure outlet. 8) Thermal coupled walls at tubes to coolant and baffle to coolant interfaces. 9) Convective heat transfer coefficient at external walls.

Table 4. Boundary and cell zone conditions.

Condition	Unit	Value	Cell Zone
Velocity inlet	m/s	0.5	Coolant
Pressure (static) outlet	Pa	0	Coolant
Convective heat transfer coefficient	$W \cdot m^2 \cdot K^{-1}$	5	Coolant
Free stream temperature	K	300	Coolant

Thermal coupled wall	-	-	Interface Coolant/Tubes
Mass flow inlet	kg/s	2.15×10^{-4}	Tubes
Pressure outlet	Pa	0	Tubes
Operating pressure (coolant)	Pa	1.013×10^{5}	Coolant
Operating pressure (tubes)	Pa	1.013×10^{6}	Tubes
Symmetry (tubes inlet/outlet)	-	-	Tubes (stand by simulation)
Symmetry (coolant inlet/outlet)	-	-	Coolant (stand by simulation)

2.5. Meshing Approach

Figure 3 illustrates the reactor mesh across all sub-domains. Ansys Design Modeller and Ansys Meshing were used for domain and mesh preparation in this work. A non-conformal dual meshing approach was adopted. A tetrahedral mesh (1) was chosen for the coolant (fluid) domain due to its capacity to easily conform to restrictive geometries. According to standard wall function requirements, inflation layers were created (2) at coolant-tube walls to guarantee a Y+ value of 30. A hexahedral grid (3) was used on all tubes (porous media domain) to maximise mesh quality in areas where a chemical reaction occurs. A coarser hexahedral mesh was considered in both disk (4) and doughnut (5) types regarding solid baffles. Non-conformal interface zones were created to connect thermally coupled zones (i.e., when solid (6) and porous media (7) cell zones match the fluid domain). Table 5 summarises mesh quality details for each reactor's model sub-domains. Our previous work checked Mesh independence by calculating the average temperature at the tube's outlet and the average CO_2 mole fraction at the tube's outlet under a steady state.

Table 5. Mesh details.

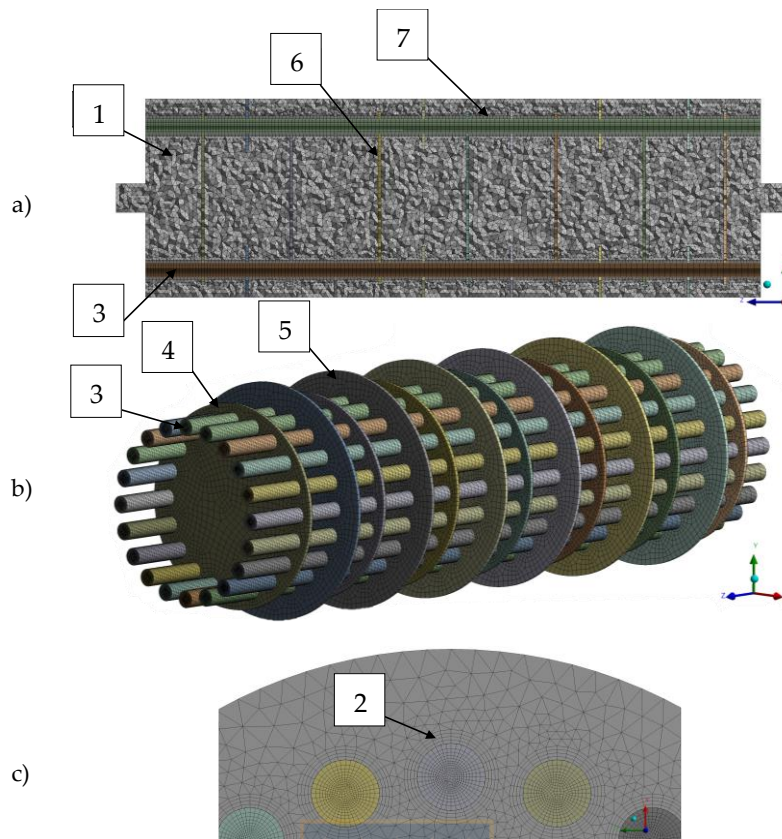| Sub-Domain	Nodes	Elements	Average Skewness	Average Aspect Ratio	Average Orthogonal Quality
Fluid	750,818	2,406,886	0.34141	3.0043	0.65751
Tubes (×20)	1,262,360	1,191,000	0.11051	8.3040	0.98924
Doughnut Baffles (×6)	21,564	9150	0.18852	1.5399	0.96949
Disk Baffles (×6)	21,168	9054	0.18358	1.5027	0.97285
Total	2,055,910	3,616,090	0.27069	4.4693	0.76151

Figure 3. Model mesh.(**a**) All domains; (**b**) Tubes and baffles sub-domains; (**c**) Tubes inlet detail. 1) Tetrahedral mesh in coolant domain. 2) Inflation layers detail at tubes wall. 3) Hexahedral mesh in tube domains. 4) Hexahedral mesh at Disk type baffle. 5) Hexahedral mesh at Doughnut type baffle. 6) and 7) Non-conformal interface zones, between coolant and tubes/baffles domains.

2.6. CFD Model Validation

The present 3D CFD model was validated in a twofold manner in our previous work [11]. First, the chemical reaction model was validated against steady-state experimental data from [16], considering a CO_2 methanation reactor of similar size (1 m in length, 30 mm in diameter). Secondly, the Gnielinski correlation [27] was used to validate the heat transfer coefficients for the tube to coolant interface. Benchmark simulation results agreed well with both experimental and correlation data. The hot spot position was accurately predicted with a 5% error in the axial coordinate. The predicted axial temperature profile showed a maximum error of 8.5% against experimental data, while numerically calculated heat transfer coefficients revealed a maximum deviation of 20% against the Gnielinski correlation. We used the same geometrical configuration and mesh from our previous work in this work. In addition, the optimal operational conditions found in [11] were adopted as the basis for all the transient simulations performed in the present work. Thus, preserving the validity of chemical kinetics and heat transfer models.

2.7. Reactor Dynamic Operation

In this work, dynamic simulations were conducted to characterise three relevant scenarios. Firstly, start-up and shutdown times were determined under nominal conditions. Secondly, the reactor was subjected to relevant dynamic disruptions, namely H_2 feed interruption and changes in the inlet temperature. Finally, the maximum reactor "standby time" (no coolant and gas feed), which allows for a warm start, was determined.

2.7.1. Start-Up and Shutdown

Firstly, a "only biogas run" was performed, where no H_2 was injected so that the flow field inside tubes (only biogas) and coolant side becomes uniform (non-reactive steady-state). In a second step, H_2 injection begins until an ignited steady state is reached (reactor start-up). This start-up operation is characterised by the operational conditions detailed in Table 1. Since the feed is rich in methane, no additional measures (e.g., catalyst dilution) for thermal control were considered. Finally, the reactor shutdown is simulated, interrupting the H_2 feed while maintaining the flow of biogas at operational temperature. The simulation sequence summarises as follows:

1. **Non-reactive steady state:** Biogas and coolant under nominal operational conditions are injected until a fully developed flow is attained. A steady-state simulation was conducted to simulate the abovementioned flow and used as an initial condition in further transient studies.
2. **Reactor start-up:** As H_2 supply begins, reactor steady state was checked by monitoring the following variables: average CO_2 mole fraction, maximum temperature, average temperature and CH_4 mole fraction at the tube outlet. A change of less than 1×10^{-4} for all monitored variables in two successive time steps was considered as proof of steady-state condition.
3. **Reactor shutdown:** As a steady state was reached, H_2 supply was interrupted. Pure biogas (at 523 K) was fed to the reactor until the average tube temperature matched the coolant temperature (523 K). The average gas composition inside tubes reached that of pure biogas. Biogas is assumed to be continuously recirculated to the bio-digestor under reactor shutdown operation.

2.7.2. Dynamic Disruptions

As mentioned, the impact of dynamic disruptions on the reactor was numerically simulated through inlet composition and temperature disruptions. After a steady state was attained, the H_2 supply was interrupted. Then, pure biogas (at reaction temperature) was injected into the reactor for 30 s (according to the European Union guidelines for electricity transmission [28], in case of frequency disruption in the grid, the transmission system operators (TSO) shall restore the reference value at the latest after 30 s. Therefore a 30 s H_2 feed interruption was considered to depict a relevant electricity supply disruption) while preserving the GHSV (same superficial velocity). Then H_2 injection is resumed. On the other hand, temperature perturbations were considered through a ±20 K variation in the feed gas. Special attention is given to temperature disruptions due to their relevance in triggering "Wrong Way" behaviour [12]. All simulations were conducted until steady state conditions were observed.

2.7.3. Stand by Reactor

To determine the maximum "standby" of a non-feed and non-coolant flow condition, the reactor cooling process was simulated in the absence of heating sources. After the reactor shutdown, both coolant and biogas inflows are interrupted. This simulation aimed to determine the maximum reactor idle time, allowing for the reactor's resumption (warm start) with no necessity of heating the inflow gases beyond the optimal temperature (523 K).

3. Results and Discussion

3.1. Reactor Start-Up and Shutdown Simulation

First, the reactor model simulates the start-up process as detailed in Section 2.7.1. In this study, CFD simulations were oriented towards identifying temperature contours in the hot spot affected area since it strongly influences the reactor operational flexibility. Additionally, the CH_4 mole fraction at the reactor outlet was given special attention for its relevance to the product gas quality. Progress towards the steady state was simulated considering nominal operational conditions of the reactor. At t = 0 s, reactor feed is adjusted from pure biogas to a mixture of biogas and H_2, preserving a stoichiometric ratio of 3.8. The volumetric flow remains constant in both conditions (same GHSV). According to Figure 4a) the reactor needs 70 s to reach the maximum temperature after H_2 injection. A steady-state hot spot is observed after 330 s from H_2 injection. A maximum temperature of 879 K is reached, which means

that it is possible to maintain a safe and stable start-up operation in the reactor under the considered operational conditions without diluting the catalytic bed or the addition of complex cooling and control systems. During this transient operation, it is assumed that no flow is directed to the second methanation module. Shutdown operation was also simulated, and the reactor thermal behaviour was characterised. After the reactor reaches the steady state (330 s), H_2 feed is interrupted, and pure biogas (523 K) injection is resumed. The reactor assumes a "non-reactive" flow mode aimed at maintaining warm start conditions in the absence of chemical reaction.

Figure 5 illustrates the temperature contours in the characteristic reactor tube at different time series: 10 s, 20 s, 40 s, 330 s. As typical in exothermic reactions, a distinct hot spot appears at the reactor's inlet. High reactant concentration results in higher reaction rates and large temperature gradients. A fully developed hot spot is observed at 330 s. Due to heat removal and viscosity effects, a large temperature gradient (≈200 K) exists radially at the hot spot. Downstream to the hot-spot affected area, a low-temperature zone appears, where the reactor matches the coolant temperature (523 K). As it is common in fixed bed reactors, it should be noted that most of the extent of reaction takes place in the first ≈250 mm of the reactor's first module. As already mentioned in our previous work, the extent of reaction is mostly driven by kinetic effects in this section. Downstream, it becomes increasingly difficult to reach higher conversions unless the thermodynamic equilibrium is shifted back to products (e.g., water removal). As detailed in our previous work, interstage water removal becomes mandatory to achieve the required SNG quality. As Figure 4b) shows, after ≈130 s of hydrogen feed interruption, the hot spot affected area cools down to the ignition temperature. From the CFD simulations, it can be concluded that nearly six minutes (330 s) are needed for the reactor's first module to reach a steady state (start-up operation). In contrast, the reactor's first module requires two minutes to attain warm start conditions after H_2 is interrupted (shutdown operation). Reported start-up times in similar simulation and experimental works range in the minutes for all cases. Bremer [29] reported 1000 s to reach a steady state for a 20 mm × 5 m, 720 h^{-1} GHSV tubular reactor. Fache [30] determined optimal operational variables for a multi-tubular reactor with staged dilution. An optimal start-up time of 178 s was found for a total flow of 0.44 m³/h per reactor tube. Matthischke [5] determined the start-up times for an adiabatic and a cooled tubular reactor. The latter needed 200 s to attain a steady temperature profile while the former required 400 s. Dannesboe [25] developed a pilot plant scale double pass reactor with boiling water cooling for a 10 Nm³/h biogas flow. Steady state operation, with respect to the temperature profile, was achieved after 25 min. Giglio [6] proposed a three-staged methanation unit with two water removal steps. A product gas with a 95% methane content was obtained after 130 s from a warm start.
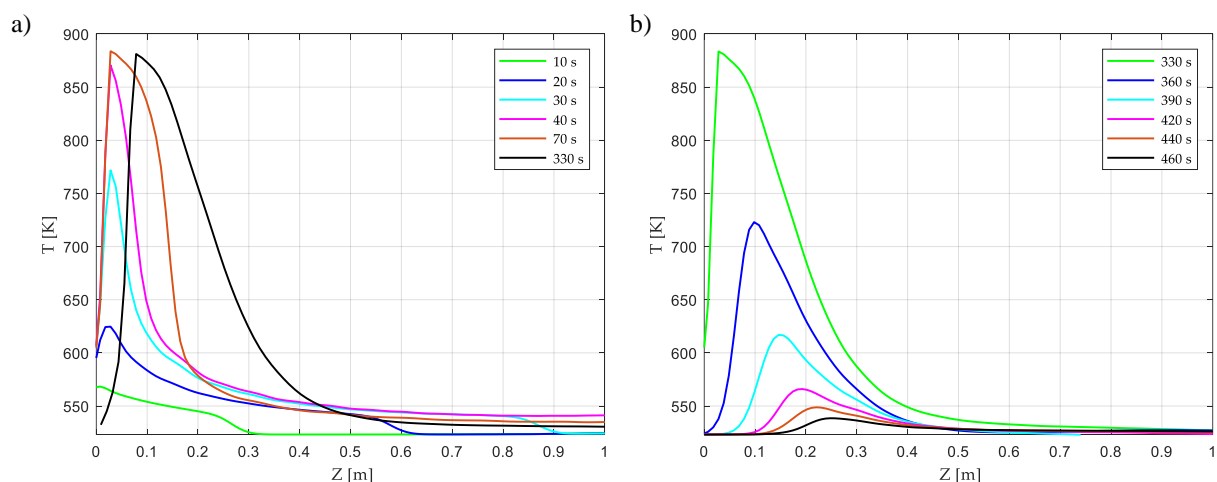

Figure 4. Transient axial temperature profiles inside reactor tubes for: (**a**) Start-up and (**b**) Shutdown operation. Steady state reached after 330 s (**a**), and reactor Shutdown reached after 130 s of H_2 feed interruption (**b**).
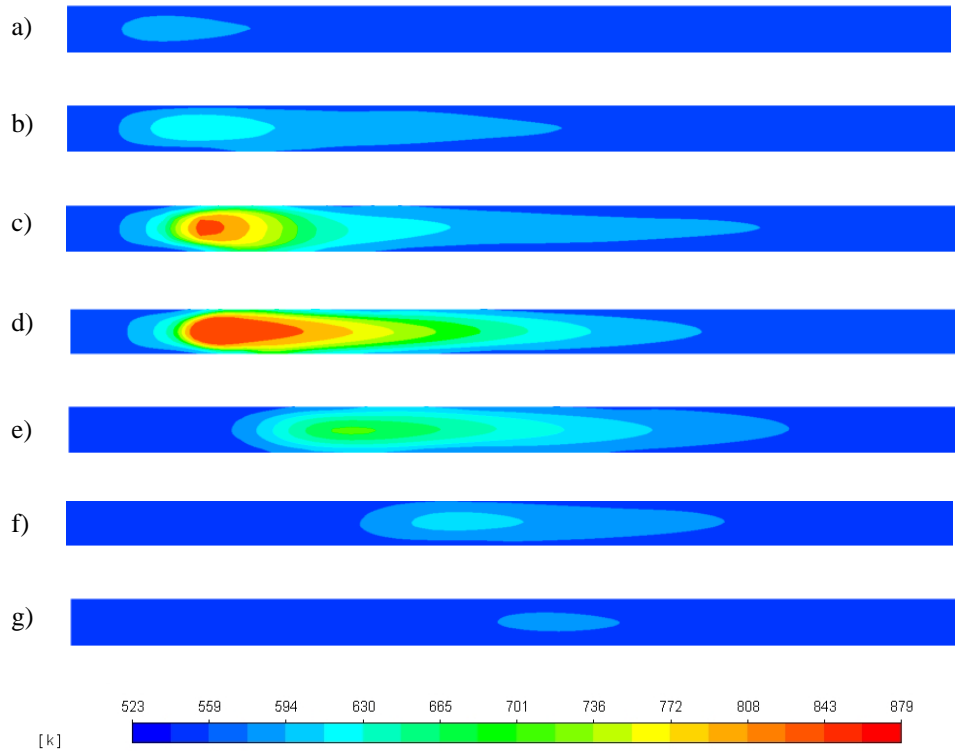
Figure 5. Temperature contours in the hot-spot relevant zone (First 500 mm of reactor tube length) for: Start-up operation: (**a**) 10 s, (**b**) 20 s, (**c**) 40 s, (**d**) 330 s and Shut-down operation: (**e**) 365 s, (**f**) 405 s, (**g**) 460 s.

3.2. Reactor Response to H_2 Feed Interruption

The first disturbance was simulated as a step-change in the inlet gas composition due to a sudden loss of the H_2 feed from the electrolyser for 30 s. The reactor response was followed from this reference state, t = 360 s (330 s "steady state" +30 s interruption) to the recovery of steady-state behaviour after 450 s from the reactor's start-up. Figure 6a represents the reactor temperature contours after 30 s the H_2 feed was disrupted. Due to the cooling effect of the inlet biogas stream and the absence of H_2, the original hot spot dissipates, but a high-temperature zone persists downwards. As H_2 feed resumes, a new hot spot begins to form downwards, at t ≈ 375 s Figure 7, due to the displacement of the maximum temperature zone, Figure 6b.

As a new hot-spot forms, the temperature rises near the reactor inlet, Figure 6c prompting the resurgence of the original hot spot after t ≈ 410, Figure 6d. As the temperature progressively increases, the reaction front moves forward until the hot spot is fully formed 90 s after the H_2 feed was interrupted. This behaviour can be explained as follows: after 30 s of H_2 feed interruption and biogas injection, an area downwards of the original hot spot position is not cooled enough during the 30 s of biogas injection, preserving a high-temperature zone (642–682 K) Figure 6a, due to the catalytic bed thermal inertia. As H_2 injection is resumed, the concentration front reaches this high-temperature surface, triggering a transient hot spot similarly as observed by Try et al. [12]. As more reactants convert to CH_4 in this area, fewer reactants become available downwards to sustain this hot spot. Consequently, the reaction front moves upwards, where a higher concentration of reactants allows for higher reaction rates and temperature. As fewer reactants reach the downstream part of the reactor, the transient hot spot, Figure 6b, dissipates. According to Figure 7, a step disruption of the H_2 feed impacts the outlet CH_4 composition during 90 s, i.e., (from t = 360 s to t = 450 s).

At t = 450, the steady state CH_4 outlet mole composition stabilises around 0.55, allowing for the fulfilment of SNG quality requirements (90.2% CH_4 on a dry basis after the first methanation module).

At the same time, the low-temperature transient hot spot is entirely replaced by a high-temperature one after the 450 s (90 s after H_2 resumption).
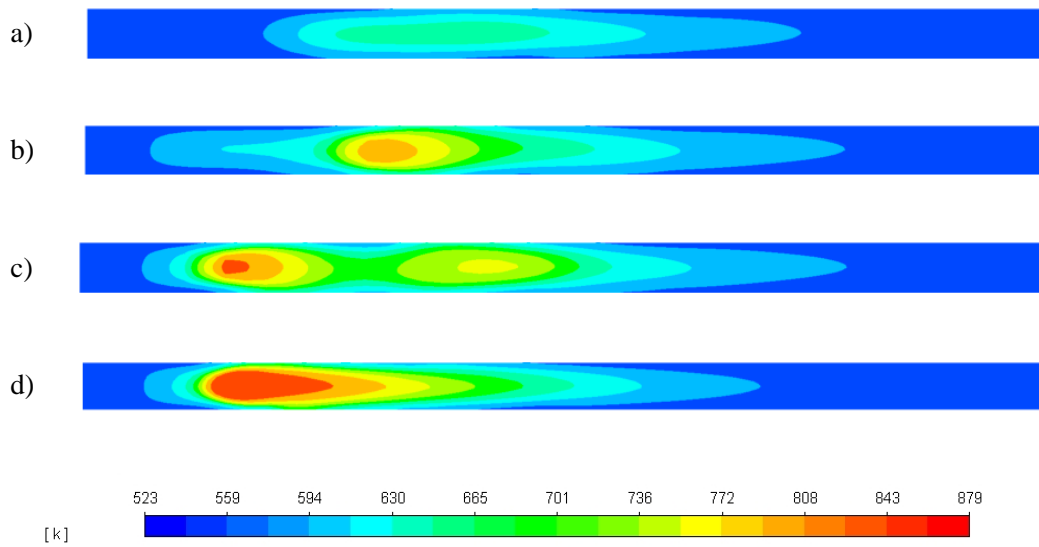

Figure 6. Temperature contours in the hot-spot relevant zone after a 30 s H_2 feed disruption at t: (**a**) 360 s, (**b**) 380 s, (**c**) 400 s, (**d**) 450 s.
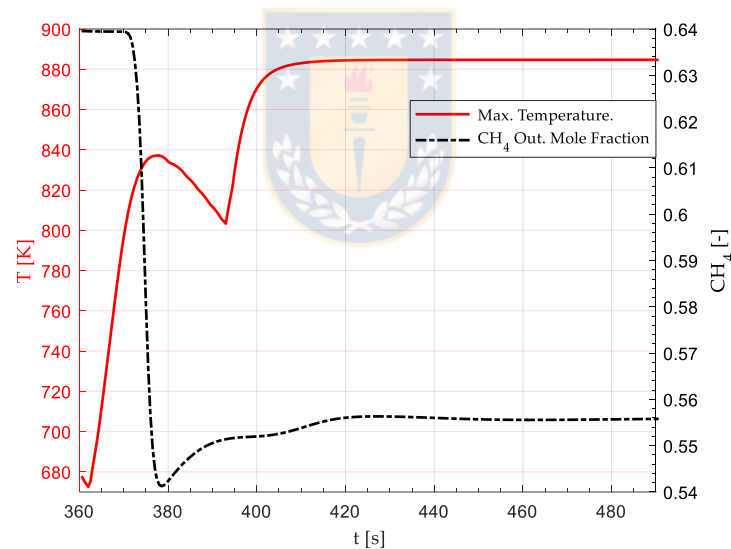

Figure 7. Effect of a 30 s H_2 feed disruption on the methane mole fraction at reactor outlet and the maximum reactor temperature. H_2 feed disruption occurs from 330 s to 360 s (from reactor standby). At 360 s, H_2 feed is resumed. The original steady state is completely recovered at t = 450 s.

3.3. Reactor Response to Temperature Disruptions

3.3.1. 20 K Feed Temperature Rise

Figure 8 shows the temperature contours of the reactor subjected to a 20 K step-rise in the feed gas temperature (523 K–543 K). Figure 9 shows the transient response of the hot spot temperature and the CH_4 mole fraction at the reactor's outlet, respectively. The inlet temperature rise triggered a transient drop in the reactor hot spot temperature from t = 0 to t = 25, Figure 9. Similar behaviour was observed by Li et al. [13] for a sudden temperature rise (523 K to 543 K) in an adiabatic CO methanation reactor. Higher upstream temperatures prompted higher reaction rates and CO_2 consumption near the reactor inlet, Figure 10. As the concentration front moves upwards, Figure 10 shows fewer reactants remain

available downstream. Consequently, the reactor undergoes a transient drop in the maximum temperature, Figure 8a,b. At approximately t = 25 s from the disruption, in Figure 9, the hot spot attains its minimum temperature (850 K), after which it begins to rise until it reaches 892 K at t = 40 s Figure 9. After 120 s, a new steady state becomes apparent by a new maximum temperature (892 K up from 879 K) Figure 9, and the stabilisation of the concentration front upwards, Figure 10c. Regarding the CH_4 formation, Figure 9, this disruption does not significantly affect the minimum outlet mole fraction required to fulfil SNG quality (>0.55). Although the hot spot moved upwards from the optimal design position (i.e., between the inlet and the first baffle), it remained in the maximum heat transfer area due to exposure to the incoming coolant stream at high velocity directly from the inlet, Figure 11.
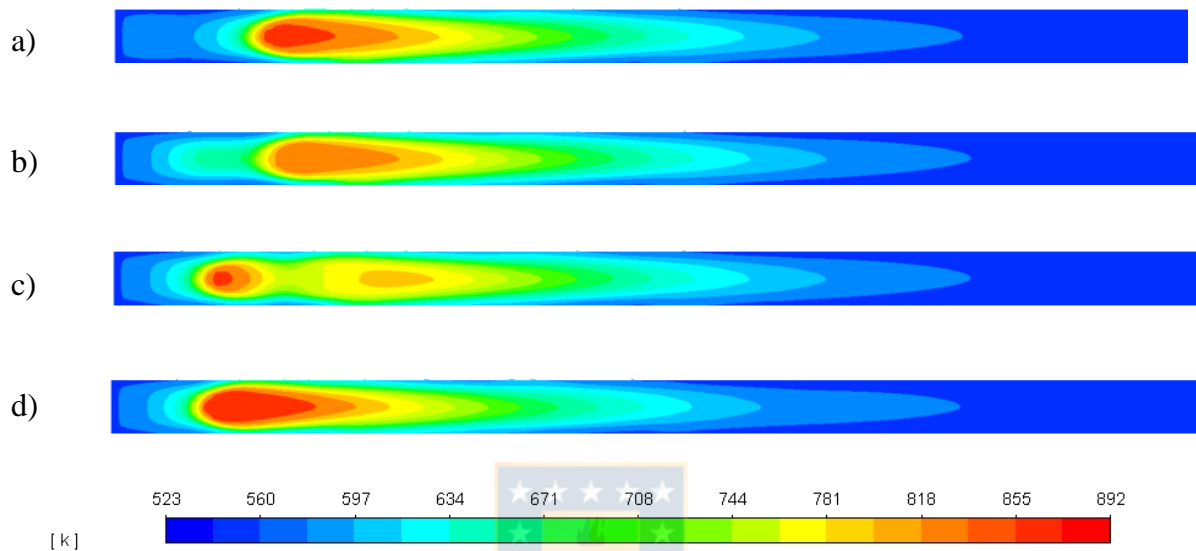
Figure 8. Temperature contours in the hot-spot relevant zone after a 20 K step-rise in the feed gas (523 K to 543 K) at t = (**a**) 10 s, (**b**) 20 s, (**c**) 30 s, (**d**) 120 s from disruption.

Figure 9. Effect of a 20 K step-rise in the feed gas (523 K to 543 K) on the maximum (Hot Spot) reactor temperature and CH_4 average outlet mole fraction. The disruption begins at t = 0, and a new steady state is established after t ≈ 120 s.
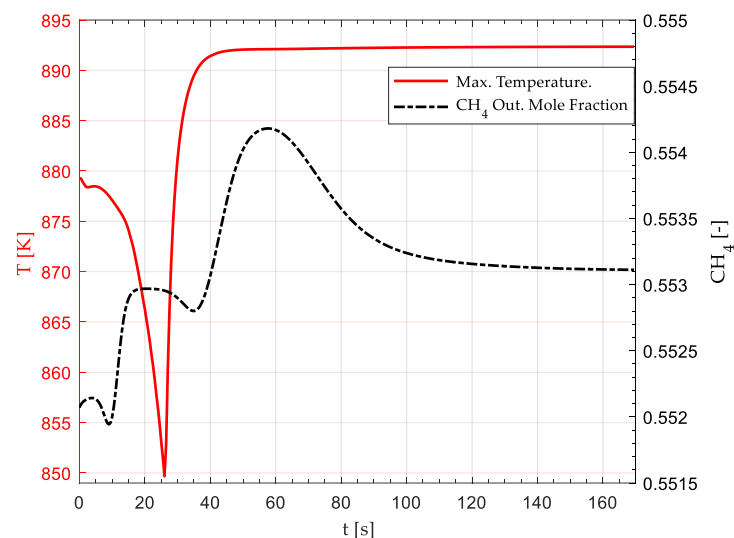
Figure 10. CO_2 mole fraction contours in the hot-spot (First 250 mm of reactor tube length) after a 20 K step-rise in the feed gas (523 K to 543 K) at t = (**a**) 0 s, (**b**) 10 s, (**c**) 30 s from disruption. The concentration front successively moves upwards due to the effect of larger reaction rates near the inlet.
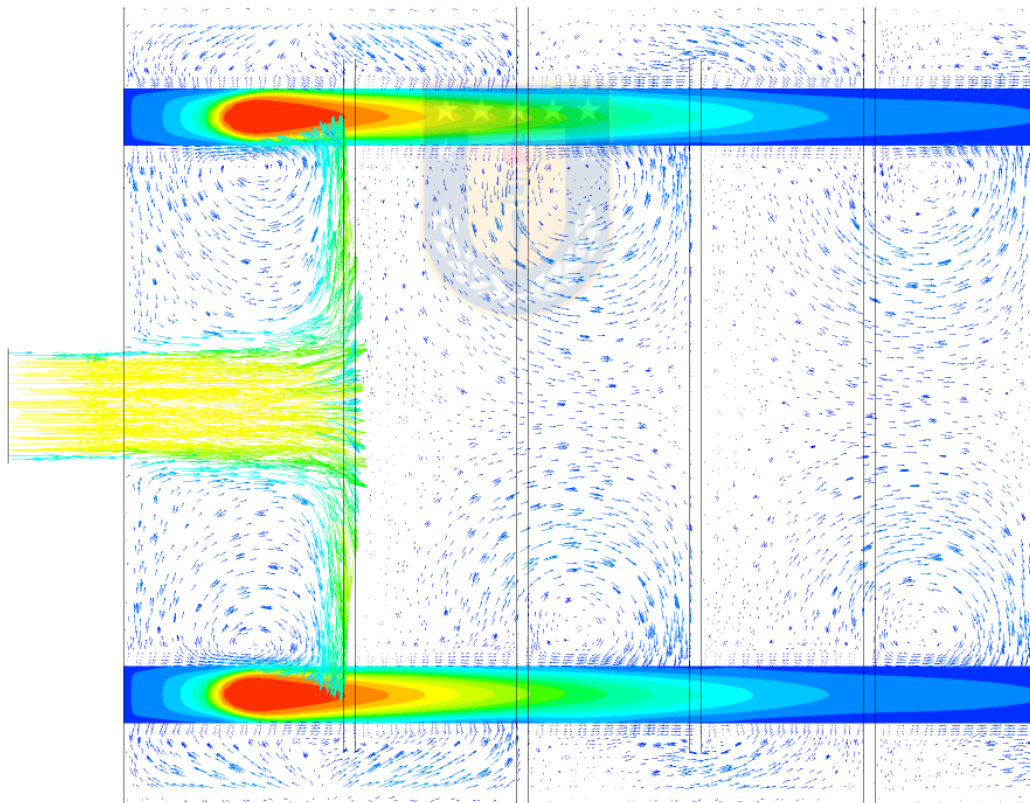
Figure 11. Effect of 20 K inlet temperature rise on the reactor. Hot-spot position and coolant velocity overlay field at t = 120 s.

3.3.2. 20 K Feed Temperature Drop

Figure 12 shows the temperature contours of the reactor subjected to a 20 K step-drop in the feed gas temperature (523 K–503 K). In contrast, Figure 13 shows the transient response of the hot spot temperature and the CH_4 mole fraction at the reactor's outlet, respectively. A transient hot spot of 923 K begins to appear after 20 s, Figure 12b and it is completely formed at 35 s, Figure 12c. The observed

wrong way behaviour can be explained in accordance with the works of [12,13]. As the temperature diminishes in the upstream section of the reactor, the reaction rate diminishes accordingly, prompting a successive increment in the CO_2 concentration near the inlet due to the movement of the reaction front towards the outlet, Figure 14. Owing to the bed's thermal inertia, the incoming gas stream at a lower temperature (503 K) cannot cool the bed quickly enough. Therefore, the high bed temperature and the increasing reactant concentration trigger a transient "high temperature" hot spot between t = 0 s to t = 35 s, Figure 13. This transient hot spot surpassed the maximum steady-state temperature by 43 K (880 K to 923 K), exposing the reactor to its maximum operational temperature (923 K). A new steady state is attained after 200 s the disruption occurs, characterised by an 872 K hot spot Figure 12e. Finally, the wrong-way behaviour tends to disappear as the concentration front stabilises around its final position, Figure 14c, from t = 40 s onwards, Figure 13. As in Section 3.3.1, the CH_4 average outlet mole fraction, Figure 13, remains under acceptable ranges to fulfil the required SNG quality (>0.55). As the hot spot moved downwards from the optimal design position (i.e., between the inlet and the first baffle), a loss in cooling effectivity occurs due to the displacement out of the optimal cooling zone, Figure 15. In this case, the high-temperature hot spot may be attributed partially to this loss of cooling effectivity during the hot spot transition.
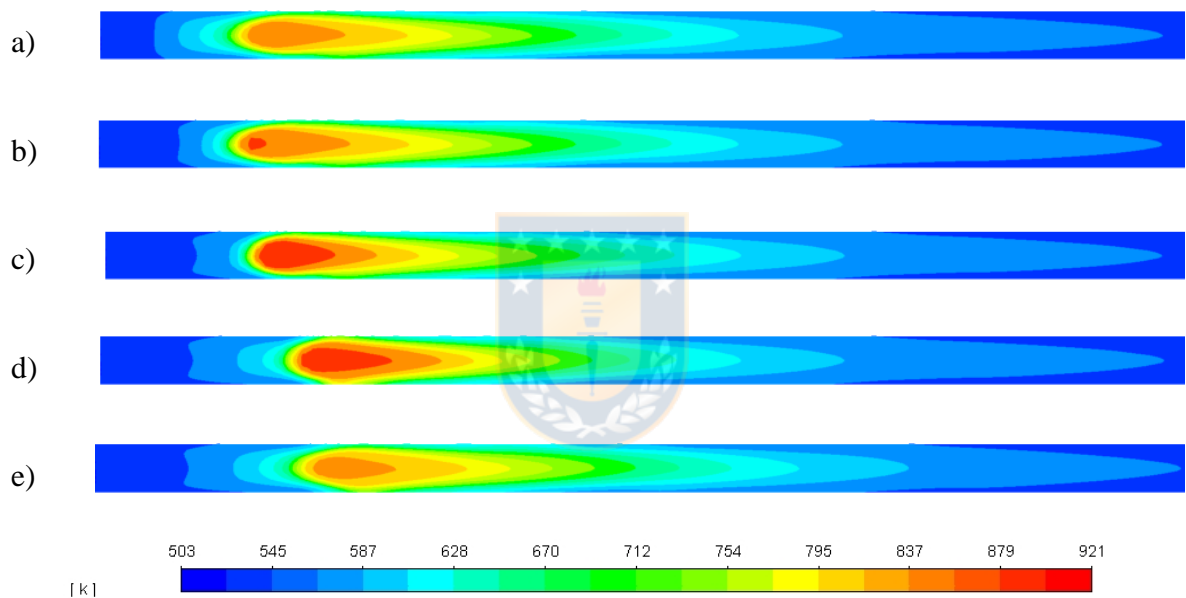
Figure 12. Temperature contours in the hot-spot relevant zone after a 20 K step-drop in the feed gas (523 K to 503 K) at t = (**a**) 10 s, (**b**) 20 s, (**c**) 30 s, (**d**) 60 s, (**e**) 200 s from the disruption.
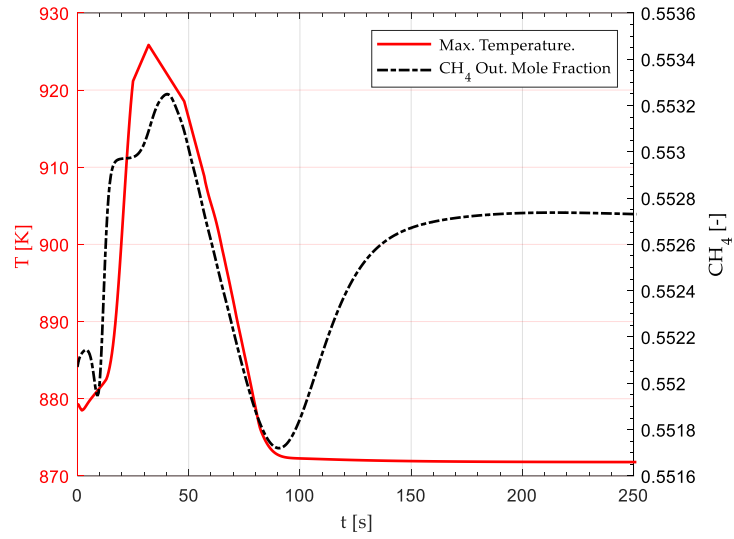
Figure 13. Effect of a 20 K step-drop in the feed gas (523 K to 503 K) on the maximum (Hot Spot) reactor temperature and CH_4 average outlet mole fraction. The disruption begins at t = 0, and a new steady state is established after t ≈ 200 s.

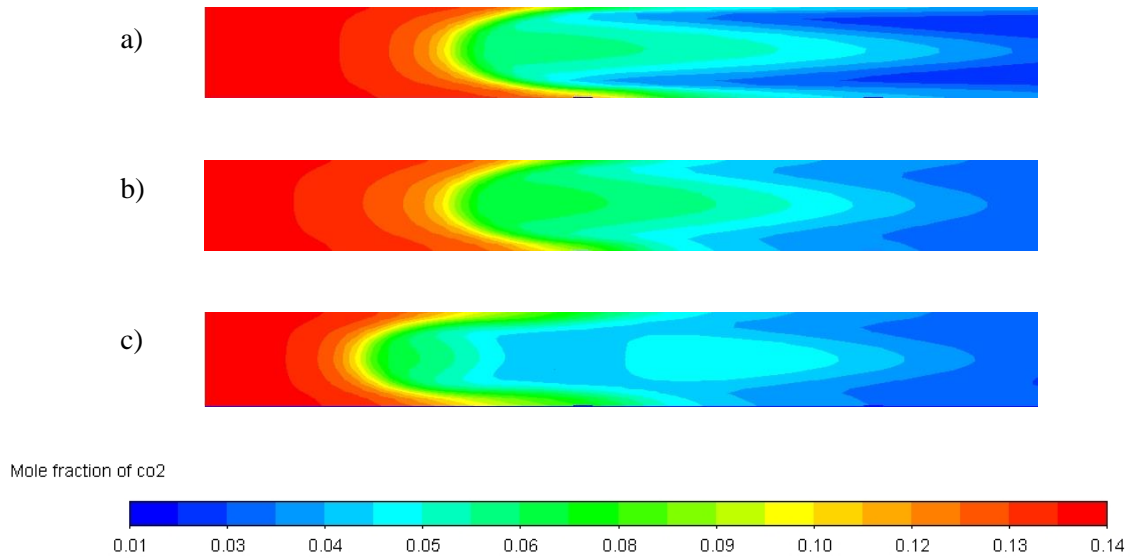**Figure 14.** CO_2 mole fraction contours in the hot-spot (First 250 mm of reactor tube length) after a 20 K step-drop in the feed gas (523 K to 503 K) at t = (**a**) 10 s, (**b**) 20 s, (**c**) 40 s from disruption. The concentration f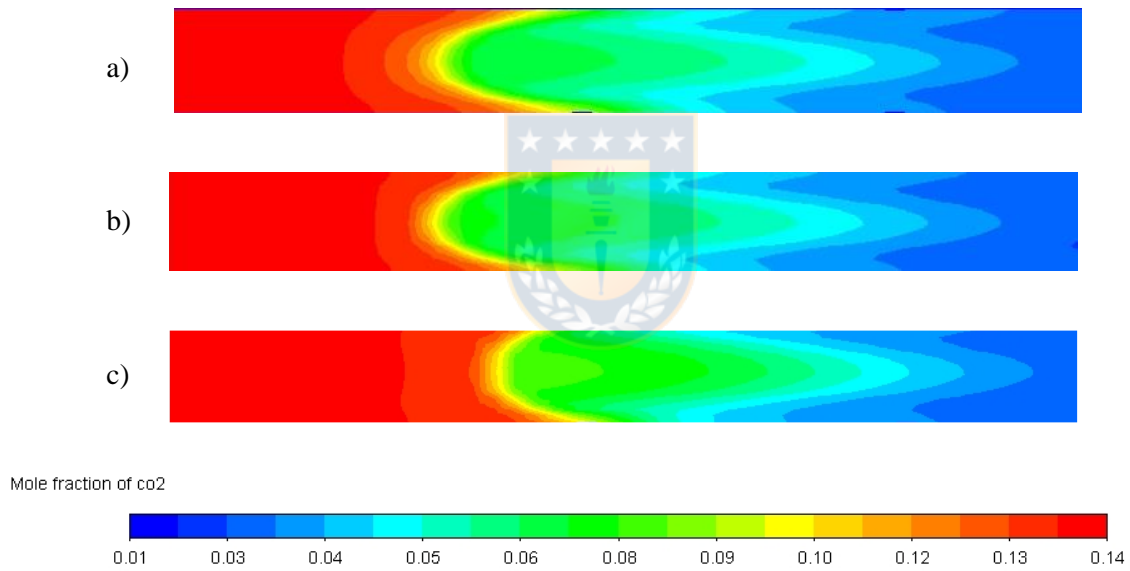ront successively moves downwards due to lower reaction rates near the inlet. A maximum concentration gradient is observed in c), which coincides with the maximum temperature in Figure 12a.
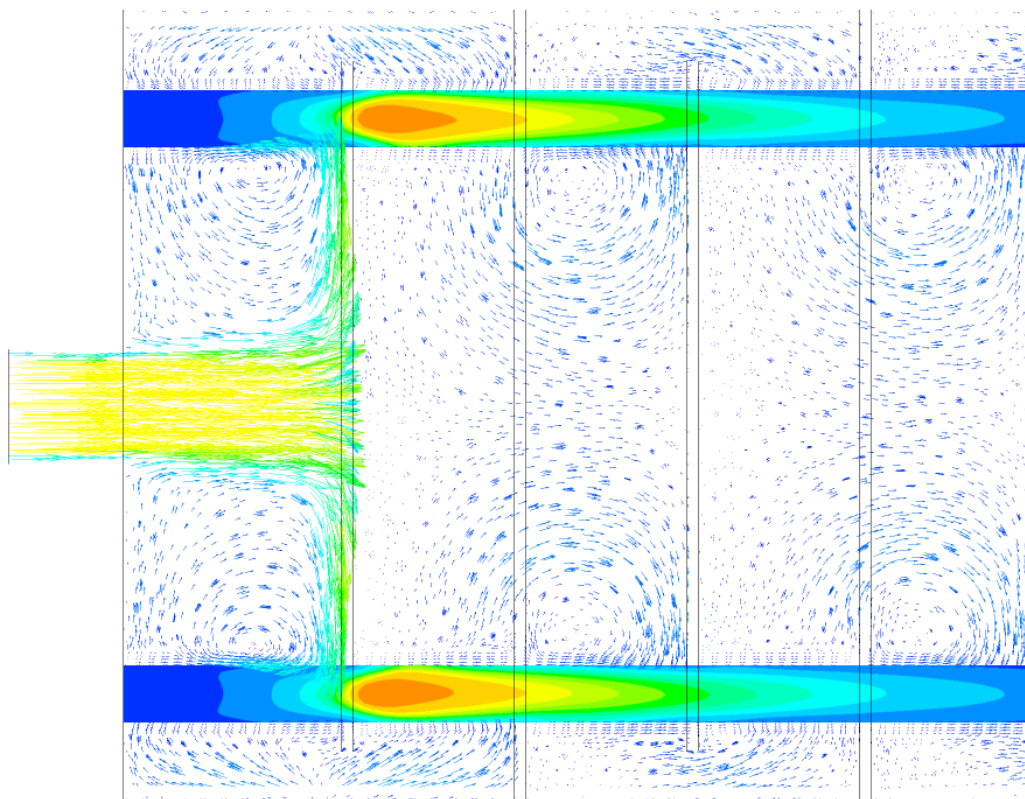
Figure 15. Effect of 20 K inlet temperature drop on the reactor. Hot-spot position and coolant velocity overlay field at t = 200 s.

3.4. Stand by Reactor Simulation

Figure 14a–c shows the YZ plane temperature contours of the reactor in standby mode after one, three, and five hours, respectively, as all external and internal heat sources were suspended (no coolant, gas flow, or reaction heat). As expected, temperature reduction is more significant in the non-insulated areas (coolant inlet and outlets) and in the reactor corners, where two heat transfer fronts exist. Due to the high thermal conductivity of the reactor baffles, a thermal bridge effect is observed from the reactor centreline to the surroundings, where the doughnut type baffle comes in contact with both the surroundings (1) and the inner section of the reactor (2). After five hours of idle time, catalytic tubes zones in contact with doughnut baffles tend to be at a lower temperature than the surroundings (3).

According to Figure 16a, after one hour of idle time, the reactor preserves a temperature of 523 K in the catalytic tubes, allowing for a warm start under optimal conditions. After three hours, the catalytic tubes mostly hold a temperature over 516 K, except in the zones where a thermal bridge exists. At this temperature, a warm start is still possible without the necessity to heat the reactants beyond 523 K or the reactor again up to 523 K. Finally, after five hours of idle time, a minimum temperature of 500 K is observed in the catalytic tubes inlets/outlets and the areas affected by thermal bridges. Although possible, a reactor warm-start is not desirable since the start-up time of the reactor will be raised, and operational parameters like CO_2 conversion will be affected due to lower reaction rates, leading to a lower quality product gas. As an alternative, further heating of reactants is possible to enhance the reaction rate in low-temperature zones. However, this would demand additional control routines to keep the original operational conditions. Therefore, a maximum of 3 h of idle time is possible to allow the optimal ignition of the reactor (warm-start conditions).
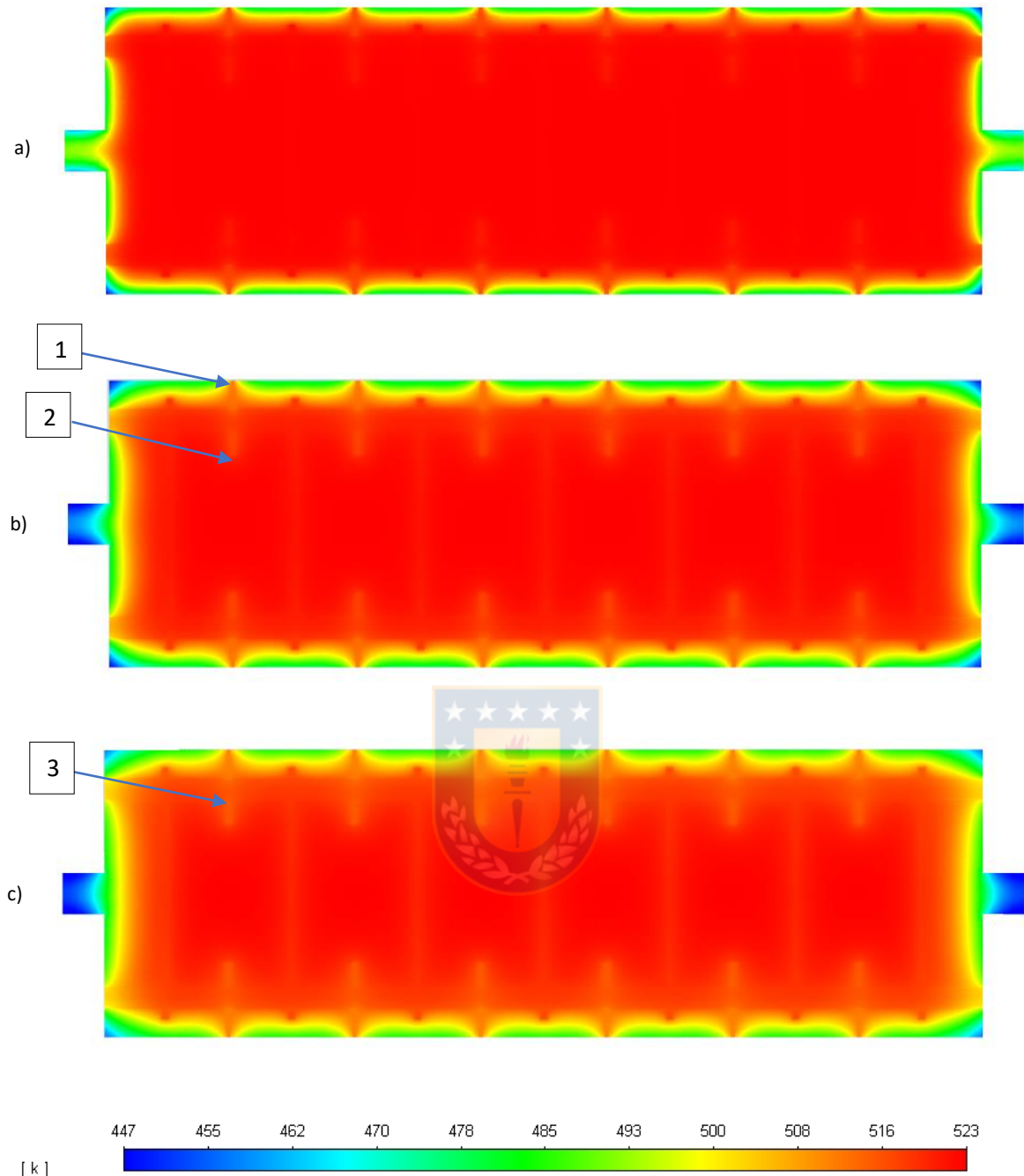
Figure 16. Reactor YZ plane temperature contours after (**a**) one, (**b**) three, and (**c**) five hours of no coolant/gas flow.

4. Conclusions

A 3D fixed bed methanation model was evaluated under dynamic disruptions in this work. The main aim was to enhance our 3D methanation reactor design methodology by incorporating relevant power to methane operational elements. Firstly, the required start-up and shutdown times were determined. As a second step, dynamic perturbations were simulated through a 30 s H_2 feed disruption and ±20 K temperature variation in the gas feed. Finally, the maximum idle time (no coolant or gas flow) was determined, which would allow a warm start without the need to alter the nominal operational conditions.

The reactor reached a steady state after 330 s from a warm start, in line with similar fixed bed reactor studies. On the other hand, the reactor needed 130 s to dissipate most of the reaction heat and return to nominal warm-start conditions. A 30 s H_2 feed disruption showed the appearance of a transient low-temperature hot spot. At t = 450 s (90 s after the H_2 feed was resumed), the maximum temperature and profile returned to the original steady-state condition. A sudden 20 K (523–543 K) rise in the inlet temperature triggered a lower temperature transient hot spot than the nominal case. On the other hand, a sudden 20 K (523–503 K) drop in the inlet stream led to higher transient temperatures. As a result, a high-temperature hot spot (≈923 K) was generated, which exposed the catalyst to its maximum operating temperature. According to simulation results, inlet temperature disruptions did not affect the minimum CH_4 outlet mole fraction. However, in the case of a 30 s H_2 feed loss, 90 s were necessary to stabilise the outlet concentration around 0.55. The appearance of wrong way behaviour was explained by moving concentration fronts prompted by a combination of transient reactant concentration and thermal inertia of the bed. Finally, in the absence of all heat sources, the reactor maintained warm start conditions for 3 h of idle operation. Further increment in the idle time could be attained at the expense of an increment in the reactor insulation layer.

The present contribution probed the significance of a 3D CFD model in designing tubular reactors subjected to dynamic disruptions. Unlike 1D/2D based simulation works, a 3D model allows identifying relevant design issues like the effect of different hot spot positions on the reactor cooling capability. Moreover, the transient nature of the model probed effective in identifying operational features not available to a steady state based simulation (e.g., a 20 K step drop in the inlet temperature exposed the reactor to its maximum operational temperature: 923 K). Future works may include validating the proposed design through an experimental study at the pilot plant scale and further enhancement of the design through process intensification (PI).

Author Contributions: V.S. contributed with CFD simulations and writing the original draft. X.G. and C.U. contributed with supervision and editing. All authors have read and agreed to the published version of the manuscript.

5. Appendix A. Thermodynamic, Physical Properties and Kinetic Parameters

Property	Value	Unit	Reference
Gas mixture			
Specific heat (C_{pg})	Mixing-law	J kg^{-1}K^{-1}	[31]
Thermal conductivity (λ_g)	Ideal gas mixing law	W m^{-1} K^{-1}	[31]
Density (ρ_g)	Incomp. ideal gas	Kg m^{-3}	[31]
Viscosity (μ_g)	Ideal gas mixing law	Kg m^{-1} s^{-1}	[31]
Binary molecular diffusion coefficient (D_{ij})	Chapman-Enskog	m^2 s^{-1}	[31]
Catalyst bed			
Bulk density (ρ_s)	1535	Kg m^{-3}	[32]
Specific heat (C_{ps})	880	J kg^{-1}K^{-1}	[17]
Thermal conductivity (λ_s)	0.67	W m^{-1} K^{-1}	[33]
Particle Diameter (d_p)	2.6	mm	[19]
Bed porosity	0.39	-	[17]
Permeability	1.045×10^{-8}	m^2	[31]
Inertial resistance	12,000	m^{-1}	[31]
Coolant (thermal oil)			
Density (ρ_f)	867	Kg m^{-3}	
Specific heat (C_{pf})	2181	J kg^{-1}K^{-1}	[34]
Viscosity (μ_g)	2.88×10^{-5}	Kg m^{-1} s^{-1}	
Thermal conductivity (λ_f)	0.1055	W m^{-1} K^{-1}	
Baffles & tube walls (Steel)			
Density (ρ_f)	8030	Kg m^{-3}	[35]

Specific heat (C_{pf})	502	J kg^{-1}K^{-1}	
Thermal conductivity (λ_{st})	16	W m^{-1} K^{-1}	
Kinetic parameters			
k_0	3.46×10^{-4}	kmol bar^{-1} kg$_{cat}^{-1}$ s^{-1}	
E_A	77,500	J mol^{-1}	
$K_{0.OH}$	0.5	bar$^{-0.5}$	
$\Delta H_{ads,OH}$	22,400	J mol^{-1}	
$K_{0.H_2}$	0.44	bar$^{-0.5}$	[5]
$\Delta H_{ads,H_2}$	-6200	J mol^{-1}	
$K_{0.mix}$	0.88	bar$^{-0.5}$	
$\Delta H_{ads,mix}$	$-10,000$	J mol^{-1}	
Activity factor	0.1	-	

6. References

1. Liu, J.; Sun, W.; Harrison, G.P. The economic and environmental impact of power to hydrogen/power to methane facilities on hybrid power-natural gas energy systems. *Int. J. Hydrog. Energy* **2020**, *45*, 20200–20209. https://doi.org/10.1016/j.ijhydene.2019.11.177.

2. Dannesboe, C.; Hansen, J.B.; Johannsen, I. Catalytic methanation of CO_2 in biogas: Experimental results from a reactor at full scale. *React. Chem. Eng.* **2019**, *5*, 183–189. https://doi.org/10.1039/c9re00351g.

3. Gaikwad, R.; Villadsen, S.N.B.; Rasmussen, J.P.; Grumsen, F.B.; Nielsen, L.P.; Gildert, G.; Møller, P.; Fosbøl, P.L. Container-Sized CO_2 to Methane: Design, Construction and Catalytic Tests Using Raw Biogas to Biomethane. *Catalysts* **2020**, *10*, 1428. https://doi.org/10.3390/catal10121428.

4. Hidalgo, D.; Martín-Marroquín, J.M. Power-to-methane, coupling CO_2 capture with fuel production: An overview. *Renew. Sustain. Energy Rev.* **2020**, *132*, 110057. https://doi.org/10.1016/j.rser.2020.110057.

5. Matthischke, S.; Roensch, S.; Güttel, R. Start-up Time and Load Range for the Methanation of Carbon Dioxide in a Fixed-Bed Recycle Reactor. *Ind. Eng. Chem. Res.* **2018**, *57*, 6391–6400. https://doi.org/10.1021/acs.iecr.8b00755.

6. Giglio, E.; Pirone, R.; Bensaid, S. Dynamic modelling of methanation reactors during start-up and regulation in intermittent power-to-gas applications. *Renew. Energy* **2021**, *170*, 1040–1051. https://doi.org/10.1016/j.renene.2021.01.153.

7. Moon, J.; Gbadago, D.Q.; Hwang, S. 3-D Multi-Tubular Reactor Model Development for the Oxidative Dehydrogenation of Butene to 1,3-Butadiene. *ChemEngineering* **2020**, *4*, 46. https://doi.org/10.3390/chemengineering4030046.

8. Jiang, B.; Hao, L.; Zhang, L.; Sun, Y.; Xiao, X. Numerical investigation of flow and heat transfer in a novel configuration multi-tubular fixed bed reactor for propylene to acrolein process. *Heat Mass Transf.* **2015**, *51*, 67–84. https://doi.org/10.1007/s00231-014-1384-3.

9. Fischer, K.L.; Freund, H. On the optimal design of load flexible fixed bed reactors: Integration of dynamics into the design problem. *Chem. Eng. J.* **2020**, *393*, 124722. https://doi.org/10.1016/j.cej.2020.124722.

10. Fache, A.; Marias, F. Dynamic operation of fixed-bed methanation reactors: Yield control by catalyst dilution profile and magnetic induction. *Renew. Energy* **2020**, *151*, 865–886. https://doi.org/10.1016/j.renene.2019.11.081.

11. Soto, V.; Ulloa, C.; Garcia, X. A CFD Design Approach for Industrial Size Tubular Reactors for SNG Production from Biogas (CO_2 Methanation). *Energies* **2021**, *14*, 6175. https://doi.org/10.3390/en14196175.

12. Try, R.; Bengaouer, A.; Baurens, P.; Jallut, C. Dynamic modeling and simulations of the behavior of a fixed-bed reactor-exchanger used for CO_2 methanation. *AIChE J.* **2017**, *64*, 468–480. https://doi.org/10.1002/aic.15874.

13. Li, X.; Li, J.; Yang, B.; Zhang, Y. Dynamic analysis on methanation reactor using a double-input–multi-output linearized model. *Chin. J. Chem. Eng.* **2015**, *23*, 389–397. https://doi.org/10.1016/j.cjche.2014.11.007.

14. Kreitz, B.; Wehinger, G.D.; Turek, T. Dynamic simulation of the CO_2 methanation in a micro-structured fixed-bed reactor. *Chem. Eng. Sci.* **2019**, *195*, 541–552. https://doi.org/10.1016/j.ces.2018.09.053.

15. Koschany, F.; Schlereth, D.; Hinrichsen, O. On the kinetics of the methanation of carbon dioxide on coprecipitated NiAl(O). *Appl. Catal. B Environ.* **2016**, *181*, 504–516. https://doi.org/10.1016/j.apcatb.2015.07.026.

16. Gruber, M.; Weinbrecht, P.; Biffar, L.; Harth, S.; Trimis, D.; Brabandt, J.; Posdziech, O.; Blumentritt, R. Power-to-Gas through thermal integration of high-temperature steam electrolysis and carbon dioxide methanation-Experimental results. *Fuel Process. Technol.* **2018**, *181*, 61–74. https://doi.org/10.1016/j.fuproc.2018.09.003.

17. Rönsch, S.; Ortwein, A.; Dietrich, S. Start-and-Stop Operation of Fixed-Bed Methanation Reactors—Results from Modeling and Simulation. *Chem. Eng. Technol.* **2017**, *40*, 2314–2321. https://doi.org/10.1002/ceat.201700229.

18. Jürgensen, L.; Ehimen, E.A.; Born, J.; Holm-Nielsen, J.B. Dynamic biogas upgrading based on the Sabatier process: Thermodynamic and dynamic process simulation. *Bioresour. Technol.* **2015**, *178*, 323–329. https://doi.org/10.1016/j.biortech.2014.10.069.

19. Molina, M.M.; Kern, C.; Jess, A. Catalytic Hydrogenation of Carbon Dioxide to Methane in Wall-Cooled Fixed-Bed Reactors‡. *Chem. Eng. Technol.* **2016**, *39*, 2404–2415. https://doi.org/10.1002/ceat.201500614.

20. Sun, D.; Simakov, D.S.A. Thermal management of a Sabatier reactor for CO_2 conversion into CH_4: Simulation-based analysis. *J. CO2 Util.* **2017**, *21*, 368–382. https://doi.org/10.1016/j.jcou.2017.07.015.

21. El Sibai, A.; Struckmann, L.K.R.; Sundmacher, K. Model-based Optimal Sabatier Reactor Design for Power-to-Gas Applications. *Energy Technol.* **2017**, *5*, 911–921. https://doi.org/10.1002/ente.201600600.

22. Alarcón, A.; Guilera, J.; Andreu, T. CO_2 conversion to synthetic natural gas: Reactor design over Ni-Ce/Al_2O_3 catalyst. *Chem. Eng. Res. Des.* **2018**, *140*, 155–165. https://doi.org/10.1016/j.cherd.2018.10.017.

23. Witte, J.; Settino, J.; Biollaz, S.M.A.; Schildhauer, T.J. Direct catalytic methanation of biogas—Part I: New insights into biomethane production using rate-based modelling and detailed process analysis. *Energy Convers. Manag.* **2018**, *171*, 750–768. https://doi.org/10.1016/j.enconman.2018.05.056.

24. Uebbing, J.; Rihko-Struckmann, L.K.; Sundmacher, K. Exergetic assessment of CO_2 methanation processes for the chemical storage of renewable energies. *Appl. Energy* **2019**, *233–234*, 271–282. https://doi.org/10.1016/j.apenergy.2018.10.014.

25. Hashemi, S.E.; Lien, K.M.; Hillestad, M.; Schnell, S.K.; Austbø, B. Thermodynamic Insight in Design of Methanation Reactor with Water Removal Considering Nexus between CO_2 Conversion and Irreversibilities. *Energies* **2021**, *14*, 7861. https://doi.org/10.3390/en14237861.

26. Sun, Q.; Gao, Q.; Zhang, P.; Peng, W.; Chen, S.; Zhao, G.; Wang, J. Numerical study of heat transfer and sulfuric acid decomposition in the process of hydrogen production. *Int. J. Energy Res.* **2019**, *43*, 5969–5982. https://doi.org/10.1002/er.4714.

27. V. Gnielinski, "G7 Heat Transfer in Cross-flow Around Single Rows of Tubes and Through Tube Bundles," in VDI Heat Atlas, Berlin, Heidelberg: Springer Berlin Heidelberg, 2010, pp. 725–730. doi: 10.1007/978-3-540-77877-6_40. Commission Regulation (EU) 2017/1485 of 2 August 2017 Establishing a Guideline on Electricity Transmission System Operation (Text with EEA Relevance.). 2017. Volume 220. Available online: http://data.europa.eu/eli/reg/2017/1485/oj/eng (accessed on 2 February 2022).

28. Bremer, J.; Rätze, K.H.G.; Sundmacher, K. CO_2 methanation: Optimal start-up control of a fixed-bed reactor for power-to-gas applications. *AIChE J.* **2016**, *63*, 23–31. https://doi.org/10.1002/aic.15496.

29. Fache, A.; Marias, F.; Guerré, V.; Palmade, S. Optimization of fixed-bed methanation reactors: Safe and efficient operation under transient and steady-state conditions. *Chem. Eng. Sci.* **2018**, *192*, 1124–1137. https://doi.org/10.1016/j.ces.2018.08.044.

30. ANSYS, Inc. *ANSYS Fluent Theory Guide*, 15th ed.; ANSYS, Inc.: Canonsburg, PA, USA, 2013.

31. Scharl, V.; Fischer, F.; Herrmann, S.; Fendt, S.; Spliethoff, H. Applying Reaction Kinetics to Pseudohomogeneous Methanation Modeling in Fixed-Bed Reactors. *Chem. Eng. Technol.* **2020**, *43*, 1224–1233. https://doi.org/10.1002/ceat.201900535.

32. Ducamp, J.; Bengaouer, A.; Baurens, P. Modelling and experimental validation of a CO_2 methanation annular cooled fixed-bed reactor exchanger. *Can. J. Chem. Eng.* **2016**, *95*, 241–252. https://doi.org/10.1002/cjce.22706.

33. Therminol VP-1 Heat Transfer Fluid. Available online: https://www.therminol.com/product/71093459 (accessed on 25 April 2021).

34. Kreith, F.; Manglik, R.M.; Bohn, M.S. *Principles of Heat Transfer*; Cengage Learning: Boston, MA, USA, 2011.

V. Conclusions

PtM has a great potential to become the necessary link between intermittent renewable energy development and electricity grid balancing. The methanation reactor appears as the core element to be considered for proper deployment of PtM technology. Several design concepts exist; however, the tubular fixed bed reactor stands out as the only feasible alternative to develop industrial sized methanation plants. The first part of this work developed the reactor modelling technique, based on PMM-CFD methodology. A design case study was conducted aimed at proposing a methanation reactor for small to medium biogas upgrade applications. The proposed design/modelling approach probed to be accurate and efficient in terms of the computational resources required to simulate an industrial sized reactor. This approach does not only allow to capture relevant transport phenomena with accuracy (20% and 10% maximum error for the predicted temperature profile, heat transfer coefficients respectively) but also to properly identify relevant design features like baffle positioning, tube arrangement and optimal coolant selection. As a case study, our proposed methodology allowed to distinguish between the two most common coolants. Unlike what is reported in the literature, thermal oil allows for less energy demand in pumping power than molten salts, while preserving the thermal and product gas integrity on equal terms. Authors usually recommend the use of molten salts to avoid risks of coolant degradation, however this study demonstrated that given the correct flow and temperature no such risk exist. The second part of this work conducted a series of transient analysis aimed at identifying the capabilities of the design that was proposed previously under a Power to Gas operational scenario. The proposed design was able to withstand feed composition and inlet temperature disruptions pertinent to a Power to Gas context. Among the two disruption types studied (composition and temperature), the most critical disruption was a 20 K temperature drop, exposing the catalyst to its maximum operational temperature. On the other hand, temperature disruptions did not affect substantially the minimum content of CH_4 in the outlet gas. Only a 30 s disruption in the H_2 feed impacted the minimum CH_4 content during a 90 s period. After which, the reactor was able to return to nominal conditions. Results from both research articles allowed to confirm and prove the capabilities of the proposed methodology to design and modelling CO_2 methanation reactors for Power to Gas applications.

Up to now, the reactor design process was only aimed at identifying the required catalyst mass to achieve a certain conversion. From the standpoint of the mechanical engineer the traditional design approach hardly resembles the formal engineering design process. Although it is taught as such in under and postgraduate chemical engineering courses worldwide. This work aims at closing that knowledge gap, by given the chemical/mechanical engineer student or acting engineer a methodological tool to properly design and model not only methanation reactors, but also any other fixed bed-based processes like Fischer Tropsch, Methanol and Ammonia synthesis, combining accuracy, engineering detail and computational cost effectiveness.

VI.   Recommendations for future works

Although the focus of this work was the CO_2 methanation process as Power to Methane, the methodology proposed may be expanded into other syntheses of interest which may also be compatible with tubular fixed bed technology (e.g., Power to Liquids Fischer Tropsch, Power to Methanol, Power to Ammonia). The author recognizes however, that to be fully applicable to develop a fully detailed engineering package, this methodology should be enhanced by taking into consideration the economic "dimension" of the Power to Methane process. Therefore, a techno-economic assessment should be conducted considering the case of a medium sized biogas source as case study. The viability of the process may be well evaluated considering all relevant equipment and process streams (energy and mass). For such purposes, a process design study is also recommended by making use of existing tools like Aspen Hysys or Aspen Plus. Regarding the relevant coolants for fixed bed tubular reactors, recent works have begun to test nucleate boiling cooling systems. It is known that those systems are able to remove heat in a very efficient way by means of convective heat transfer coefficients several times larger than the traditional systems (thermal oils, molten salts or water steam). Therefore, the present CFD modelling methodology may be supplemented by a multiphase model, which may incorporate the nucleate boiling phenomenon in the shell side, as an enhanced coolant system.

VII.   Conclusiones y recomendaciones para trabajos futuros

El proceso PtM tienen un gran potencial para convertirse en el vínculo necesario entre el desarrollo de energías renovables intermitentes y el equilibrio de la red eléctrica. El reactor de metanación aparece como el elemento central a considerar para un correcto despliegue de la tecnología PtM. Existen varios conceptos de diseño; sin embargo, el reactor tubular de lecho fijo se destaca como la única alternativa factible para desarrollar plantas de metanación de tamaño industrial. La primera parte de este trabajo desarrolló la técnica de modelado de reactores, basada en la metodología PMM-CFD. Se llevó a cabo un estudio de caso de diseño con el objetivo de proponer un reactor de metanación para aplicaciones pequeñas y medianas de acondicionamiento de biogás. El enfoque de diseño/modelado propuesto demostró ser preciso y eficiente en términos de los recursos computacionales necesarios para simular un reactor de tamaño industrial. Este enfoque no solo permite capturar fenómenos de transporte relevantes con precisión (20% y 10% de error máximo para el perfil de temperatura previsto, coeficientes de transferencia de calor, respectivamente), sino también identificar correctamente las características de diseño relevantes, como el posicionamiento del deflector, la disposición de los tubos y la selección óptima del refrigerante. Como caso de estudio, nuestra metodología propuesta permitió evaluar el performance entre los dos refrigerantes más comunes (aceite térmico y sal fundida). A diferencia de lo reportado en la literatura, el aceite térmico permite una menor demanda de energía en el poder de bombeo que las sales fundidas, al mismo tiempo que preserva la integridad térmica y del gas producto en igualdad de condiciones. Los autores generalmente recomiendan el uso de sales fundidas para evitar riesgos de degradación del refrigerante, sin embargo, este estudio demostró que, dado el flujo y la temperatura correctos, no existe tal riesgo. La segunda parte de este trabajo realizó una serie de análisis transientes con el objetivo de identificar las capacidades del diseño que se propuso previamente bajo un escenario operativo Power to Gas. El diseño propuesto fue capaz de resistir la alteraciones en la alimentación y temperatura de entrada correspondientes a un contexto de Power to Gas. Entre los dos tipos de disrupción estudiados (composición y temperatura), la disrupción más crítica fue una caída de temperatura de 20 K, exponiendo el catalizador a su temperatura operativa máxima. Por otro lado, las alteraciones de temperatura no afectaron sustancialmente el contenido mínimo de CH_4 en el gas de salida. Solo una interrupción de 30 s en la alimentación de H_2 impactó el contenido mínimo de CH_4 durante un período de 90 s. Después de lo cual, el reactor pudo volver a las

condiciones nominales. Los resultados de ambos artículos de investigación permitieron confirmar y probar las capacidades de la metodología propuesta para diseñar y modelar reactores de metanación de CO_2 para aplicaciones Power to Gas.

Aunque el enfoque de este trabajo fue el proceso de metanación de CO_2 como Power to Methane, la metodología propuesta puede expandirse a otras síntesis de interés que también pueden ser compatibles con la tecnología de lecho fijo tubular (por ejemplo, Power to Liquids Fischer Tropsch, Power to Methanol, Power to Ammonia). El autor reconoce, sin embargo, que para desarrollar un paquete de ingeniería completamente detallado, esta metodología debe mejorarse teniendo en cuenta la "dimensión" económica del proceso Power to Methane. Por lo tanto, se debe realizar una evaluación técnico-económica considerando el caso de una fuente de biogás de tamaño mediano como caso de estudio. La viabilidad del proceso puede evaluarse bien teniendo en cuenta todos los equipos y flujos de proceso relevantes (energía y masa). Para tales efectos, también se recomienda un estudio de diseño de procesos haciendo uso de herramientas existentes como Aspen Hysys o Aspen Plus. En cuanto a los refrigerantes relevantes para reactores tubulares de lecho fijo, trabajos recientes han comenzado a probar sistemas de enfriamiento por ebullición nucleada. Se sabe que estos sistemas son capaces de remover calor de manera muy eficiente mediante coeficientes de transferencia de calor por convección varias veces mayores que los sistemas tradicionales (aceites térmicos, sales fundidas o vapor de agua). Por lo tanto, la presente metodología de modelado CFD puede complementarse con un modelo multifásico, que puede incorporar el fenómeno de ebullición nucleada en el lado de la carcasa, como un sistema de refrigeración mejorado.

Annex A: Koschany Kinetics UDF in C language

```c
/*
Sabatier.m, Version 1.0
First created by Victor Soto Pascual on 08/07/2020
Last modified by Victor Soto Pascual on 23/04/2021
References:
Matthischke (2018)
Koschany   (2016)
/*


/* Description: This UDF incorporates the Sabatier reaction (1): CO2 + 4H2 <-> CH4 + 2H2O as a volumetric reaction in
a porous media model. The RWGS reaction (2): CO2 + H2 <-> CO + H2O is neglected according to the references and operational conditions
considered.*/


#include "udf.h"
#include "math.h"

DEFINE_VR_RATE(v_rate, c, t, r, mole_weight, species_mf, rate, rr_t)

/*DEFINE_VR_RATE specifices a custom volumetric reaction rate for a single reaction or multiple reactions*/
/*From ANSYS Fluent UDF manual: rate and rr_t are conversion rates in kmol/m3*s. These rates, when multiplied by the respective
stoichiometric coefficients, yield the production/consumption rates of the individual chemical components*/

{
        real T, P;                                              /*Definition of Cell Value functions: Temperature, Pressure*/

        real m;
                                                                /*Total moles (kgmol)*/

        real m_CO2, m_N2, m_H2, m_H2O, m_CH4;
                                                                /*Species [i] moles (kgmol)*/

        real mole_fraction_CO2,
                mole_fraction_N2, mole_fraction_H2, mole_fraction_H2O, mole_fraction_CH4;   /*Species mole fractions*/

        real p_CO2, p_N2, p_H2, p_H2O, p_CH4;                   /*Species partial pressures*/

        #define UGC 8.314
                                                                /*Universal Gas Constant (J/mol*K)*/

        #define rho_cat 1475                                    /*Catalyst density in (kg/m3) */

        #define af 0.1                                          /*Activity factor, acc. to matthischke_2018 */

/*Calculation of Cell Partial pressures */

        T = C_T(c, t);                                          /*Cell static temperature calculation in (K)*/

        P = 10 + (C_P(c, t) / 1e5);                             /*Cell static presure calculation. Change from Pa to bar */

/*Calculation of species mole fractions*/

        m_CO2 = species_mf[4] / mole_weight[4];

        m_N2 = species_mf[3] / mole_weight[3];

        m_H2 = species_mf[2] / mole_weight[2];

        m_H2O = species_mf[0] / mole_weight[0];

        m_CH4 = species_mf[1] / mole_weight[1];

        m = m_CO2 + m_N2 + m_H2 + m_H2O + m_CH4;

        mole_fraction_CO2 = m_CO2 / m;

        mole_fraction_N2 = m_N2 / m;

        mole_fraction_H2 = m_H2 / m;

        mole_fraction_H2O = m_H2O / m;

        mole_fraction_CH4 = m_CH4 / m;

/*Calculation of species partial pressures*/

        p_CO2 = mole_fraction_CO2 * P;

        p_N2 = mole_fraction_N2 * P;

        p_H2 = mole_fraction_H2 * P;

        p_H2O = mole_fraction_H2O * P;

        p_CH4 = mole_fraction_CH4 * P;


/*Calculation of kinetic constant "k" in mol/(bar*gr*s)*/

        real k = 3.46e-4 * exp((77500 / UGC) * (1.8018e-3 - 1 / T));       /* acc. to Matthischke (2018) 3.46e-4 , mol/(bar*gr*s) */


/*Calculation of adsorption constants. Heats of adsorption (J/kmol) from Matthischke (2018)*/
```

```
            real KOH = 0.5 * exp((22400 / UGC) * (1.8018e-3 - 1 / T));

            real KH2 = 0.44 * exp((-6200 / UGC) * (1.8018e-3 - 1 / T));

            real Kmix = 0.88 * exp((-10000 / UGC) * (1.8018e-3 - 1 / T));
/*Calculation of equilibrium constants*/

            real Keq = 137 * pow(T, -3.998) * exp((158700 / (UGC * T)));


/*Calculation of approach to equilibrium term: beta_1*/

            real beta_1;
             if (p_CO2 == 0)

                    beta_1 = 0;

        else if (p_H2 == 0)

                    beta_1 = 0;

        else

                    beta_1 = (p_CH4 * pow(p_H2O, 2) / (p_CO2 * pow(p_H2, 4) * Keq));


/*Calculation of denominator term: DEN*/

            real DEN;

        if (p_H2 == 0)

                    DEN = 1;

        else

                    DEN = pow((1 + KOH * (p_H2O / pow(p_H2, 0.5) + KH2 * pow(p_H2, 0.5) + Kmix * pow(p_CO2, 0.5))), 2);


/*Calculation of the Rate of reaction (1) in (kmol/m3*s)*/

        *rate = df * af * rho_cat * k * pow(p_H2, 0.5) * pow(p_CO2, 0.5) * (1 - beta_1) / DEN;


/*Stops the reaction rate if becomes excessively high*/
                    if (*rate > 10)
                    {
                            *rate = 10;
                    }
                    else if (*rate < -10)
                    {
                            *rate = -10;
                    }

                    *rr_t = *rate;

                    }
```